“Matériaux Avancés à Base des Nanotubes de TiO_2 pour la Fabrication de Microbatteries 3D Li-ion”

THESE

Présentée et soutenue pour obtenir le grade de Docteur

Par:

Nana Amponsah Kyerematen

Discipline: Matière Condensée et Nanoscience
Ecole Doctorale: Physique et Science de la Matière

Jury:

Pr. Philippe Poizot	*Université de Nantes, France.*	Rapporteur
Pr. Patrik Schmuki	*Université d’Erlangen-Nürnberg, Allemagne.*	Rapporteur
Pr. Thierry Djenizian	*Aix Marseille Université, France.*	Directeur de Thèse
Dr. Philippe Delaporte	*Aix Marseille Université, France.*	Examinateur
Pr. Philippe Knauth	*Aix Marseille Université, France.*	Examinateur
Pr. José L. Tirado	*Université de Cordoue, Espagne.*	Examinateur

Aix Marseille Université

Le 23 NOVEMBRE, 2012.

"Advanced Materials Based On Titania Nanotubes for the Fabrication of High-Performance 3D Li-ion Microbatteries"

THESIS

Submitted and Defended in Fulfilment for PhD Degree

By:

Nana Amponsah Kyerematen

Discipline: Condensed Matter and Nanoscience
Doctoral School: Physics and Materials Science

Jury:

Pr. Philippe Poizot	*University of Nantes, France.*	Rapporteur
Pr. Patrik Schmuki	*University of Erlangen-Nürnberg, Germany.*	Rapporteur
Pr. Thierry Djenizian	*Aix Marseille University, France.*	PhD Supervisor
Dr. Philippe Delaporte	*Aix Marseille University, France.*	Examiner
Pr. Philippe Knauth	*Aix Marseille University, France.*	Examiner
Pr. José L. Tirado	*University of Cordoba, Spain.*	Examiner

Aix Marseille University

23rd NOVEMBER, 2012.

RESUME

Le développement des dispositifs microélectroniques a dopé la recherche dans le domaine des microbatteries tout solide rechargeables. Mais actuellement, les performances de ces microbatteries élaborées par des technologies couche mince (2D) sont limitées et le passage à une géométrie 3D adoptant le concept "Li-ion" ou "rocking chair" est incontournable. Cette dernière condition implique de combiner des matériaux de cathode comme $LiCoO_2$, $LiMn_2O_4$ or $LiFePO_4$ avec des anodes pouvant réagir de manière réversible avec les ions lithium. Parmi tous les matériaux pouvant servir potentiellement d'anode, les nanotubes de TiO_2 révèlent des propriétés intéressantes pour concevoir des microbatteries Li-ion 3D. Facilement réalisable, la nano-architecture auto-organisée a montré des résultats très prometteurs en termes de capacités à des cinétiques relativement modérées. L'utilisation des nanotubes de TiO_2 en tant qu'anode conduit à des cellules présentant de faible auto-décharge et élimine le risque de surcharge grâce au haut potentiel de fonctionnement (1.72 V vs. Li^+/Li). Dans ce travail de thèse, nous avons étudié la substitution des ions Ti^{4+} par Sn^{4+} et Fe^{2+} dans les nanotubes de TiO_2. Bien que la présence d'ions Fe^{2+} n'ait pas amélioré les performances électrochimiques des nanotubes, nous avons pu mettre en évidence l'effet bénéfique des ions Sn^{4+}. Nous avons aussi pu montré que la fabrication de matériaux composites à base de nanotubes de TiO_2 et d'oxyde de métaux de transition électrodéposés se présentant sous forme de particules (NiO et Co_3O_4) augmentait les capacités d'un facteur 4. Un premier pas vers la fabrication d'une microbatterie entièrement 3D a été aussi réalisée en étudiant l'électrodéposition conforme d'électrolytes polymères sur les parois des nanotubes de TiO_2. La morphologie de l'interface ainsi que les propriétés électrochimiques du matériau résultant ont été comparées à celles de nanotubes recouverts d'un électrolyte solide (LiPON) déposé par PVD (Physical Vapor Deposition). Les méthodes de caractérisation employées ont inclus la microscopie élecronique à balayage, en transmission, la diffraction des rayons X, la spectroscopie de Mössbauer et la spectroscopie de photoelectrons X.

ABSTRACT

The advent of modern microelectronic devices has necessitated the search for high-performance all-solid-state (rechargeable) lithium microbatteries. Presently, there is a need to move from 2D to 3D configurations, and also a necessity to adopt the "Li-ion" concept in designing these (thin-film) microbatteries. New electrode and electrolyte materials and cost-effective fabrication processes are also indispensable. Among all the potential anode materials, TiO_2 nanotubes possess a spectacular characteristic for designing 3D Li-ion microbatteries. Besides the nano-architecture, TiO_2 is non-toxic and inexpensive, and the nanotubes have intriguing lithium storage behaviour. The use of TiO_2 as anode provides cells with low self-discharge and eliminates the risk of overcharging due to its higher operating voltage (ca. 1.72 V vs. Li^+/Li). Moreover, the overall performance of TiO_2 nanotubes can be improved. In this thesis, Sn^{4+} or Fe^{2+} cationic substitution for Ti^{4+} in TiO_2 nanotubes was studied; although Fe^{2+} substitution did not improve the electrochemical behaviour of TiO_2 nanotubes, Sn^{4+} substitution led to higher capacity values in comparison to simple TiO_2 nanotubes even though Sn was not active within the studied potential window. Additionally, composites of TiO_2 nanotubes with sub-micron NiO or Co_3O_4 particles were synthesized; the addition of these transition metal oxide particles onto the TiO_2 nanotubes increased the capacity values by a factor of ~4. As a first step towards the fabrication of a 3D microbattery with TiO_2 nanotubes, electrodeposition of polymer electrolytes into TiO_2 nanotubes was studied; the inter-phase morphology and the electrochemical behaviour of the resulting material were studied and compared to similar TiO_2 nanotubes with LiPON solid electrolytes deposited by sputtering techniques. The characterization included scanning electron microscopy, transmission electron microscopy, X-ray diffraction, Mössbauer Spectroscopy and X-ray photoelectron spectroscopy.

DEDICATION

I dedicate this work to my wife, Isabella Kyerematen and my daughter, Michelle Fosuah Kyerematen, as well as all my future children.

ACKNOWLEDGEMENTS

I express my profound gratitude to **Professor Thierry Djenizian** for his remarkable support as the PhD supervisor. Apart from his patience and kindness, the encouragement and the experience he shared contributed significantly for the successful completion of the set objectives. I also offer my heartfelt appreciation to **Professor Patrik Schmuki** (Rapporteur), **Professor Philippe Poizot** (Rapporteur), **Professor José Luis Tirado** (Examiner)**, Dr. Philippe Delaporte** (Examiner) and **Professor Philippe Knauth** (Examiner) for their priceless roles as judges of this work. I am equally grateful to all the members of *MADIREL* laboratory (where the PhD work was done) especially **Dr. Ilie Hanzu** (for PhD work startup), **Dr. Florence Vacandio** (for physical vapour deposition assistance), **Dr. Chrystelle Lebouin** (for experimental assistance), **Ms. Carine Chassignaux** (for physical vapour deposition and XRD assistance), **Dr. Marielle Eyraud** (for experimental assistance), **Dr. Virginie Hornebecq** (for experimental assistance) and all the other members of *ElMa* research group such as **Dr. Katrin Pelzer**, **Dr. Florence Boulc'h** and **Ms. Amélie Demoulin** for their friendship and support**.** Lastly, no amount of words can describe my gratitude to **Dr. Frederic Dumur** of *ICR* laboratory (for the collaborative work on polymer deposition and characterization), **Professor Hervé Martinez** of Pau university (for the X-ray photoelectron spectroscopy characterization), **Dr. Moulay-Tahar Sougrati** of Montpellier university (for the Mössbauer spectroscopy characterization) and **Dr. Brigitte Pecquenard** of Bordeaux university (for the LiPON deposition and the preliminary electrochemical measurements).

TABLE OF CONTENTS

CHAPTER ONE

1. INTRODUCTION

1.1 Background

The advent of modern microelectronic devices has necessitated the search for high-performance all-solid-state (rechargeable) microbatteries. These microbatteries (based on thin-films) are integrated into microelectronic circuit boards to meet the very low energy requirement of devices such as, backup power for PC memory, microelectromechanical systems (MEMS), medical implants, hearing aids, "smart" cards, RFID tags, remote sensors and so forth[1-4]. These autonomous devices operate independently and thus on-chip electricity is indispensable.

For over four decades, microbatteries have evolved enormously with varying compositions, form factors and performance characteristics; but it cannot be overemphasized that only lithium-based systems fulfill the voltage and energy density requirements of microbatteries[5, 6]. It all began in 1969, when several silver and copper-based microbatteries were studied because of the high ionic conductivity of silver and copper solid electrolytes, but they turned out to be impractical, of low energy densities and high cost[7-10]. Around the same time, Liang *et al.*[11, 12] reported the first thin-film lithium cell comprising of the Li/LiI/AgI electrochemical chain which exhibited an open circuit voltage of 2.1 V. As a result of the work of Whittingham and Gamble[13] on the reversible insertion of lithium into transition metal dichalcogenides in 1975, Kanehori *et al.*[14] developed secondary thin-film lithium cells with amorphous $Li_{3.6}Si_{0.6}P_{0.4}O_4$ layers as the solid electrolyte, and TiS_2 films deposited by condensed vapor deposition (CVD) as

the cathode. However, the extreme stiffness of the electrolyte material deterred it from fully accommodating the volume expansion of the cathode material upon lithium intercalation.

In 1988, Jourdaine *et al*.[6] developed a microbattery comprising of $Li|Li_2O–B_2O_3|V_2O_5–P_2O_5$ or $Li|Li_2O–B_2O_3–P_2O_5|V_2O_5–TeO_2$ but the performance was poor due to low lithium diffusivity arising from the glassy nature of both the positive electrode ($V_2O_5–P_2O_5$ or $V_2O_5–TeO_2$) and the electrolyte ($Li_2O–B_2O_3$ or $Li_2O–B_2O_3–P_2O_5$). In 1989, Meunier *et al*.[15] reported a promising microbattery that consisted of TiO_xS_y thin-films (deposited by RF-sputtering) as cathodes, a sputter-deposited $B_2O_3–0.8Li_2O–0.8Li_2SO_4$ glass as electrolyte and a thermally evaporated lithium thin film as anode. It was in 1992 that Jones and Akridge[16] reported the milestone work of a more functional thin-film microbattery. The microbattery was constructed using cathodic sputtering for deposition of chromium contacts, TiS_2 cathode, and $6LiI-4Li_3PO_4–P_2S_5$ solid electrolyte, whilst high-vacuum vapor deposition was used for the lithium thin-film anode.

Although various other designs were reported[17-21] with different cathode and electrolyte materials, it was the work of Bates *et al*.[22, 23] in 1993 that made profound impact. Their cell designs consisted of $Li-TiS_2$, $Li-V_2O_5$, and $Li-Li_xMn_2O_4$ couples with $Li_{2.9}PO_{3.3}N_{0.46}$ (LiPON) as the solid electrolyte. The thin-film electrolyte was obtained by RF-magnetron sputtering of Li_3PO_4 in an N_2 atmosphere. This solid electrolyte, having a conductivity of 2 μS cm^{-1} at room temperature, showed a good stability and thus it has become the widely adopted solid electrolyte for lithium-based microbatteries to date.

Conventionally, microbatteries are fabricated by a sequential layer-by-layer deposition of the cell components using physical-vapour-depositon (PVD) techniques, and they have quite small dimensions (~1000 mm^3)[24]. The low output energy of a microbattery is simply a function of its size. They are generally called solid-state batteries as they are

composed of thin-film ceramic materials as anode, cathode and electrolyte[5]. The performance of thin-film batteries are commonly expressed in terms of energy or power per area (or volume), instead of per mass[25].

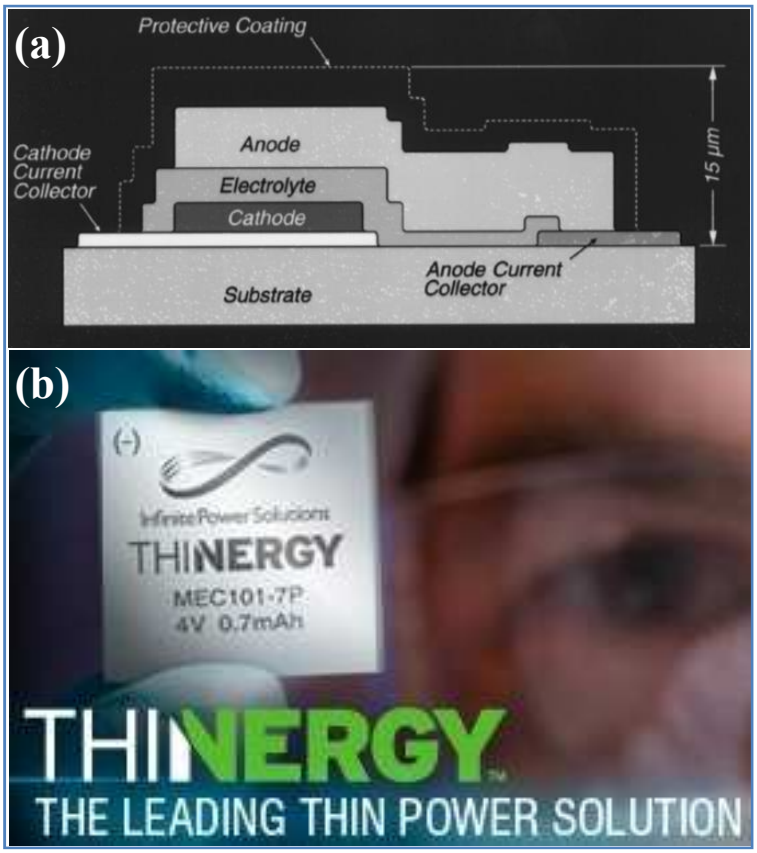

Figure 1 (a) Schematic of the internal configuration of a conventional (Planar) thin-film microbattery[25]; (b) An exemplary thin-film microbattery (courtesy of *THINERGY™ MEC*)

Figure 1a shows a schematic portraying the two-dimensional (2D) nature of conventional (thin-film) microbatteries, an exemplary commercial microbatteriy is also shown in Figure 1b. They comprise of a parallel configuration or a sandwich of a planar cathode and anode separated by an electrolyte. As a result of this 2D geometry, evidently, the microbatteries are not small enough. In addition, higher output energy/power densities are recently required of microbatteries, and eventhough this demand could be met by increasing the content of the active materials, it would simultaneously increase the dimensions or the areal footprint. However, as a result of the miniaturization of modern electronic devices, the size of microbatteries must be kept as small as possible (≤0.1

cm^3)[24, 26, 27]. This implies the reduction of the footprint of thin-film microbatteries through 3D architectures[24, 28-31].

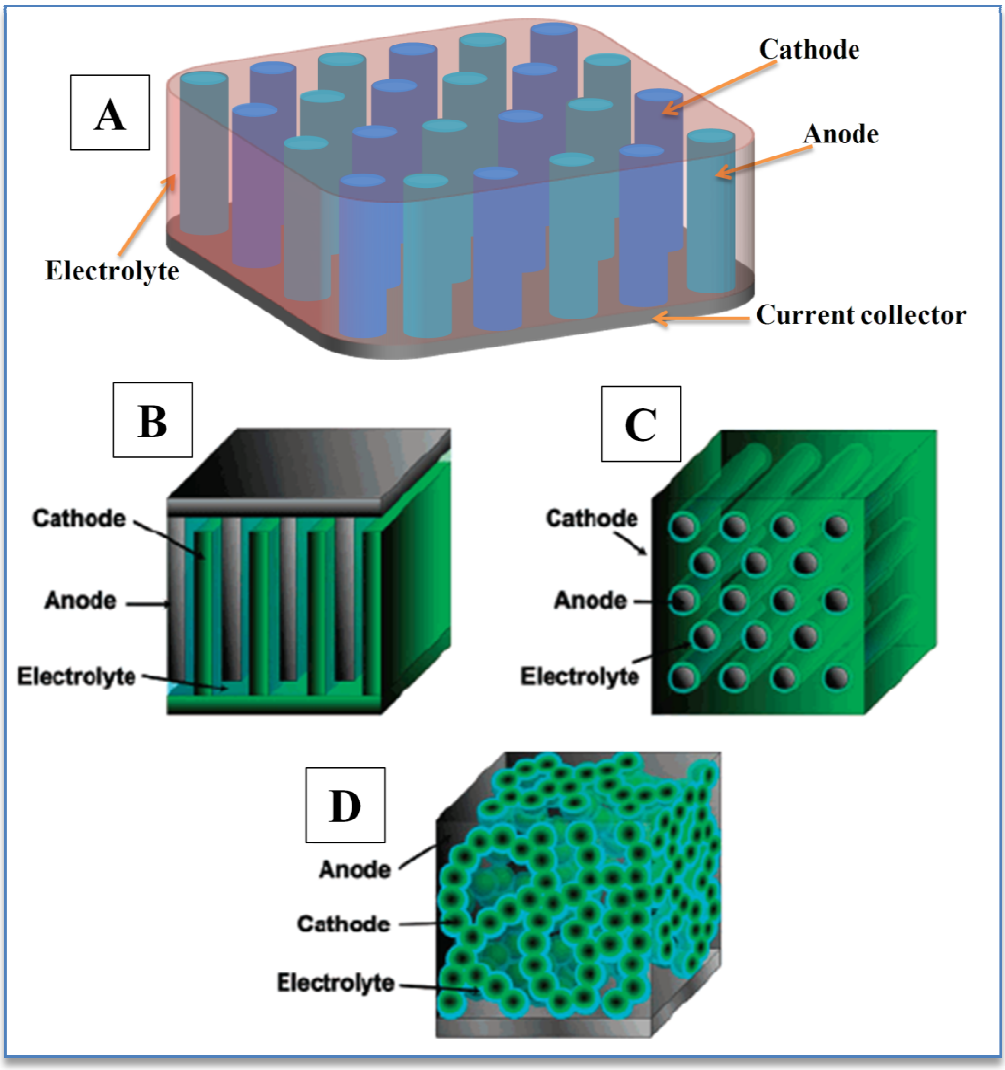

Figure 2 Schematics of prospective 3D microbattery designs: (a) array of interdigitated cylindrical cathodes and anodes; (b) interdigitated plane array of cathodes and anodes; (c) rod array of cylindrical anodes coated with a thin layer of electrolyte, and the remaining free volume filled with the cathode material; (d) aperiodic "sponge" architecture in which the solid network of the sponge serves as the charge-insertion cathode, which is coated with an ultrathin layer of electrolyte, and the remaining free volume filled with an interpenetrating (continuous) anode[31].

Achieving a three-dimensional (3D) thin-film microbattery stands as a crucial paradigm shift. The 3D design simply means having anodes and cathodes with surfaces exposed in three dimensions[27,28]. Figure 2a-d shows schematics of prospective 3D microbattery designs. Such 3D configurations would make use of the out-of-plane dimension instead of

just the in-plane surface of conventional thin-film microbatteries. Nanostructuration of electrode materials is one of the most promising approaches to realize this 3D paradigm of microbatteries, ensuring increased cell capacity and reduced areal footprint (i.e., square footage)[31]. Actually, nanostructuration of electrode materials is known to lead to higher energy densities because of increased effective surface area and short ion diffusion length between anode and cathode. Also, it is very suitable for sustaining mechanical and structural strain during electrochemical reactions[29, 31, 32].

As yet, the 3D approach has not reached commercialization and there are not even many prototypes reported in literature. It was Nathan *et al.*[33] that first reported a 'functioning-full-3D' li-ion microbattery based on a sandwich-like structure of conformally deposited thin-film electrodes, electrolyte and current collectors using wet chemistry. Golodnitsky *et al.*[1, 34] proposed a 3D design of perforated silica-based substrates filled with current collector, cathode, electrolyte and anode materials. The materials were deposited by combined electrolytic methods and a series of spinning and vacuum impregnation steps. The silicon substrate perforated with high-aspect-ratio micro-holes or micro-channels increased the active surface area by more than an order of magnitude and consequently the capacity. Baggetto *et al.*[27, 28] reported the most promising 3D design based on a step-conformal successive deposition of Li-diffusion barrier layers, high energy density Si-anodes, solid-state electrolytes, cathodes and current collectors. In their design (Figure 3), a thin-film current collector covers a single crystal Si substrate. Anisotropic etching of the Si substrate led to a large surface area. A barrier layer was then deposited to protect the substrate from Li penetration, followed by a Si anode thin film, LiPON solid electrolyte, $LiCoO_2$ cathode thin film and its current collector.

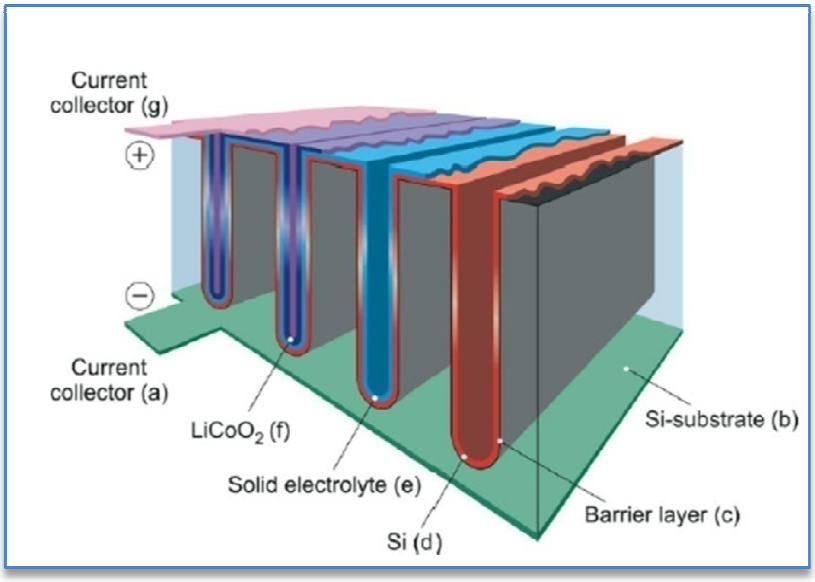

Figure 3 Schematic of a 3D thin-film (all-solid-state) Li-ion battery fabricated by electrochemical/reactive ion etching (RIE) of a silicon substrate and conformally depositing the other components using low pressure chemical vapor deposition[27].

Jeyaseelan and Rohan[35] used lithographic techniques to pattern planar substrates to achieve 3D substrates for sequential deposition of electrode materials. Min *et al.*[36] proposed the carbon-microelectromechanical system (C-MEMS) microfabrication process as a possibility for fabricating 3D battery architectures. Lethien *et al.*[37] proposed a 3D Li-ion microbattery based on a micromachined silicon periodic nanopillar array and a micropatterned LiPON/$LiFePO_4$ conformal layers. Recently, Yoshima *et al.*[38] reported a 3D Li-ion microbattery consisting of a 3D $Li_4Ti_5O_{12}$ anode and a 3D $LiCoO_2$ cathode (selectively formed on interdigitated current collectors by slip-casting) separated by a PMMA gel electrolyte layer.

In addition to targeting higher energy densities, significant attempts are being made to fully adopt the "Li-ion" or the "rocking-chair" concept in the design of lithium-based microbatteries[1, 28]. This implies the combination of cathode materials such as $LiCoO_2$, $LiMn_2O_4$ or $LiFePO_4$[39-41] with the wide range of possible anode materials that can react reversibly with lithium either by insertion[42-44], alloying[28, 32, 45, 46] or conversion[47-50]. Cathode materials such as V_2O_5 and TiO_xS_y are of considerable interest particularly with a

lithiated anode material to maintain the 'Li-ion' concept[13, 51-53]. As a matter of fact, the negative electrode material for thin-film microbatteries is of a great concern. All thin-film microbatteries utilize metallic lithium as anode and this is a major setback in fabrication and applications due to the low melting point and the strong reactivity of lithium. Metallic lithium is highly volatile and melts at about 181 ºC, a temperature usually lower than that applied during the re-flow soldering process widely used in the micro-electronic industries. In addition, an expensive packaging technology is always required due to the lithium anode[53]. Indeed, the importance of replacing the conventional microbattery design with the "Li-ion" or the "rocking-chair" technology cannot be overemphasized.

1.2 Objectives

Among all the potential anode materials, TiO_2 nanotubes (TiO_2nts) possess a spectacular characteristic for designing 3D Li-ion microbatteries. Actually, the ideal 3D microbattery designs schematically shown in Figure 2a-d have not been realized yet. So far, only interdigitated designs have been reported, by patterning one electrode material with lithography and/or ion etching techques and consecutively depositing the electrolyte and the second electrode material[1, 27, 28, 34, 35, 54]. It is in view of this that we have developed the interest to exploit the 3D nano-architecture of TiO_2 nanotubes, given that the nanotubes are self-supported onto Ti-foil or Si-wafer substrates and the tubes' top openings are large enough (or can be tailored) for the successive depositions of conformal thin-film electrolyte and cathode material and a non-conformal current collector as shown in Figure 4. It is also believed that a 3D design based on a conformal current collector is possible as schematically shown in Figure 5.

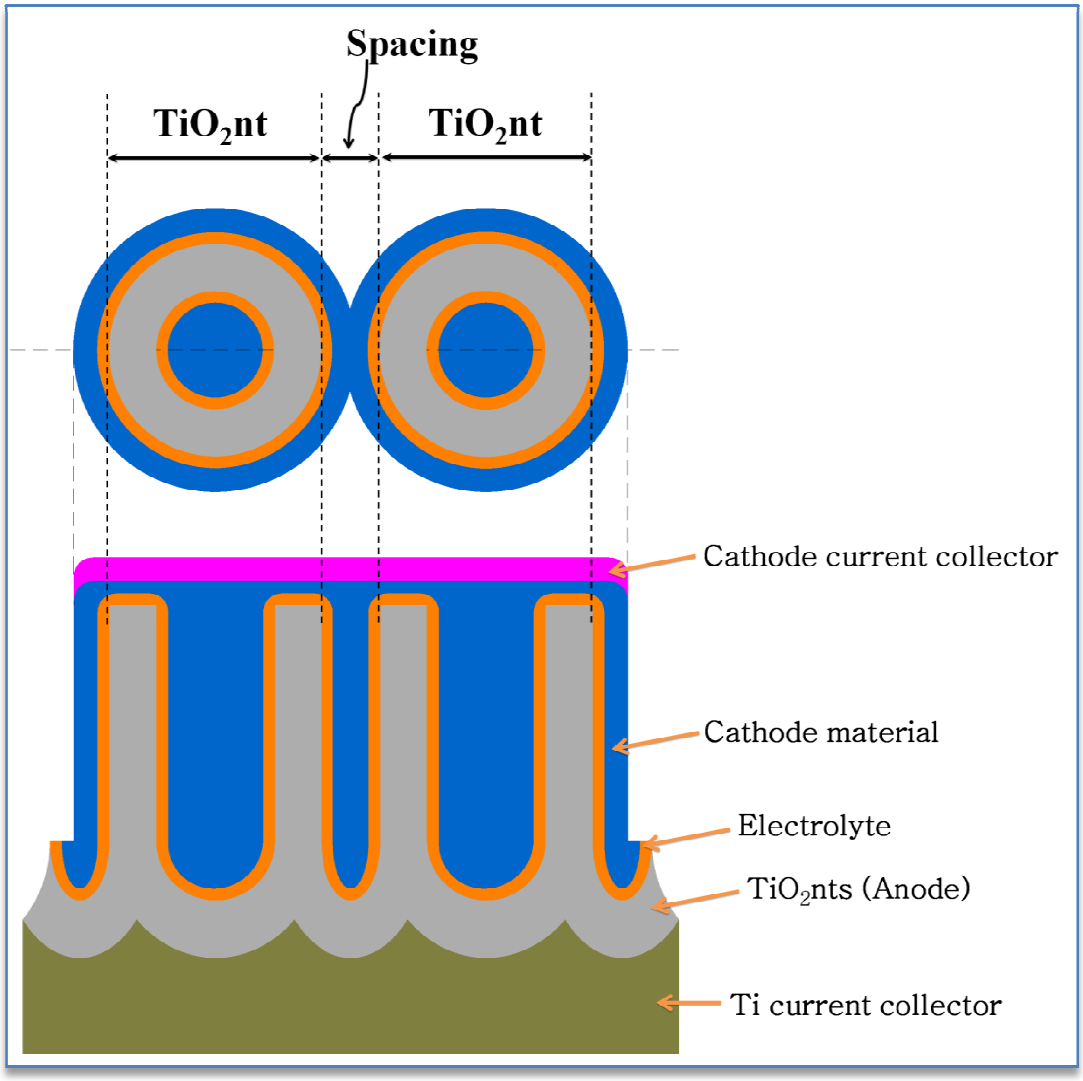

Figure 4 The targeted 3D design with TiO_2 nanotubes [Down: Cross-section; Up: top-view].

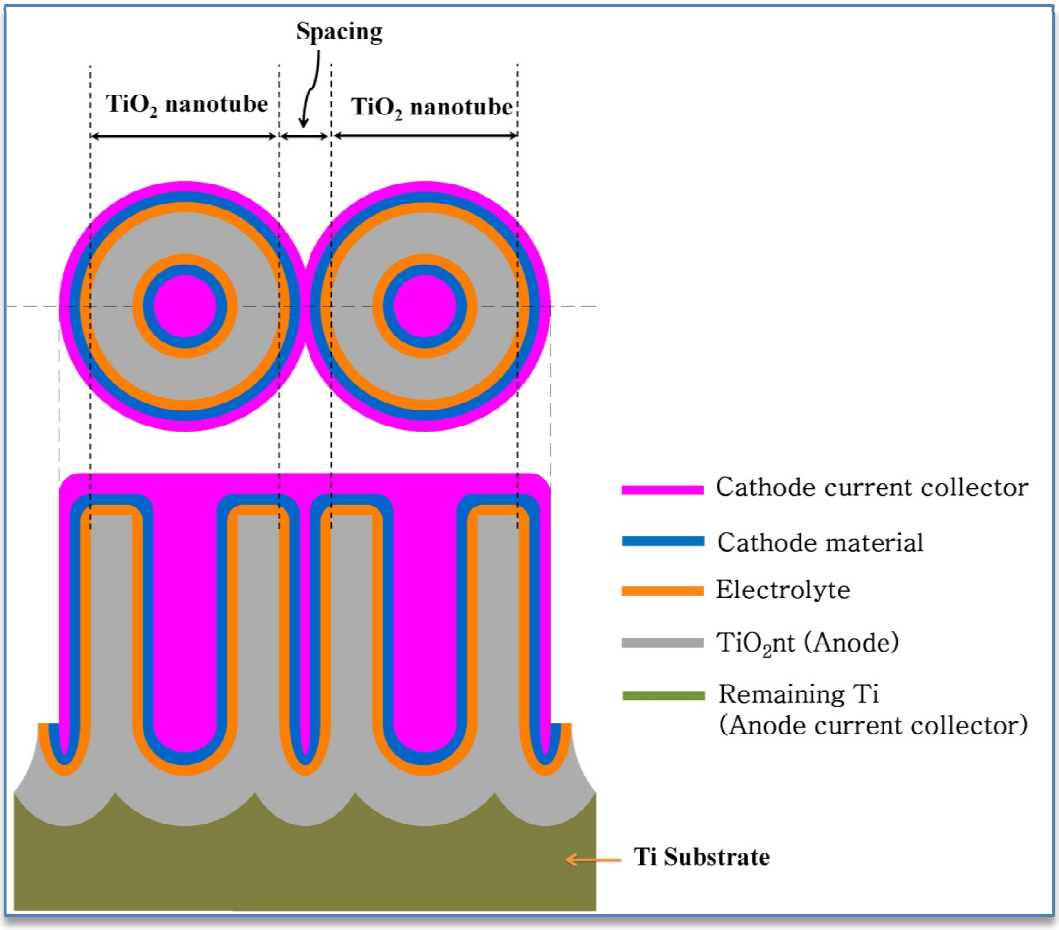

Figure 5 The second possible 3D design with TiO_2 nanotubes [Down: Cross-section; Up: top-view].

Besides the self-organised nano-architecture, TiO_2 is non-toxic and inexpensive, and the nanotubes have been demonstrated to exhibit very good capacity retention (as anode materials) particularly at moderate kinetic rates[42, 43, 55]. Despite these promising characteristics of TiO_2 nanotubes, their overall performance can be improved for the potential design of high-performance 3D Li-ion microbatteries since TiO_2 (anatase or rutile) effectively inserts only 0.5 Li^+ per formula unit, corresponding to a theoretical capacity of 168 mAh/g[43, 55, 56].

In this work,

- TiO_2 nanotubes and their derivatives will be synthesized and characterized, and their electrochemical behaviour versus lithium will be evaluated in lithium test cells.

- Electrodeposition of polymer electrolytes into the synthesized TiO_2 nanotubes will be studied; the interphase morphology and the electrochemical behaviour of the resulting material will be evaluated and compared to similar TiO_2 nanotubes with LiPON solid electrolyte deposited by RF-Magnetron sputtering.

CHAPTER TWO

2. LITERATURE REVIEW

2.1. Electrochemical Energy Storage

The indispensability of electrical energy is such that its storage and transport must be effectively achieved. Capacitors allow its direct storage but in very small quantities in relation to the demand of most applications thus it also remains another interesting area of research [57, 58]. On the other hand, batteries suitably achieve this much coveted energy storage by employing chemical compounds as the storage media. In principle, a battery is a device that converts the chemical energy contained in its active materials directly into electrical energy by means of an electrochemical reaction. As the battery electrochemically converts chemical energy into electric energy, it is not subject, as are combustion or heat engines, to the limitations of the Carnot cycle dictated by the second law of thermodynamics. Batteries, therefore, are capable of having higher energy conversion efficiencies[59].

For a number of battery systems, the electrochemical process can be reversed and the battery recharged, i.e. the intake of electrical energy can restore the chemical composition that contains higher energy, and can closely re-establish the original structures within the battery. This leads to the following classification:

i. Primary batteries— which convert their chemical energy into electrical energy only once.

ii. Secondary batteries— which are reversible energy converters and designed for repeated discharges and charges.

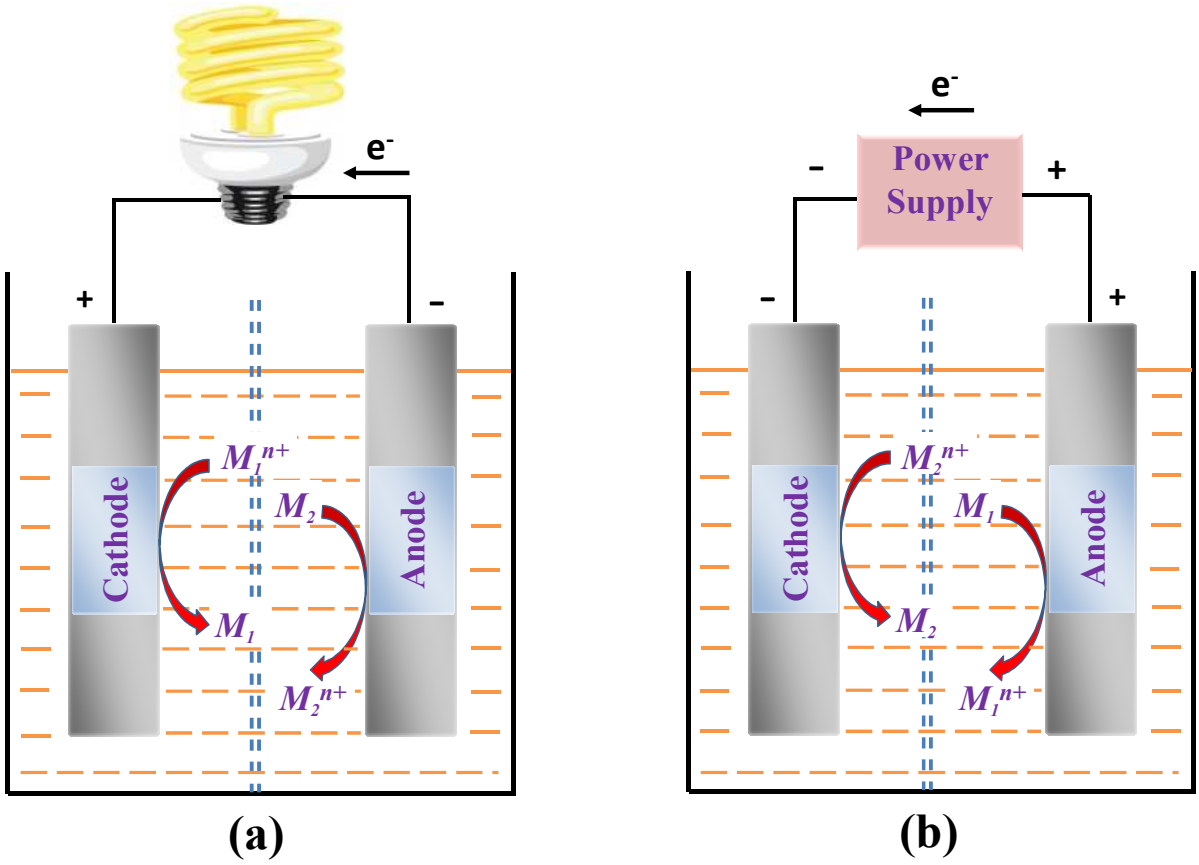

Figure 6 The electrochemical operation of a cell during (a) discharge (Galvanic), and (b) charge (Electrolytic)[59].

The term ‘‘battery’’ is often used but the basic electrochemical unit being referred to is the ‘‘cell’’. A battery actually consists of at least two electrochemical cells connected in series or parallel, or both, depending on the desired output voltage and energy.

The cell consists of three major components:

1. The anode or negative electrode—which gives up electrons to the external circuit and is oxidized during the electrochemical reaction.
2. The cathode or positive electrode—which accepts electrons from the external circuit and is reduced during the electrochemical reaction.
3. The electrolyte—the ionic conductor (electronic insulator)—which provides the medium for transfer of charge, as ions, inside the cell between the anode and cathode.

The electrolyte is typically a liquid, such as water or other solvents, with dissolved salts, acids, or alkalis to impart ionic conductivity. Some batteries use solid electrolytes, which are ionic conductors at the operating temperature of the cell [59, 60].

The operation of a cell during discharge is shown schematically, in Figure 6a. When the cell is connected to an external load, electrons flow from the anode (which is oxidized) through the external load to the cathode, where the electrons are accepted and the cathode material is reduced. The electric circuit is completed in the electrolyte by the flow of electroactive species to the anode and cathode, accordingly[59].

Assuming 'M_1' and 'M_2' are the cathodic and anodic materials respectively; the discharge reaction can be written as follows:

Negative electrode: $M_2 \rightleftharpoons M_2^{n+} + ne^-$ (1)

Positive electrode: $M_1^{n+} + ne^- \rightleftharpoons M_1$ (2)

Overall reaction: $M_2 + M_1^{n+} \rightleftharpoons M_2^{n+} + M_1$ (3)

During the recharge of a rechargeable cell, the polarities are reversed and oxidation takes place at the anode (now the positive electrode) and reduction at the cathode (now the negative electrode), as shown in Figure 6b, the reactions are as follows:

Negative electrode: $M_2^{n+} + ne^- \rightleftharpoons M_2$ (4)

Positive electrode: $M_1 \rightleftharpoons M_1^{n+} + ne^-$ (5)

Overall reaction: $M_1 + M_2^{n+} \rightleftharpoons M_1^{n+} + M_2$ (6)

2.1.1. Theoretical Voltage

During the operation of a cell, the anodic and cathodic reactions occur at electrode/electrolyte interfaces. Whenever a reaction occurs, there is a decrease in the free energy of the system,

and for a galvanic cell, this change in free energy as a result of the overall reaction is expressed as:

$$\Delta G^o = -nF\Delta E^o \quad (7)$$

Where, F = Faraday's constant (96,500 C or 26.8 Ah)

n = Number of electrons involved in stoichiometric reaction

ΔE^o *= Cell electromotive force (Standard cell potential, V)*

The standard potential of the cell is determined by the type of active materials contained in the cell. It can be calculated from free-energy data or obtained experimentally. The standard potential of a cell can be calculated from the standard electrode potentials as follows:

Standard cell potential = cathode (reduction potential) – Anode (oxidation potential)

$$\Delta E^o = E^{o,+} - E^{o,-} \quad (8)$$

The cell voltage is then dependent on the standard cell potential as well as on other factors such as concentration and temperature as expressed by the Nernst equation:

$$E = E^o - \frac{RT}{nF}\boldsymbol{In}\left[\frac{a_C^c \times a_D^d}{a_A^a \times a_B^b}\right] \quad (9)$$

Where, a_i *= activity of relevant species*

R = gas constant

T = absolute temperature for the reaction: $aA + bB \rightarrow cC + dD$

The change in the standard free energy, ΔG^o, of a cell reaction, is the driving force which enables a battery to deliver electrical energy to an external circuit. The measurement of the electromotive force, incidentally, also makes available data on changes in free energy, entropies and enthalpies together with activity coefficients, equilibrium constants, and solubility products. Direct measurement of single (absolute) electrode potentials is considered practically impossible. To establish a scale of half-cell or standard potentials, a reference

potential ‘‘zero’’ must be established against which single electrode potentials can be measured. By convention, the standard potential of the $H_2/H^+_{(aq)}$ reaction is taken as zero and all standard potentials are referred to this potential[59].

2.1.2. Theoretical Capacity

The theoretical capacity of a cell is determined by the amount of active materials in the cell. It is expressed as the total quantity of electricity involved in the electrochemical reaction and is defined in terms of coulombs or ampere-hours. The ‘‘ampere-hour capacity’’ of a battery is directly associated with the quantity of electricity obtained from the active materials. Theoretically, 1 gram-equivalent weight of material will deliver 96,487 C or 26.8 Ah. (A gram-equivalent weight is the atomic or molecular weight of the active material in grams divided by the number of electrons involved in the reaction) Similarly, the ampere-hour capacity on a volume basis can be calculated using the appropriate data for ampere-hours per cubic centimetre[59].

2.1.3. Theoretical Energy

The capacity of a cell can also be considered on an energy (watthour) basis, by taking both the voltage and the quantity of electricity into consideration.

$$\textit{Watthour (Wh)} = \textit{voltage (V)} \times \textit{ampere-hour (Ah)} \qquad (10)$$

This theoretical energy value corresponds to the maximum energy that can be delivered by a specific electrochemical system[59].

2.2. The Lithium-ion (Li-ion) Technology

It is an undisputable fact that the interest in lithium secondary batteries was as a result of the quite promising performance of lithium primary batteries since the 1970s[59]. In Figure 7 is shown a schematic of a Li secondary cell during discharge. Although the Li secondary batteries delivered outstanding energy densities, the problem of dendrite growth and the concomitant short circuit/explosion posed severe safety issues. Hence, lithium-ion batteries were developed. Lithium-ion batteries are made of cells that employ lithium intercalation compounds as the positive and negative electrodes. The conventional positive electrode and negative electrode materials for lithium–ion batteries are $LiCoO_2$ (with a layered structure) and graphite (also a layered material) respectively, with current collectors of aluminium (cathode) and copper (anode)[59]. Figure 8 shows a schematic of the "rocking–chair" electrochemical process that occurs in a Li-ion cell during discharge. The lithium–ions are exchanged between the positive and negative electrodes via a lithium conducting (electronically insulating) electrolyte, as described in Eqs. (11)-(13).

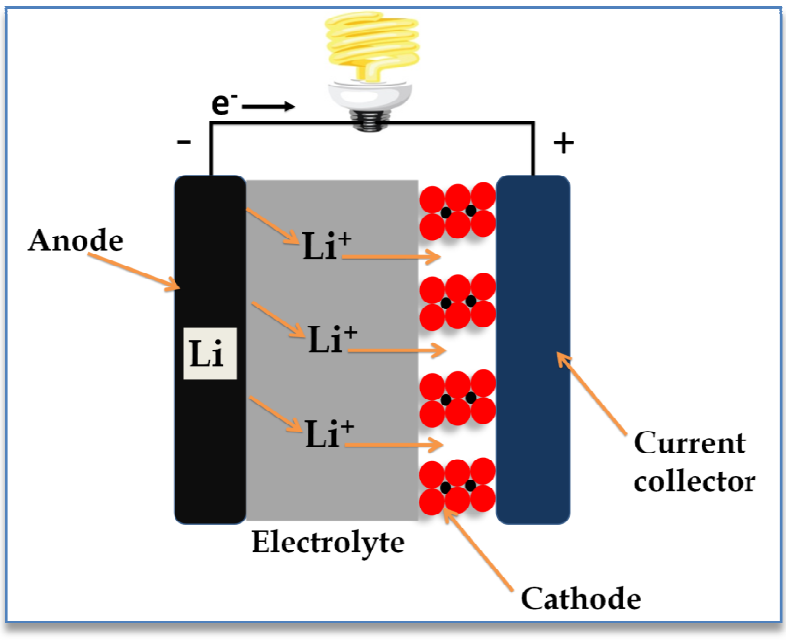

Figure 7 Schematic representation of a Li secondary cell during discharge.

Like most innovations, numerous scientists worldwide contributed to the development of the lithium-ion technology. Before the studies of Whittingham and co-workers[13, 61-63] from 1975 on the reversible intercalation of lithium into titanium disulfide, Bell labs had already developed works on the reversible reaction of lithium with metal chalcogenides in the early 1970s[64, 65]. After a few years, the electrochemical intercalation of lithium into graphite was demonstrated by Basu *et al*.[66, 67], and Yazami R. and Touzain P.[68]. It is important to note that over the same period, Besenhard *et al*. [69-73] did several studies on the reversible intercalation of alkali metals into graphite and cathodic oxides, demonstrating their possible energy storage characteristics. Not long after, the idea of replacing metallic lithium anode by an insertion material for a safer rechargeable energy source was realized in the laboratory by Murphy *et al.*[74] and Scrosati *et al.*[75]. Most importantly however, it was Bell labs that developed the first rechargeable battery (in 1980) fully based on intercalation chemistry–avoiding a metallic lithium anode and the concomitant safety issues[76]. The battery was based on a fused-salt electrolyte, and the positive electrode material was open to any of FeS, FeS_2, TiS_2, $NbSe_3$, CuS, and NbS_2, with a Li intercalated graphite as the negative electrode. Later, Goodenough and co-workers[77, 78] reported the milestone work on reversible insertion of lithium into Li_xCoO_2 and manganese spinels, and as a result, Yoshino *et al*.[79] assembled a prototype cell using a carbonaceous material as anode and a layered oxide material such as $LiCoO_2$ as the cathode. Finally, it was in 1991 that the first commercial rechargeable lithium-ion battery operating at room temperature with a graphite anode and a $LiCoO_2$ cathode was released by Sony[80, 81].

Since then, lithium–ion batteries have come to stay, and their impact in the world of portable electronics cannot be overemphasized. Among all the existing secondary batteries, lithium ion (Li-ion) batteries are being given substantial attention to date because of their

striking performance characteristics such as high energy density, absence of toxic metals (such as lead or cadmium), and lack of memory effect.

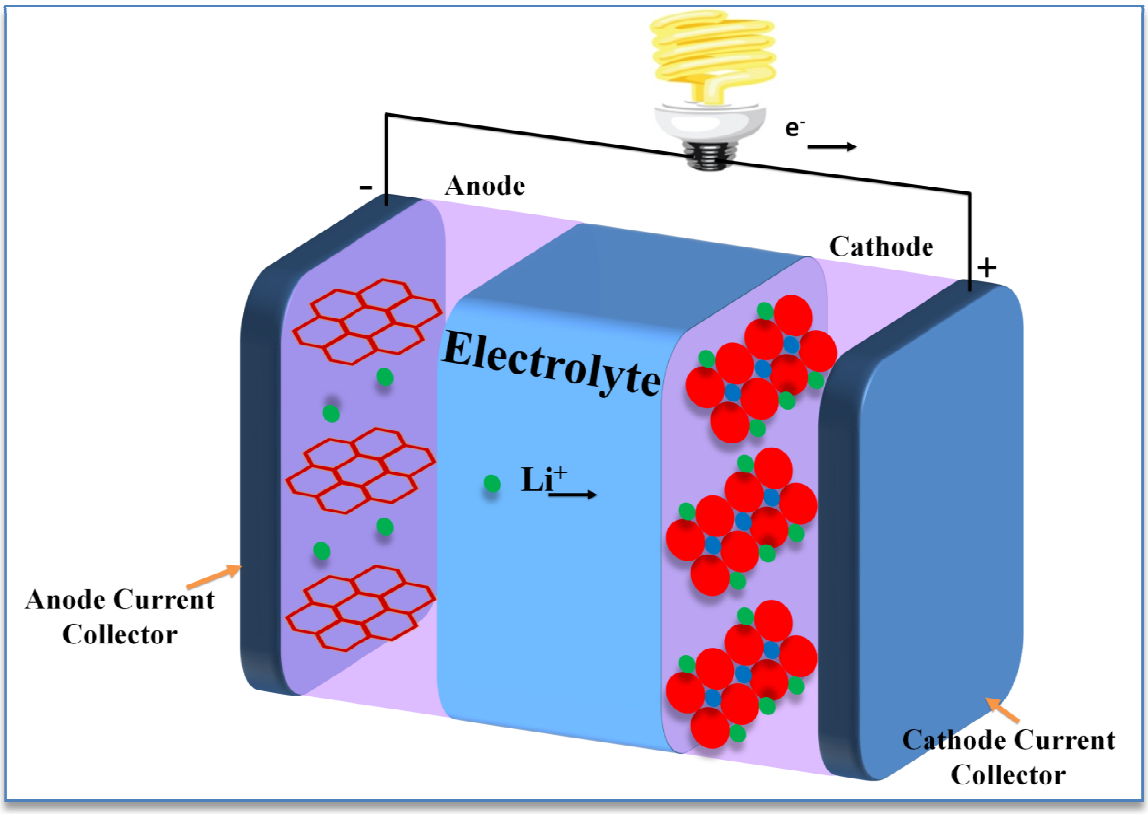

Figure 8 Schematic representation of a Li-ion cell during discharge.

$$\textit{Positive}: \quad LiMO_2 \rightleftharpoons Li_{1-x}MO_2 + xLi^+ + xe^- \qquad (11)$$

$$\textit{Negative}: \quad C + Li^+ + xe^- \rightleftharpoons Li_xC \qquad (12)$$

$$\textit{Overall}: \quad LiMO_2 + C \rightleftharpoons Li_xC + Li_{1-x}MO_2 \qquad (13)$$

Concerning the electrolyte for lithium–ion batteries, four different kinds have been established: liquid, gel, polymer, and ceramic electrolytes. Liquid electrolytes are solutions of a lithium salt in organic solvents, typically carbonates. A polymer electrolyte is a liquid- and solvent-free material, where an ionically conducting phase is formed by dissolving a salt in a high molecular weight polymer, whereas a gel electrolyte is an ionically conductive material

wherein a salt and a solvent are dissolved or mixed with a high molecular weight polymer. Gel electrolytes developed for Li-ion batteries are typically films of PVDF-HFP, $LiPF_6$ or $LiBF_4$ salt, and carbonate solvent. Fumed silica may be added to the PVDF-HFP film for additional structural integrity. Potential advantages of polymer electrolytes include improved safety properties resulting from their low volatility and high viscosity, as they do not contain a volatile flammable solvent component. A possible advantage of gel electrolytes is that the liquid phase is absorbed within the polymer, thus less likely to leak from a battery; however, in a typical Li-ion battery employing a liquid electrolyte, the electrolyte is almost completely absorbed into the electrode and separator materials. Generally, gel electrolytes are often termed gel-polymer electrolytes, and cells that employ gel (or gel-polymer) electrolytes are termed gel-polymer or simply polymer cells. Ceramic electrolytes refer to inorganic solid-state materials that are ionically conductive and electronically insulating[59].

Although different anode and cathode materials are imperative for unprecedented performance, Li-ion batteries are still envisaged as the best energy storage systems with several characteristic advantages relative to other types of secondary batteries:

1. High specific energy (~150 Wh/kg) and energy density (~400 Wh/L) which makes them attractive for weight or volume sensitive applications.
2. High coulombic and energy efficiency.
3. No memory effect.
4. Low self-discharge rate (2% to 8% per month) thus long shelf life.
5. Long cycle life (greater than 1000 cycles).
6. A broad temperature range of operation (charge at -20 °C to 60 °C, discharge at -40 °C to 65 °C), enabling their use in a wide variety of applications.

7. Single cells typically operate in the range of 2.5 to 4.2 V, approximately three times that of NiCd or NiMH cells, and thus require fewer cells for a battery of a given voltage.
8. Li-ion batteries can offer high rate capability. Discharge at 5C continuous, or 25C pulse, has been demonstrated.

Nevertheless, Li-ion batteries have some shortcomings in that they degrade when discharged below 2 V and may vent when overcharged as they do not have a chemical mechanism to manage overcharge, unlike aqueous cell chemistries. Li-ion batteries typically employ management circuitry and mechanical disconnect devices to provide protection from over-discharge, overcharge or over-temperature conditions. Also, Li-ion batteries permanently lose capacity at elevated temperatures (65 °C) but at a lower rate than most NiCd or NiMH products[59].

2.3. Titanium Dioxide

2.3.1. Occurrence, Properties and Applications

Titanium dioxide (TiO_2) occurs naturally in three main polymorphic forms (well-known minerals): anatase (space group: *I*41/*amd*), rutile (space group: *P*42/*mnm*) and brookite (space group: *Pbca*)[82]. Moreover, TiO_2 adopts five other crystal structures which generally do not occur in nature but can be synthesized chemically:

I. TiO_2 II (columbite or α-PbO_2-like structure) space group: *Pbcn*); synthesized either by a high-pressure treatment of anatase or rutile [83].

II. TiO_2 III (baddeleyite-like structure", space group: $P2_1/c$); also synthesized either by a high-pressure treatment of anatase or rutile[83].

III. TiO_2 (H) (hollandite-like structure", space group: *I*4/*m*); synthesized by topotactic oxidative extraction of potassium from $K_{0.25}TiO_2$ (hollandite)[84].

IV. TiO_2 (R) ("ramsdellite-like structure", space group: *Pbnm*)[85]; synthesized by topotactic oxidative extraction of lithium metal from $Li_{0.5}TiO_2$ (ramsdellite), and

V. TiO_2 (B) (bronze, space group: *C*2/*m*); synthesized by topotactic oxidative extraction of potassium from $K_2Ti_4O_9$ (bronze)[86]. Naturally occurring TiO_2 (B) has recently been found in Valais, Switzerland[87].

TiO_2 is a material known to be of profound industrial significance since time immemorial but of course, most of the desired applications are sensitive to certain specific polymorphic forms. TiO_2 is inexpensive, environmentally friendly and corrosion resistant, and finds applications in paint pigments[88], sunscreens[89], photocatalysis (oxidation of organic pollutants, water splitting, air purification etc.)[90, 91], electrocatalysis (oxidation of organic pollutants)[92], sensors[93], electrochromic devices[94, 95], photovoltaics[96, 97] and lithium-ion batteries[98, 99]. Irrespective of the polymorphic form, TiO_2 is an n-type semiconductor and that is the reason for its vast and versatile functionalities. TiO_2 tends to be oxygen-deficient at ambient temperature and pressure, and the material is thus an n-type semiconductor according to the defect equilibrium given below in Kröger-Vink notation[100]:

$$O_o \rightarrow V_o^{\circ\circ} + \frac{1}{2}O_2 + 2e' \qquad (14)$$

Moreover, TiO_2 is an indirect (wide) bandgap semiconductor and the bandgap value varies with respect to the polymorphic form. The indirect bandgap values are 3.2 eV for anatase and

3.0 eV for rutile[101-103]. In all cases however, the bandgap values are sensitive to crystallinity and quantum size effects. It is worth mentioning that unfortunately, not much bandgap information is reported for the other polymorphs of TiO_2[104].

2.3.2. Structural Description for Anatase, Rutile and Brookite

Anatase

The anatase crystal structure is body-centered tetragonal, space group $I4_1/amd$. Information about the ionic occupancy is provided in Table 1. The lattice parameters are: a = 3.785 Å and c = 9.514 Å (JCPDS: 21-1272) as given in Table 2. In the lattice, titanium atoms occupy the 4*a* octahedral sites whereas oxygen atoms occupy the 8*e* tetrahedral sites.

Table 1 Occupancy in the anatase TiO_2 structure

Atom	Wyckoff Notation	Atomic positions	Occupancy	Environment
Ti	4a	0; 0; 0	100%	Octahedral
O	8e	0; 0; 0.208	100 %	Tetrahedral
	4b	0; 0; 1/2	–	Octahedral

It consists of TiO_6 octahedra that are connected by their edges. Each octahedral shares 4 edges in the *ab*-plane, leading to large void channels perpendicular ($\perp$) to the c-axis as shown in Figure 9. It is in these voids or interstitial sites that lithium ions for example, are inserted upon electrochemical reaction with lithium[105, 106].

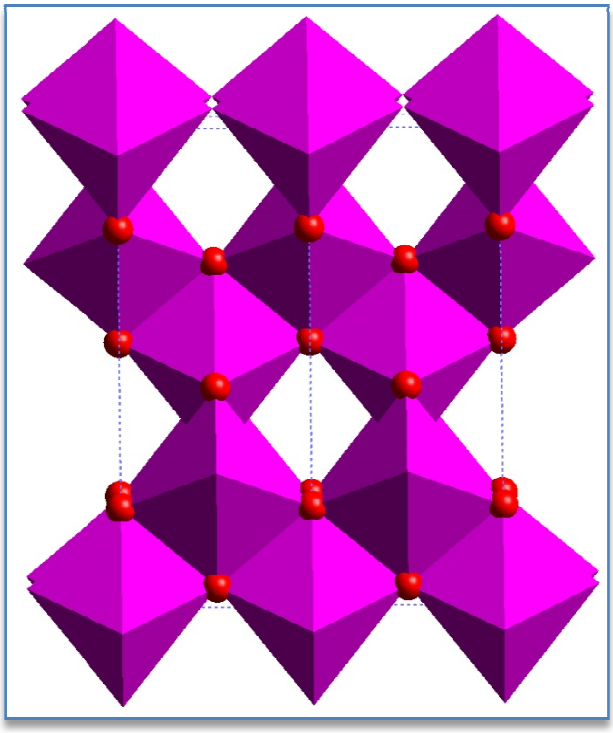

Figure 9 Co-ordination of TiO_6 octahedra in anatase

Rutile

The rutile form of TiO_2 is also tetragonal but primitive, with space group $P4_2/mnm$. The lattice parameters are: a = 4.593 Å and c = 2.959 Å (JCPDS: 21-1276) as given in Table 2. It is composed of TiO_6 octahedra which share edges along the *c*-direction and corners in the *ab*-plane as shown in Figure 10. Every octahedron shares 2 edges with other octahedra[105, 106].

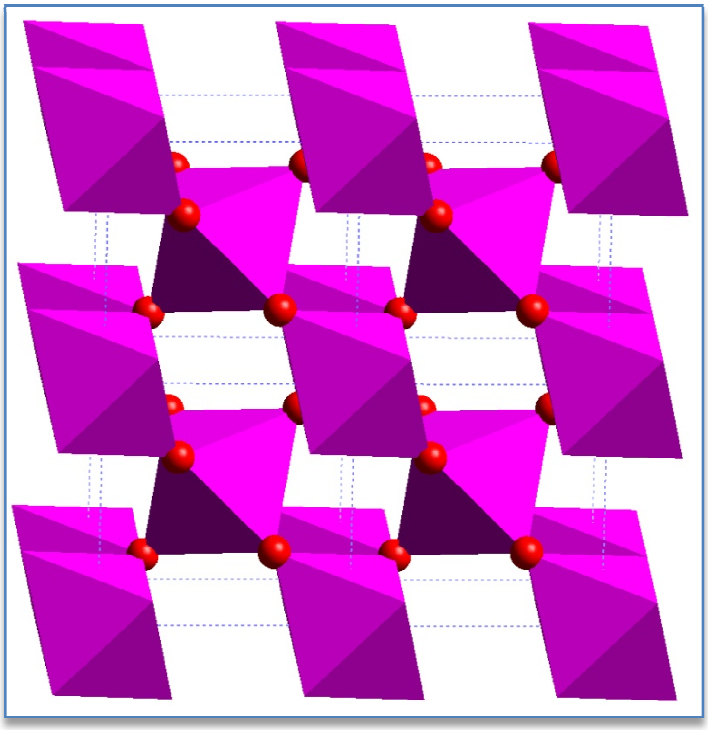

Figure 10 Co-ordination of TiO_6 octahedra in rutile

Brookite

The brookite form of TiO_2 is Orthorhombic, with space group *P*bca. The lattice parameters are: a = 5.456 Å, b = 9.182 Å, and c = 5.143 Å (JCPDS: 29-1360) as given in Table 2. The TiO_6 octahedra share edges and corners as shown in Figure 11. Every octahedron shares 3 edges with other octahedra[105, 106].

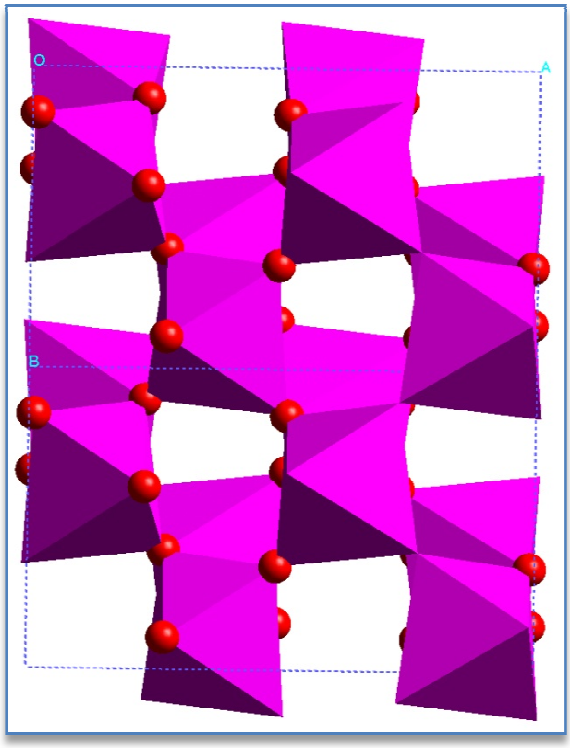

Figure 11 Co-ordination of TiO_6 octahedra in brookite

Table 2 Crystallographic data for the 3 main TiO_2 polymorphs

Polymorph	Space group	Lattice Parameters	*Z*(motif)	Density, ρ (gcm^{-3})
Anatase	$I4_1/amd$	a = 3.785 Å, c = 9.514 Å	4	3.9
Rutile	$P4_2/mnm$	a = 4.593 Å, c = 2.959 Å	2	4.25
Brookite	*P*bca	a = 5.456 Å, b = 9.182 Å, c = 5.143 Å	8	4.12

2.3.3. Titanium Dioxide Nanotubes (TiO_2nts)

Ever since carbon nanotubes (CNTs) were discovered by Iijima as an electron microscopic marvel in 1991[107], there have been immense activities related to the synthesis and applications of CNTs due to their exciting physicochemical properties (ballistic conduction, outstanding mechanical strength, quantum confinement effects etc.). The discovery of CNTs has indeed triggered countless worldwide research on other one-dimensional (1D) nanomaterials such as

inorganic nanotubes, nanowires, and nanoribbons[101]. To date, it is the nanotubes of metal–oxides that are receiving substantive attention as a result of their peculiar electronic, optical, magnetic and electrochemical properties. For example, titanium dioxide nanotubes (TiO_2nts) produced by electrochemical (anodization[108, 109]) or chemical (template-assisted[110, 111], sol–gel and hydro/solvothermal[112, 113]) routes have been shown to be extremely useful. Actually, the former synthesis route tends to be much more beneficial as it leads to self-supported nanotubes.

The electrochemical synthesis of TiO_2 nanotubes is reckoned to have started in 1979 when Kelly[114] reported on the influence of fluoride ions on the passive dissolution of titanium and resolved that the film consisted of polycrystalline TiO_2. Although possible nano-structuration was not mentioned by Kelly, it most probably could have been as a result of microscopy limitations or un-optimized experimental conditions. It was not until 1999 that Zwilling *et al*.[115, 116] reported the milestone work of fairly-organized porous structures by anodization of titanium and titanium-aluminium alloy in an electrolyte of chromic acid and hydrofluoric acid. And since 2001, significant advancements of the initial works of Kelly and Zwilling were achieved, formation of self-organised TiO_2 nanotubes were reported with fluorine-containing electrolytes of H_3PO_4, H_2SO_4, Na_2SO_4, H_3BO_3, glycerol and ethylene glycol[100, 101, 108, 117-120]. Ever since this novel material was reported, its impact in materials science has been enormous, with applications in energy storage[42, 43, 45, 121], photovoltaics[122, 123], sensors[124], catalysis[125] etc.

2.3.3.1. Mechanism of Formation of TiO_2nts by Electrochemical Anodization

It has been established that in the fabrication of TiO_2 nanotubes by potentiostatic anodization, the applied potential and the electrolyte composition play very important roles[101, 108]. With a

suitable potential and a fluoride-free electrolyte, a compact (non-porous) TiO_2 layer would be obtained with a typical current–time profile represented in a dashed line (– – –) in Figure 12; whilst TiO_2 nanotubes would be formed in fluoride-containing electrolytes with a typical current–time profile represented in a solid line (——) in Figure 12.

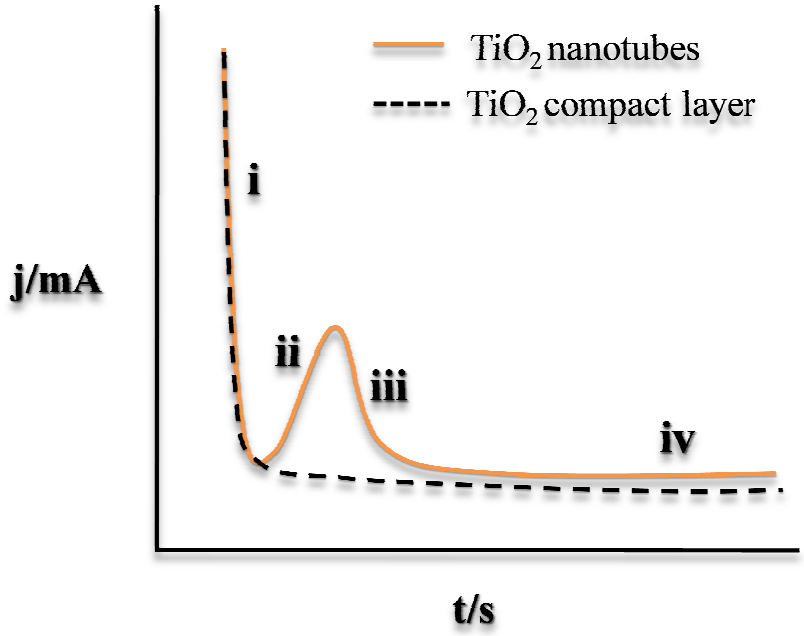

Figure 12 Typical current–time (j–t) curves recorded during the potentiostatic anodization of Ti in fluoride-free (– – –) and fluoride-containing (——) electrolytes.

The current–time profile characteristic of TiO_2 nanotubes formation can be divided into four (i-iv) stages as shown in Figure 12[42, 108]. The corresponding stepwise morphologies are also schematically given in Figure 13a-f. In stage i, the current decays due to instantaneous passivation of the titanium surface, according to Eq. (15), immediately after applying the potential. The current density then increases (after ~150 s; stage ii) due to the formation of pits on the formed barrier oxide layer by a chemical dissolution mechanism (Eq. (16)) and the concomitant increase in surface area. Afterwards, the current density decreases (stage iii) as the pits grow into uniformly–spread pores over the surface and increase diffusion length for the reacting ionic species. Finally, the pores grow into nanotubes at stage iv, where the current

becomes almost constant as a result of a competition between electrochemical oxide formation and chemical dissolution.

$$Ti + 2H_2O \rightarrow TiO_2 + 4H^+ + 4e^- \quad (15)$$

$$TiO_2 + 6F^- + 4H^+ \rightarrow TiF_6^{2-} + 2H_2O \quad (16)$$

$$Ti \rightarrow Ti^{2+} + 2e^- \qquad ; E^o = -1.63 V_{/SHE} \quad (17)$$

$$Ti^{2+} + 2H_2O \rightarrow TiO_2 + 4H^+ + 2e^- \; ; E^o = -0.502 V_{/SHE} \quad (18)$$

The basic processes responsible for anodic formation of nanoporous alumina[126-129] and titania[115, 130] appear to be the same, and are fundamental to the formation of vertically oriented titania nanotubes. The key processes are: (i) Oxide growth at the surface of the metal occurs due to enhanced interaction of the metal with O^{2-} anions (generated by field-assisted de-protonation of H_2O or OH^-). Although the titanium oxide formation is commonly described by Eq. (15), it is thermodynamically a two-step process, that is, Eq. (15) is a sum of Eq. (17) and Eq. (18), leading to E^o = –1.066 $V_{/SHE}$. Once the initial oxide layer is formed, O^{2-} anions migrate through the oxide layer to the metal/oxide interface for further reaction with the metal, as shown in Figure 14. (ii) Ti^{4+} cations migrate from the metal/oxide interface towards the oxide/electrolyte interface under the existing electric field, as shown in Figure 14. (iii) Field-assisted dissolution of the oxide occurs incessantly at the oxide/electrolyte interface[129, 131]. Due to the applied electric field, the Ti–O bond undergoes polarization and is weakened, promoting dissolution of the metal cations[132, 133]. (iv) Chemical dissolution or top-etching of the oxide also takes place at the oxide/electrolyte interface (according to Eq. (16)) as a function of the concentration of the F^- anions in the electrolyte. The chemical dissolution effect of the F^- anions plays a key role in the formation of nanotubes instead of a non-porous or a nanoporous layer[108].

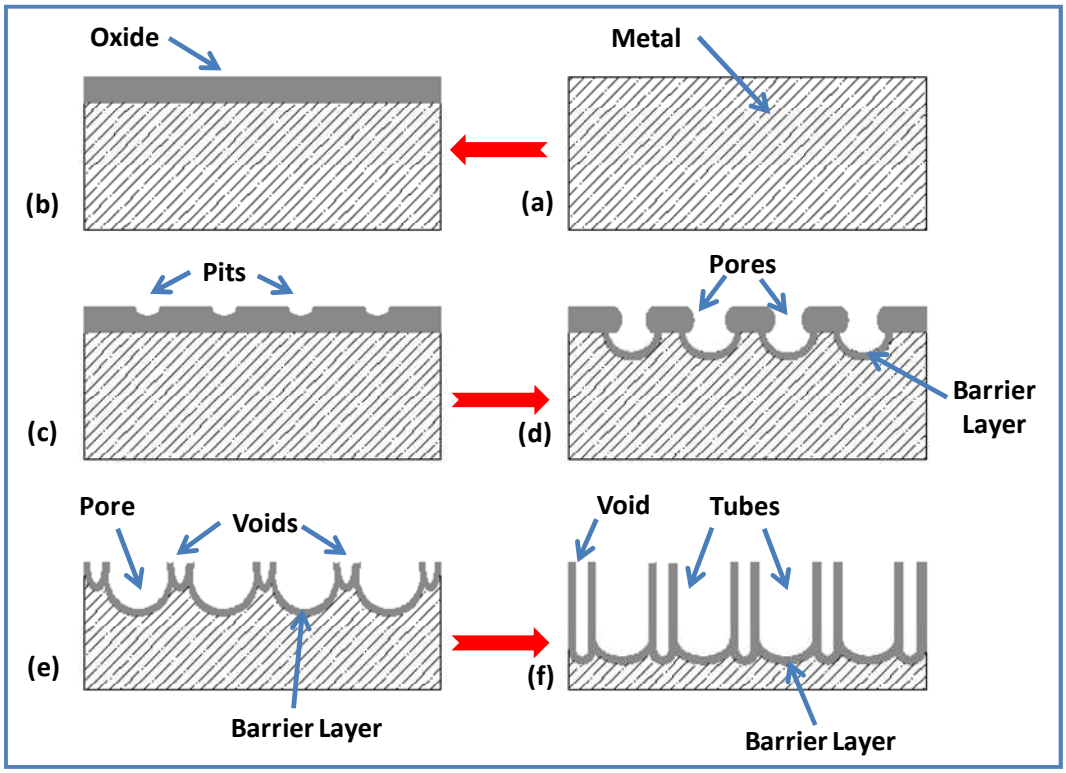

Figure 13 Schematic depicting the stages of formation of TiO_2 nanotubes during potentiostatic anodization: (a) starting metal, (b) initial oxide layer, (c) pits formed on the oxide layer, (d) pits grown into convex–shaped pores, (e) voids develop via field assisted dissolution, and (f) front view of a fully developed nanotube array[108].

During the anodization process, the rate of oxide growth at the metal/oxide interface and the rate of oxide dissolution at the oxide/electrolyte interface ultimately become equal and thereafter, the thickness of the barrier layer remains unchanged although it moves further into the metal –making the pores deeper as schematically shown in Figure 14. When nanotubes are formed, the thickness of the tubular layer ceases to increase as soon as the chemical dissolution rate of the oxide at the mouth of the tubes (top surface) becomes equal to the rate of inward movement of the metal/oxide boundary at the base of the tubes. Higher anodization voltages enhance the rates of oxidation and field-assisted dissolution and consequently, much thicker nanotubular–layers can be formed before equilibrating with the chemical dissolution. It has also been found that the nanotube diameter (d) increases with the applied voltage (V) by $d\ [nm] = k \times V$, where k equals $2 \times f_g$; f_g being the growth factor for anodic oxides and typically

between 2 and 2.5 nmV^{-1} for TiO_2 films[102]. Furthermore, no nanotubes can be formed if the chemical dissolution is too high or too low. Hence, controlling the F^- concentration is essential in achieving the desired nanotubes. Longer or shorter nanotubes can be obtained depending on the F^- concentration and also depending on if acidic electrolytes or viscous electrolytes are used[55, 101, 108].

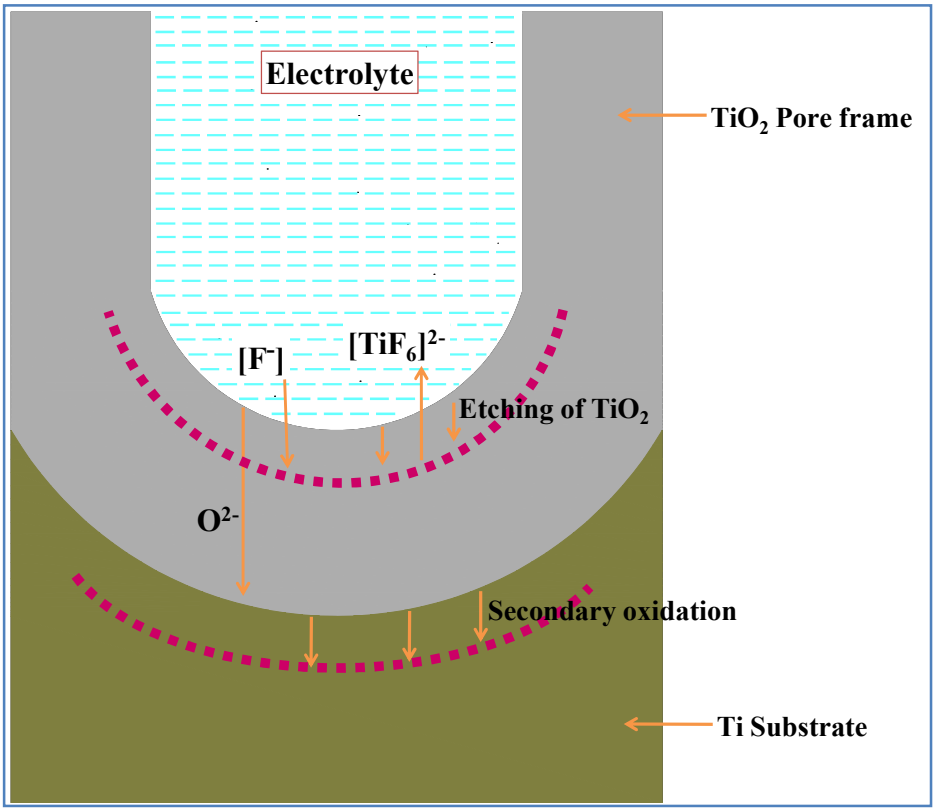

Figure 14 A schematic representation of the oxidation and etching processes that occur during the anodic growth of TiO_2 nanotubes[109].

It is important to note that self-organized nanotubes are formed because both voids and pores grow in equilibrium[108]. And the transition from a porous to nanotubular morphology during the anodization process has been proven to be initiated by the splitting (separation) of the pores along the pore frames (cell boundaries) as shown in Figure 15a-b. Actually, the cell boundaries are believed to be sensitized by a rapid accumulation of fluoride species, and consequently prone to chemical dissolution[101, 134]. The accumulation of fluoride species in the

pore walls is believed to be due to the fact that F^- anions migrate twice as fast as O^{2-} anions in the high-field barrier oxide (pore bottom), leading to fluoride–rich layers at the metal/oxide interfaces (Figure 15a-b)[135-137].

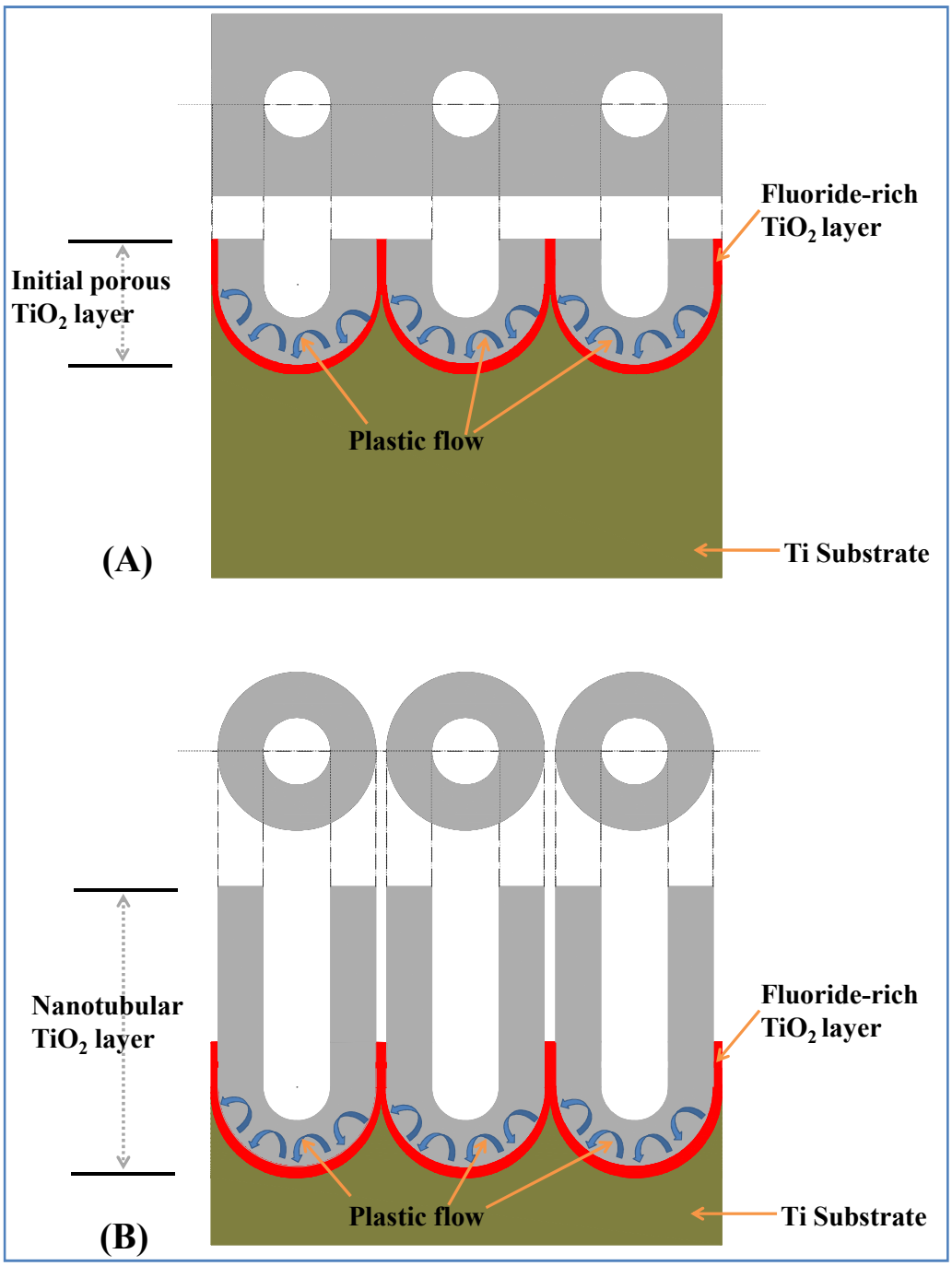

Figure 15 Schematic representation of (a) porous TiO_2 with fluoride-rich layers accumulated by plastic flow during anodization [Down: Cross-section; Up: top-view]; and (b) developing TiO_2 nanotubes [Down: Cross-section; Up: top-view] after dissolution of fluoride-rich layers.

As the fluoride–rich layer develops, it gradually gets displaced into the inter-pore frames (cell boundaries). This displacement is believed to be caused by the plastic-flow of the oxide towards the pore walls[101, 138-141]. Berger *et al.*[134] used spatial resolution scanning Auger Electron Spectroscopy (AES) to demonstrate that a fluoride–rich layer still existed in between the tube walls of as-anodized TiO_2 nanotubes.

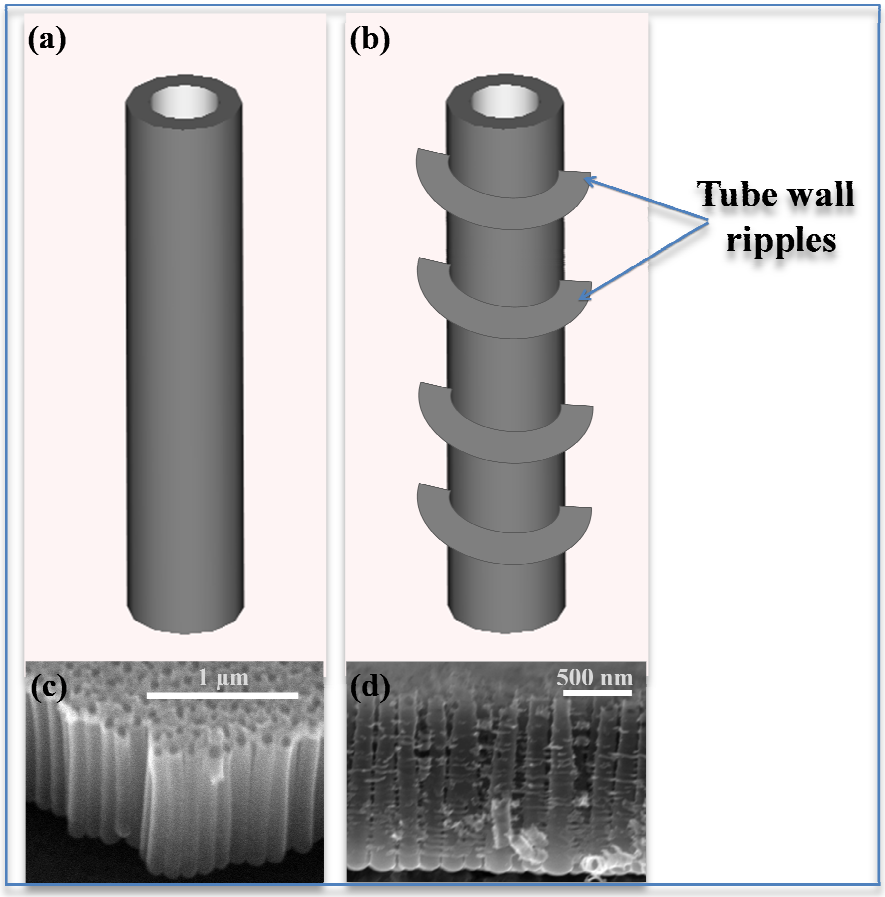

Figure 16 Schematic representations of a smooth TiO_2 nanotube (a) and a rugous TiO_2 nanotube (b); with the corresponding exemplary SEM images (c: 2% H_2O, d: 10% H_2O).

Apart from the applied potential and the fluoride concentration, the water content of the electrolyte also has a pronounced impact on the morphology of the nanotubes. The water content indeed controls the rates of oxide formation and oxide etching (chemical dissolution) during the growth of the nanotubes. Strikingly, electrolytes of lower water contents lead to nanotubes of very smooth walls (Figure 16 a and c), whereas significant side wall ripples are

formed with higher water contents[43, 100, 109, 119, 142-144]. The reason being that for higher water contents, the fluoride-rich layers between the tubes show a faster etching rate (chemical dissolution) than the growth rate of the oxide into the underlying substrate. The ripples on the walls of such nanotubes (Figure 16 b and d), therefore, represent the footprint of the number of rapid dissolutions (of the fluoride-rich layers) that occurred during the anodization process.

Another important parameter in the fabrication of TiO_2 nanotubes by electrochemical anodization is the pH of the electrolyte. In acidic electrolytes (low pH), top etching proceeds much faster and thus the tubes have lengths limited to 500–900 nm[42, 43]. In neutral electrolytes, 2–4 μm thick nanotubes can be obtained owing to reduced top etching[101, 145]. However, top etching is greatly mitigated in viscous electrolytes (glycerol or ethylene glycol based systems), leading to very thick (up to7 μm) nanotubes [142, 146]. Concerning the anodization technique, it has been proven that although tubes can in principle, be grown by galvanostatic (constant current) anodization [147], the method has the drawback that the voltage may change with time and the control over the tubes' morphology would be lost. In the work of Taveira *et al.*[147], it was demonstrated that during constant current anodization, the voltage indeed increases and fluctuates with time. It was also confirmed that tubular growth occurred up to a critical voltage after which the layer exfoliated and a new layer began to form. Other techniques such as voltage pulse anodization[148] or sono-electrochemical anodization[149] have some interesting effects but the nature of the resulting nanotubes are not overly different from the conventional constant voltage routes.

By optimizing the electrochemical conditions, organized nanotubular or nanoporous structures can be developed for several other valve metals such as Zr[150, 151], Hf[152, 153], W[154], Nb[155, 156], Ta[157-159], V[160, 161] and now, the technique is evolving to be transferrable to other transition metals[162-164] and even alkali earth metals[165].

CHAPTER THREE

3. MATERIALS AND EXPERIMENTAL

3.1. Thin Film Deposition by Physical Vapour Deposition (PVD)

Metallic targets (Ti, Fe and Sn, 99.9% pure) were supplied by Sigma-Aldrich. In addition to depositing pure Ti thin films, co-sputtering was employed for Fe or Sn incorporation into the Ti thin films when it was desired. For the co-sputtering, Ti, Fe or Sn targets were cut into the right proportions (considering the sputtering rates of Ti, Fe or Sn in relation to the anticipated thin film composition), cleaned and assembled in a target holder with the aid of a silver paste as schematically shown in Figure 17.

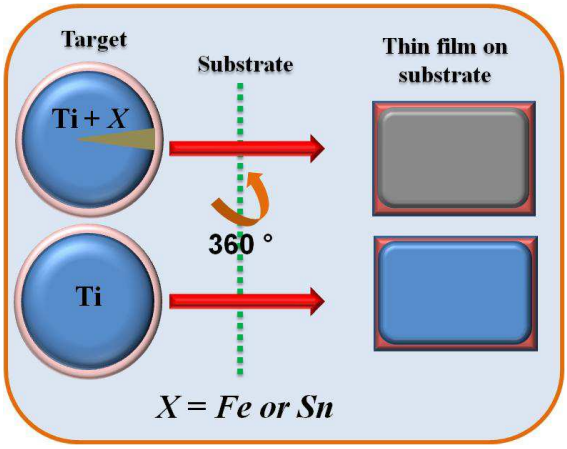

Figure 17 Schematic representation of target preparation for incorporating Fe or Sn into Ti thin films by co-sputtering and substrate rotation.

The target, after drying overnight at room temperature, was inserted into the PVD chamber. Mirror polished silicon wafers (p-type Si with a resistivity of 1–10 Ωcm [WaferWorld, Inc.]) were cut to size (along the (100) crystallographic plane) and cleaned by sonicating sequentially with acetone, isopropanol, and methanol, for 10 min each. Any oxide layer was then removed by dipping the Si wafers in HF solution of 1 wt % for 1 min followed by rinsing

with distilled water and drying with compressed air. The cleaned Si substrates were immediately inserted into the PVD chamber which was subsequently pumped for a high vacuum (10^{-6} mbar).

Thin films (Ti or Ti-Fe or Ti-Sn) of ~1.8 μm thickness were deposited by cathodic sputtering onto the silicon substrates. The substrates were constantly rotated (360°) during the deposition to ensure a uniform thin film composition. An ultrapure Ar atmosphere was maintained inside the deposition chamber at a pressure of 6×10^{-4} mbar during the deposition with a current of 150 mA.

3.2. Anodization Experiments

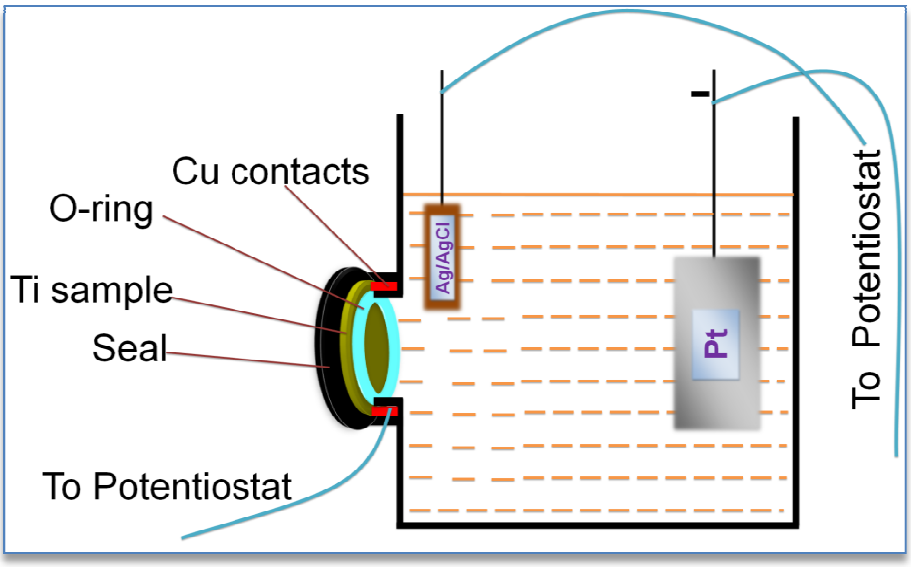

Figure 18 Schematic representation of the cell used for the electrochemical experiments.

Anodization was carried out by applying a constant voltage (5 or 20 or40 V, where necessary) to Ti foils (99.9% pure), Sn foils (99.9% pure) or thin films (Ti or Ti–Sn or Ti–Fe) for the required period of time in a conventional two electrode cell using PARSTAT 2273 potentiostat/galvanostat. A platinum foil counter electrode was used (see Figure 18). The electrodes were kept 3 cm apart and the electrolyte was either aqueous (1 M H_3PO_4 + 1 M

NaOH + 0.4 wt% HF) or viscous (88.7 wt% glycerol + 1.3 wt% NH_4F + 10 wt% H_2O) depending on the nature of the working electrode (Ti foil, Sn foil or Ti/Ti–Sn/Ti–Fe thin films).

3.3. Electrodeposition

Metal electrodeposition was carried out on TiO_2nts layers using aqueous electrolytic baths containing Co^{2+} or Ni^{2+} electroactive species. The bath (pH = 5) consisted of a mixture of 0.09 M $CoSO_4$ (Sigma-Aldrich, 98%) or 0.09 M $NiSO_4$ (Sigma-Aldrich, 97%) and 0.1 M $(NH_4)_2SO_4$ (Alfa Aesar, 99%) solutions prepared with ultrapure water (18 MΩcm). The electrodeposition experiments were carried out galvanostatically using an EG&G PARSTAT 2273 potentiostat/galvanostat with a current density of -2.6 $mAcm^{-2}$ during a short time (120 s). The deposition solutions were de-aerated under nitrogen flow for 10 minutes. A platinum foil counter electrode and an Ag/AgCl reference electrode were used.

3.4. Thermal Treatments, XRD, SEM, EDS and TEM

Optional thermal treatments at 400–500 ºC (depending on the material) were performed in air during 4 h. X-ray diffraction patterns were recorded (with a step-time of 10 s and step size of 0.02°) at room temperature using a Siemens D5000 diffractometer with Cu Kα radiation (λ = 1.5406 Å). EDS analysis and scanning electron microscopy imaging were carried out with a Philips XL-30 FEG SEM. For transmission electron microscopy, the nanotubes were carefully scratched directly onto copper grids and the imaging was done using a JEOL 2010F transmission electron microscope.

3.5. Polymer Deposition and Characterization (FTIR, GPC, NMR and Mass spectrometry)

Samples of nanotubes were used as the working electrodes for electropolymerization by

cyclic voltammetry, which involved sweeping at 25mV/s from 0V to -2.5V with a reverse scan using saturated calomel electrode (SCE) as reference. Cathodic polarization curves were recorded using EG&G PARSTAT 2273 potentiostat/galvanostat. The electrolyte was a 0.035M lithium bis(trifluoromethanesulfone)imide (LiTFSI) aqueous solution. Lithium bis(trifluoromethanesulfone) imide, $LiN(CF_3SO_2)_2$, (LiTFSI) is the prototype of a new family of bulky lithium salts with bulky anions combining great charge delocalization favourable forionic dissociation in a solvating polymer such as PEO, good chemical, electrochemical and thermal stabilities and also a plasticizing effect which decreases the crystallinity of the host polymer and enhances ionic mobility easier. This $LiN(CF_3SO_2)_2$ salt with 99.0% purity was used as received from Sigma-Aldrich. After purging the electrolyte solution with nitrogen gas for 10 minutes, 2g of PEO-functionalized methyl methacrylate monomers (MMA-$(PEO)_n$ with n=475 used as received from Aldrich) was added. After electropolymerization, the samples were dried in an oven at 60°C to remove the residual water content of the polymer.

FTIR spectroscopy in the range of 4000 to 400 cm^{-1} was performed using Equinox 55 Brucker in the diffuse reflectance mode.

^1H NMR spectra were determined on a Bruker Advance DPX 400 MHz spectrometer of the Spectropole of Aix Marseille University at room temperature in 5 mm o.d. tubes. The ^1H chemical shifts were referenced to the solvent peak: $CDCl_3$ (7.26 ppm). The determinations of polymer molecular weights and molecular weight distribution were performed on a system composed of a Waters 717 plus auto-sampler, a Waters 600 system controller and a Waters 600 fluid unit and two detectors: A waters 2414 differential refractometer and a UV/visible detector Waters 486, both used at 40 °C. THF + 0.25%vol toluene was used as eluent at a flow rate of 0.7 $mL.min^{-1}$ after filtration on Alltech nylon membranes with a porosity of 0.2 μm. The column oven was kept at 70 °C, and the

injection volume was 20 µL. Two ResiPore columns (600 mm, 7.5 mm), Polymer Laboratories, were used in series. The system was calibrated using PS standards (Standards Varian Easical PS-2) in the range 1000–400000.

Mass spectroscopy was performed by the Spectropole of Aix Marseille University. ESI mass spectral analyses were recorded with a 3200 QTRAP (Applied Biosystems SCIEX) mass spectrometer.

3.6. LiPON (Lithium Phosphorus Oxynitride) Deposition

LiPON thin films were deposited onto TiO_2nts by rf magnetron sputtering from an Li_3PO_4 target in a pure N_2 atmosphere with a BAK550 (Balzers) apparatus. The base pressure was 2×10^{-4} Pa. Plasma ignition was performed with argon before introduction of nitrogen. Prior to the deposition of thin films, a presputtering of 30 min was performed. Targets of 7.5 cm diameter were prepared either by hot pressing or by uniaxial pressing (at room temperature) of a commercial Li_3PO_4 powder (Aldrich, 99.9%).

3.7. Mössbauer Spectroscopy

^{119}Sn room temperature Mössbauer spectra were recorded in the constant acceleration mode and Conversion Electron Mössbauer Spectroscopy (CEMS) geometry. A specific helium-flow counter was used for the detection of conversion electrons. The γ-ray source consisted of $Ba^{119m}SnO_3$ with a nominal activity of 7 mCi. The hyperfine parameters, isomer shift (δ) and quadrupole splitting (Δ) were determined by fitting appropriate Lorentzian lines to the experimental data. The quality of the fit was controlled by the usual χ^2-test. All isomer shifts for Sn are given relative to $BaSnO_3$ at room temperature.

3.8. X-ray Photoelectron Spectroscopy

XPS measurements were carried out with a Kratos Axis Ultra spectrometer, using focused monochromatized Al Kα radiation (hν = 1486.6 eV). The XPS spectrometer was directly connected to an argon dry box through a transfer chamber, to avoid moisture/air exposure of the samples. The analyzed area of the samples was 300 µm x 700 µm. Peaks were recorded with constant pass energy of 20 eV. The pressure in the analysis chamber was around 5 x 10^{-8} Pa. Short acquisition time spectra were recorded before and after each normal experiment to check that the samples did not suffer from degradation under the X-ray beam during measurements. Peak assignments were made with respect to experimental reference compounds, namely bulk anatase and/or rutile TiO_2. The binding energy scale was calibrated from hydrocarbon contamination using the C 1s peak at 285.0 eV. Core peaks were analyzed using a non linear Shirley-type background. The peak positions and areas were optimized by a weighted least–square fitting method using 70% Gaussian and 30% Lorentzian line-shapes. Quantification was performed on the basis of Scofield's relative sensitivity factors.

3.9. Mott-Schottky Analysis

Mott-Schottky analysis was carried out in a 0.1 M Na_2SO_4 solution using an Ag/AgCl reference electrode and a platinum foil counter electrode, with the studied nanotubes as working electrodes. The potential was changed in 0.1 V voltage steps and the impedance was determined at 30 Hz fixed frequency with 10 mV a.c. amplitude using an EG&G PARSTAT 2273 potentiostat/galvanostat.

3.10. Electrochemical Measurements

For the electrochemical measurements, two-electrode Swagelok-type cells (see Figure 19) were assembled in a glove-box filled with purified argon in which moisture and oxygen contents were less than 2 ppm. The galvanostatic experiments were then carried out with

the prepared Li/$LiPF_6$ (EC:DEC)/W_E (Working electrode) cells using a VersaSTAT 3 potentiostat/galvanostat. The electrolyte supplied by Merck was embedded in a Whatman glass microfiber, which acts as a separator. It is remarkable to note that additives such as poly(vinyl difluoride) that is a binding agent, and carbon black (conductive agent) were not utilized. For the discharge/charge, a constant current density of 70 μAcm^{-2} (1C) was applied to the assembled cells in the $1.0 \leq U/V \leq 2.6$ or $0.05 \leq U/V \leq 3$ voltage range. Additionally, cyclic voltammetry was carried out with the VersaSTAT3 potentiostat/galvanostat in the $0.65 \leq U/V \leq 3$ or $0.05 \leq U/V \leq 3$ voltage ranges at a scan rate of 0.1 mVs^{-1}.

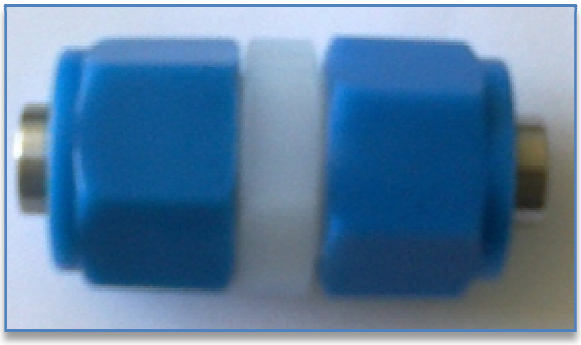

Figure 19 Two-electrode Swagelok cells used for the Li-based electrochemical measurements.

CHAPTER FOUR

4. RESULTS AND DISCUSSION

4.1. Sn Doping of TiO_2 Nanotubes

In this section, Sn doping of TiO_2 nanotubes is discussed. The effect of Sn doping on the morphology and the electrochemical behaviour of TiO_2 nanotubes will be evaluated.

To date, there were no reports in literature on the anodization of Ti-Sn alloys nor Ti-Sn thin films. Even though the anodization of pure Sn leading to porous SnO_2 was widely reported with oxalic acid electrolyte[166-170], the possibility to form self-organized nanostructures of SnO_2 is still at a deadlock.

4.1.1. Morphology, Structure and Composition

Doping of TiO_2nts with Sn was achieved by incorporating Sn into Ti thin films (by co-sputtering of Ti and Sn targets) and oxidizing the thin films by potentiostatic anodization. As the anodization of Sn (leading to porous SnO_2) was always carried out with oxalic acid electrolyte[166-170], it became imperative to first assess the behaviour of Sn under the conditions for the production of TiO_2nts. A commercially available tin foil was employed as a simple and faster alternative to achieve this assessment, considering that the quality of a sputtered pure Sn thin film is generally low (due to the low melting point [232 °C] of Sn) and as such, the morphology of anodized SnO_2 could be affected.

$$Sn + 2H_2O \rightarrow SnO_2 + 4H^+ + 4e^- \quad (19)$$

$$SnO_2 + 6F^- + 4H^+ \rightarrow SnF_6^{2-} + 2H_2O \quad (20)$$

The current-transient recorded during the potentiostatic anodization of Sn at 5 V in the electrolyte consisting of 1M H_3PO_4, 1M NaOH and 0.4 wt% HF is as shown in Figure 20. It can be seen that for the formation of porous SnO_2, the current increases right from the beginning, corresponding to an initial etching effect. The current then decreases asymptotically due to the growth of SnO_2 (Eq.(19)) combined with pore formation and propagation according to the chemical dissolution mechanism given in Eq. (20). SEM image of the resulting mesoporous SnO_2 is shown in Figure 21b. A thickness of ~2.6 µm and a pore size of ~20 nm were estimated. In an HF-free electrolyte consisting of 1M H_3PO_4 and 1M NaOH, an entirely non-porous oxide layer was obtained (*Inset*: Figure 21b). It is worth mentioning that during the anodization of Sn foil at potentials greater than 5 V, there was macroscopic dissolution of the formed SnO_2 into the electrolyte.

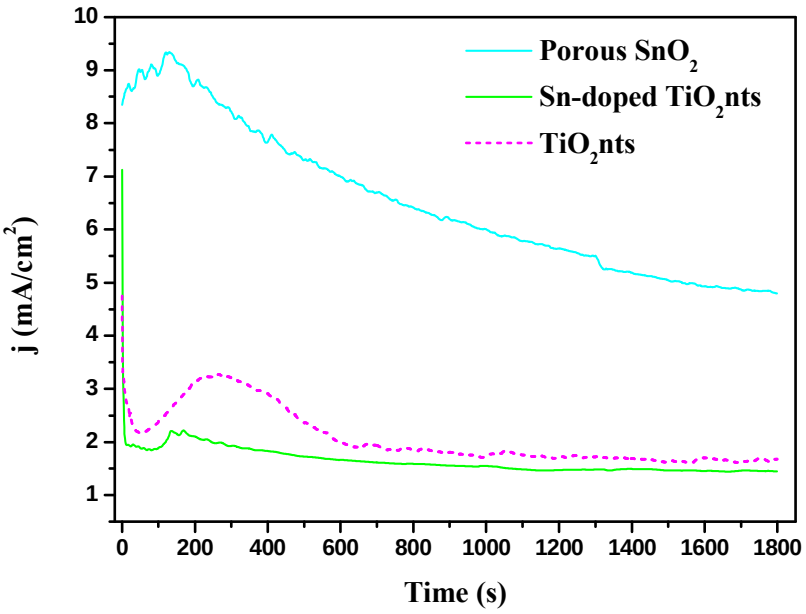

Figure 20 Current-transients recorded during the 30 min anodization of Sn foil at 5V, Ti thin film at 20 V, and Ti-Sn thin film at 20 V in the electrolyte consisting of 1M H_3PO_4, 1M NaOH and 0.4 wt% HF.

Moreover, it can be seen from Figure 21b that the mesoporous SnO_2 consists of stacked layers. This has been explained as the consequence of the vigorous oxygen evolution (under the prevailing anodizing conditions) that creates turbulence in the electrolyte and/or local

stress around the metal/oxide interface, affecting the long range order of the pores[169]. The as-prepared SnO_2 is amorphous and after annealing at 400 ºC in air during 4h, peaks corresponding to a nano-crystalline SnO_2 (Cassiterite: space group $P4_2/mnm$) could be identified as shown in Figure 24. When Sn electrodeposited onto TiO_2nt materials were annealed at temperatures not far from 400 ºC, SnO (romarchite) was obtained co-existing with metallic tin, meaning that oxidation was not complete[45, 46].

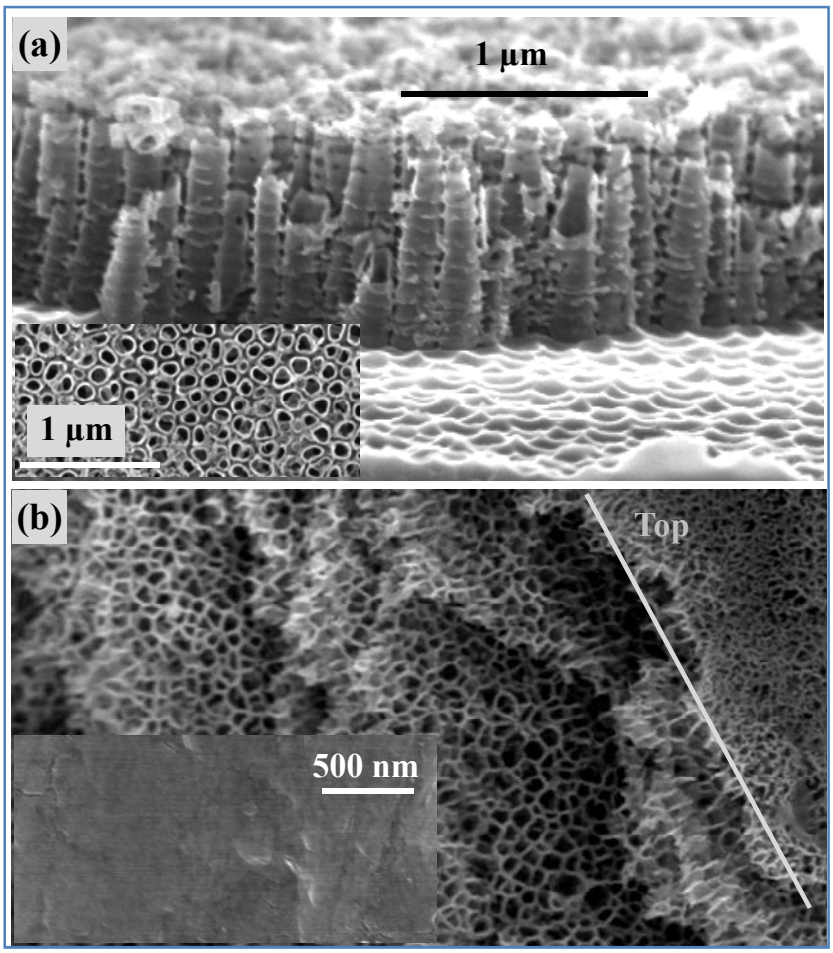

Figure 21 SEM images of TiO_2 nanotubes (a), and porous SnO_2 [*Inset*: non-porous SnO_2] (b) prepared at 20 V and 5 V respectively, in the electrolyte consisting of 1M H_3PO_4, 1M NaOH and 0.4 wt% HF.

Subsequently, pure Ti thin films (Figure 22a) were anodized at 20 V with the same electrolyte composition (1M H_3PO_4, 1M NaOH and 0.4 wt% HF) that was adopted for the production of the porous SnO_2, and the resulting current-transient is also shown in Figure 20.

It can clearly be noticed that the current–transient profile is characteristic of nanotubes formation[42, 109, 117], that is, there is a sharp drop in the anodization current in the first 100 s due to the formation of an initial insulating oxide layer followed by an increase in the current due to the formation of pits in the oxide by a chemical dissolution effect of fluoride ions and the concomitant increase in surface area.

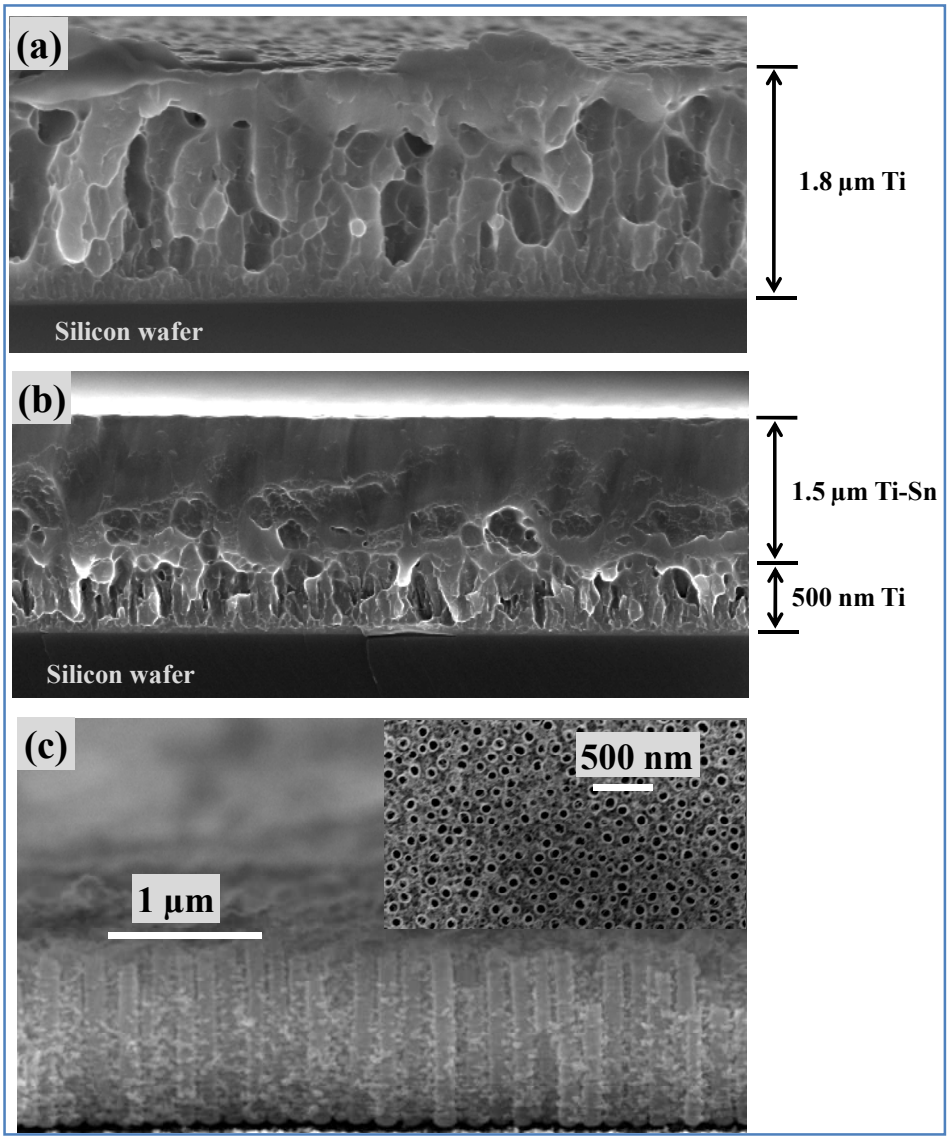

Figure 22 SEM images of (a) Ti thin film; (b)Ti-Sn thin film cross-section (with a 500 nm Ti barrier layer); and (c) Sn-doped TiO_2nts (Inset: top-view) prepared at 20 V(for 30 min) in the electrolyte consisting of 1M H_3PO_4, 1M NaOH and 0.4 wt% HF.

The current then decreases as the pits grow into uniformly–spread pores over the surface and increase diffusion length for the reacting ionic species. Finally, the pores transform into nanotubes when the current becomes almost constant as a result of a competition between electrochemical oxide formation and chemical dissolution. The obtained TiO_2 nanotubes have diameters of ~100 nm, and lengths of ~750 nm as shown in Figure 21a.

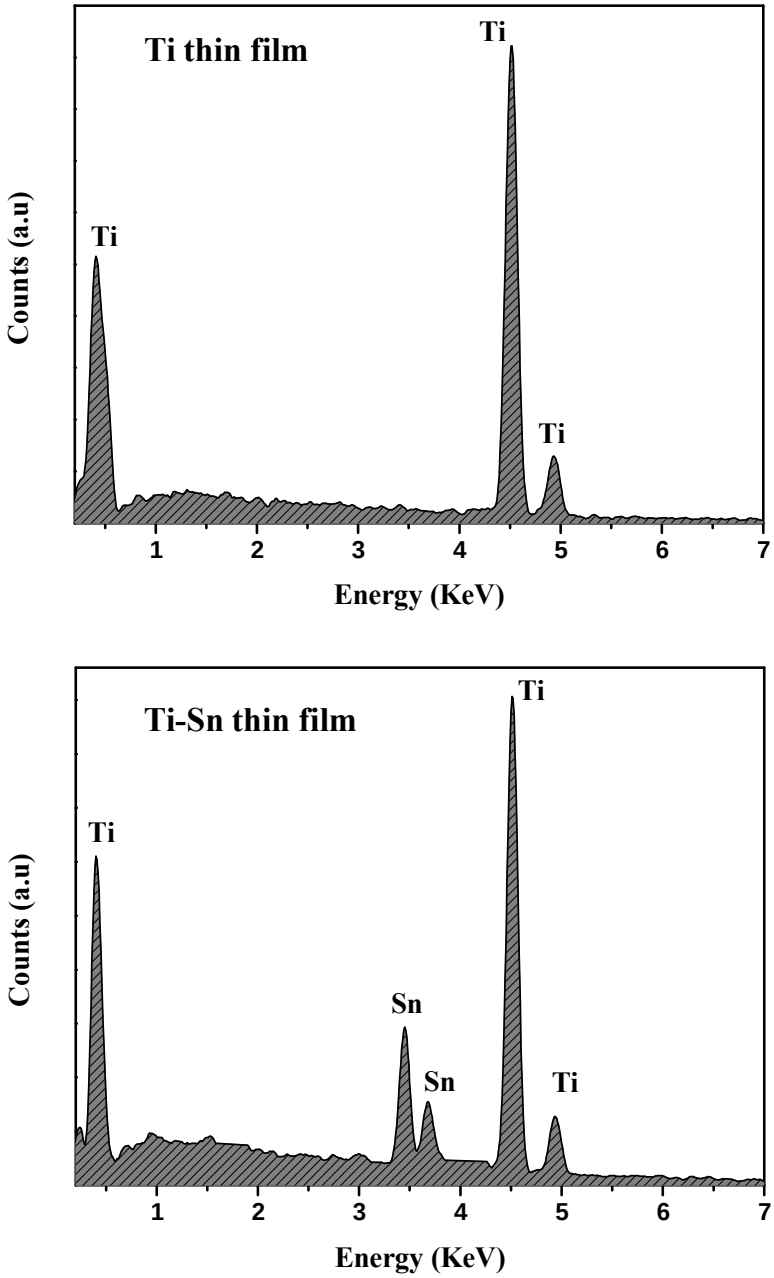

Figure 23 EDS spectra for the as-sputtered Ti and Ti-Sn thin films

As tin and titanium can be independently oxidized under similar electrochemical conditions, anodization of the co-sputtered Ti-Sn thin film (with the usual conditions for the production of TiO_2nts) led to Sn-doped TiO_2nts as shown in Figure 22c. It can also be noticed in Figure 20 that the recorded current-transient is sufficiently characteristic of nanotubes formation. The obtained Sn-doped TiO_2nts have lengths of ~1.20 µm and diameters of ~90 nm according to the SEM images presented in Figure 22c. As the Sn-doped TiO_2nts were not highly delimited according to SEM imaging, TEM imaging (Figure 25a-b) was also carried out. Although the scratched nanotubes had agglomerated, nanotubes could be distinguished with ~90 nm diameter, ~30 nm bottom wall thickness and ~15 nm side wall thickness. The selected area electron diffraction (SAED) pattern shown in Figure 25c evidenced that the as-formed Sn-doped TiO_2nts are amorphous.

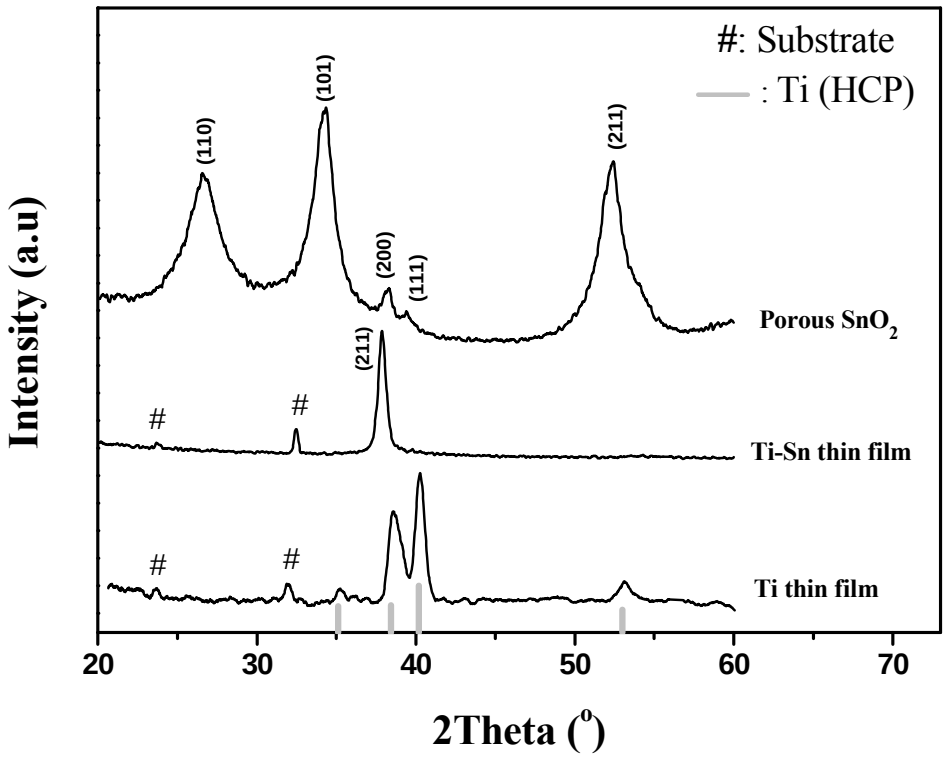

Figure 24 X-ray diffractograms of porous SnO_2 (JCPDS: 041-1445) annealed at 400 ºC, as-deposited Ti thin film (JCPDS: 44-1294), and as-deposited Ti-Sn thin film (JCPDS: 03-065-3605).

A cross-sectional SEM image of the co-sputtered Ti-Sn thin film (with a 500 nm Ti barrier layer) is shown in Figure 22b. It can be noticed that the thin film is homogeneous and columnar along the entire cross-section. It is important to note that the silicon substrates were not heated during the deposition. The EDS spectra shown in Figure 23 confirmed the incorporation of Sn into the Ti thin film. Although the sputtered pure titanium thin films studied in our lab[42, 120, 171] usually have a hexagonal titanium structure (JCPDS: 44-1294) from X-ray diffraction studies, the Ti-Sn thin film corresponds to the Sn_3Ti_5 intermetallic as shown in Figure 24. The peak at $2\theta = 38^{\circ}$ can be attributed to the (211) reflection of Sn_3Ti_5 (JCPDS: 03-065-3605). It is therefore obvious that there is a preferred orientation in the Ti-Sn thin film. The low intensity peaks marked '#' are emanating from the silicon substrate.

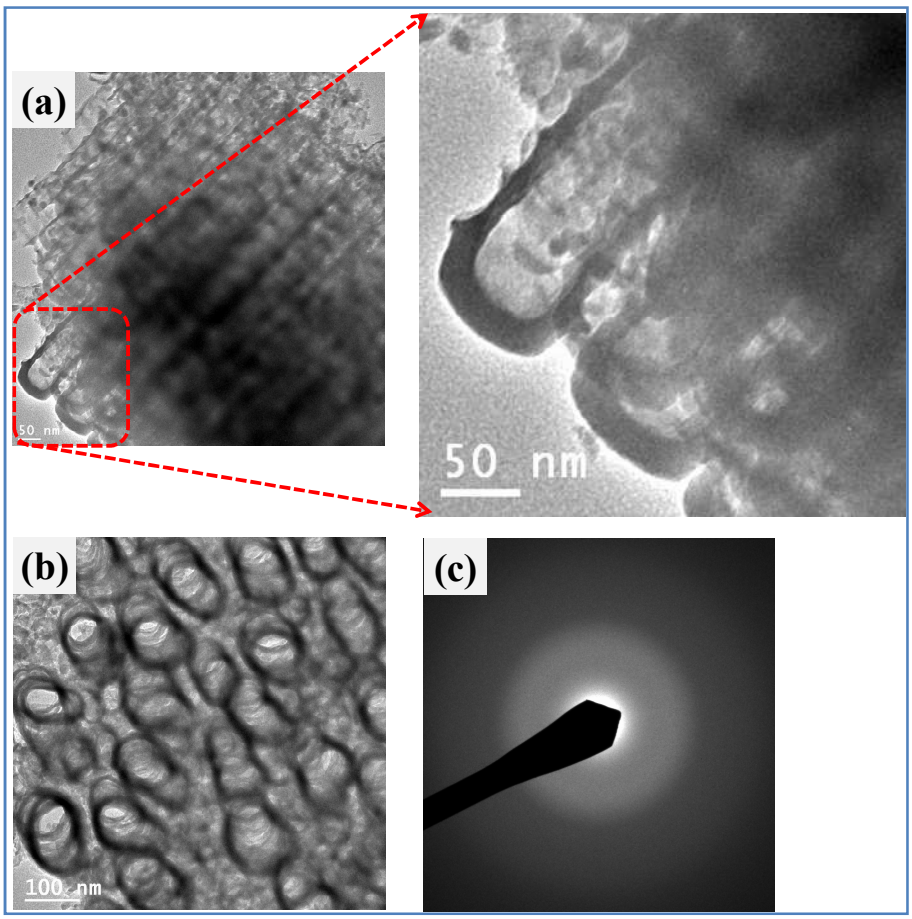

Figure 25 TEM micrographs (a-b) and SAED pattern (c) for the as-prepared Sn-doped TiO_2nts.

Usually, as-formed TiO_2nts are amorphous[42, 119]. Indeed, the as-prepared TiO_2nts and Sn-doped TiO_2nts were amorphous according to X-ray diffraction studies. However, after thermal treatments at 450 ºC, it can be noticed from Figure 26 that whilst the TiO_2nts crystallize in the anatase structure (JCPDS: 21-1272) with an infinitesimal rutile proportion (JCPDS: 21-1276), the Sn-doped TiO_2nts are transformed entirely into a rutile–type structure (JCPDS: 21-1276) without any traces of SnO_2 (cassiterite) nor SnO (romarchite). This transformation, from anatase to rutile, observed for the $Ti_{1-x}Sn_xO_2$–type nanotubes is consistent with the already established fact that Sn^{4+} substitution for Ti^{4+} in TiO_2 is generally accompanied by the structural transformation from anatase to rutile except for very low ($x \leq 0.05$) Sn contents[172, 173]. Table 3 presents a comparison of the calculated lattice parameters (Using Celref software) of TiO_2nts, porous SnO_2 and Sn-doped TiO_2nts. The obtained values are in good agreement respectively with the theoretical lattice parameters of anatase, cassiterite and rutile.

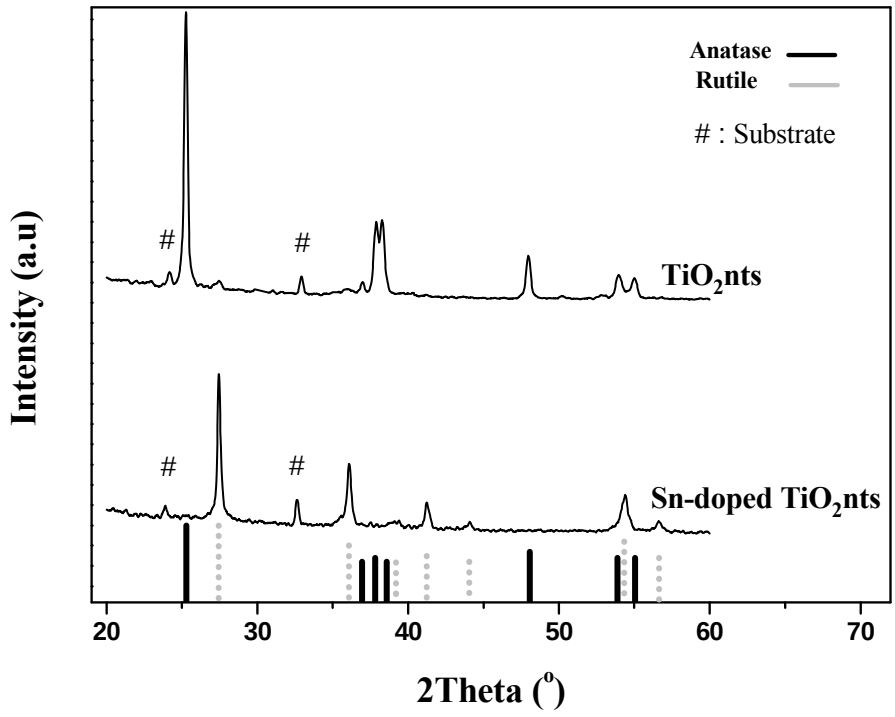

Figure 26 X-ray diffractograms of TiO_2nts and Sn-doped TiO_2nts recorded after thermal treatments at 450 ºC. The low intensity peaks marked '#' are emanating from the silicon substrate.

Table 3 Calculated Lattice parameters compared to theoretical values for Anatase, Rutile and Cassiterite.

	a /Å	c/Å	Volume/ Å^3		a /Å	c/Å	Volume/ Å^3
	Calculated				Theoretical		
TiO_2nts	3.78	9.50	135.74	Anatase	3.7852	9.5139	136.31
Sn-doped TiO_2nts	4.59	2.96	62.36	Rutile	4.5933	2.9592	62.43
Porous SnO_2	4.74	3.12	70.10	Cassiterite	4.7382	3.1871	71.55

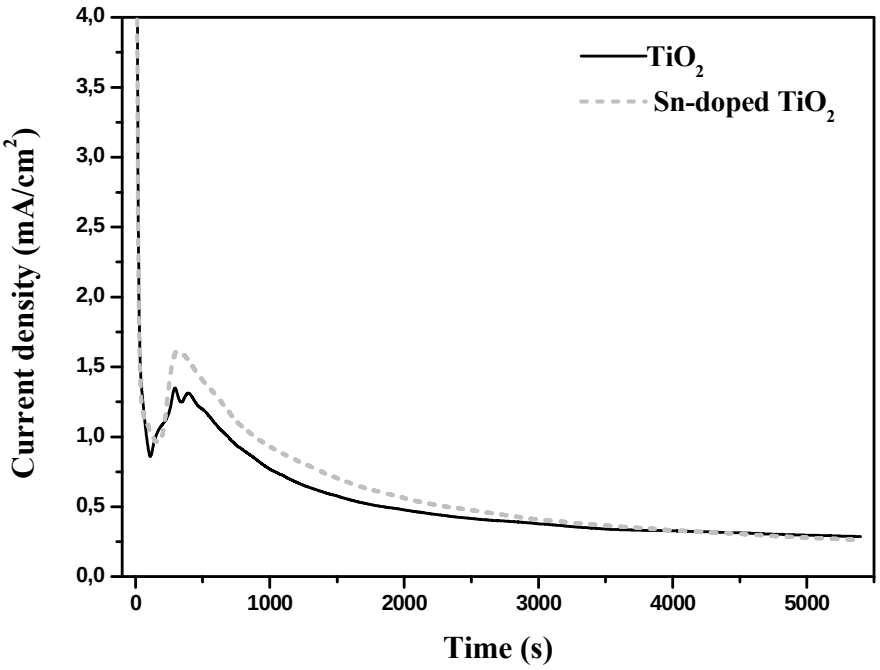

Figure 27 Chronoamperometric curves obtained during the 1.5 h anodization of Ti and Ti-Sn thin films at 40 V in an electrolyte consisting of 88.7 wt% glycerol, 1.3 wt% NH_4F and 10 wt% H_2O.

Furthermore, when the Ti and Ti-Sn thin films were anodized at 40V (for 1.5 h) in a viscous electrolyte consisting of 88.7 wt% glycerol, 1.3 wt% NH_4F and 10 wt% H_2O, the recorded current–transients (Figure 27) did not deviate from the usual profile characteristic of a nanotubular layer formation[42, 109, 117]. The only drastic variation is that the Sn incorporation led to higher peak current values from t = 400 to t = 3000 s, and this can be explained as a consequence of the formation of smaller diameter Sn-doped TiO_2 nanotubes. SEM images of the resulting TiO_2 and Sn-doped TiO_2 nanotubes are given in Figure 28. The undoped TiO_2 nanotubes have lengths of ~1.4 μm, diameters of ~160 nm, and sidewall thickness of ~20

nm; whilst the Sn-doped TiO_2 nanotubes have lengths of ~1.2 μm, diameters of ~120 nm, and sidewall thickness of ~15 nm.

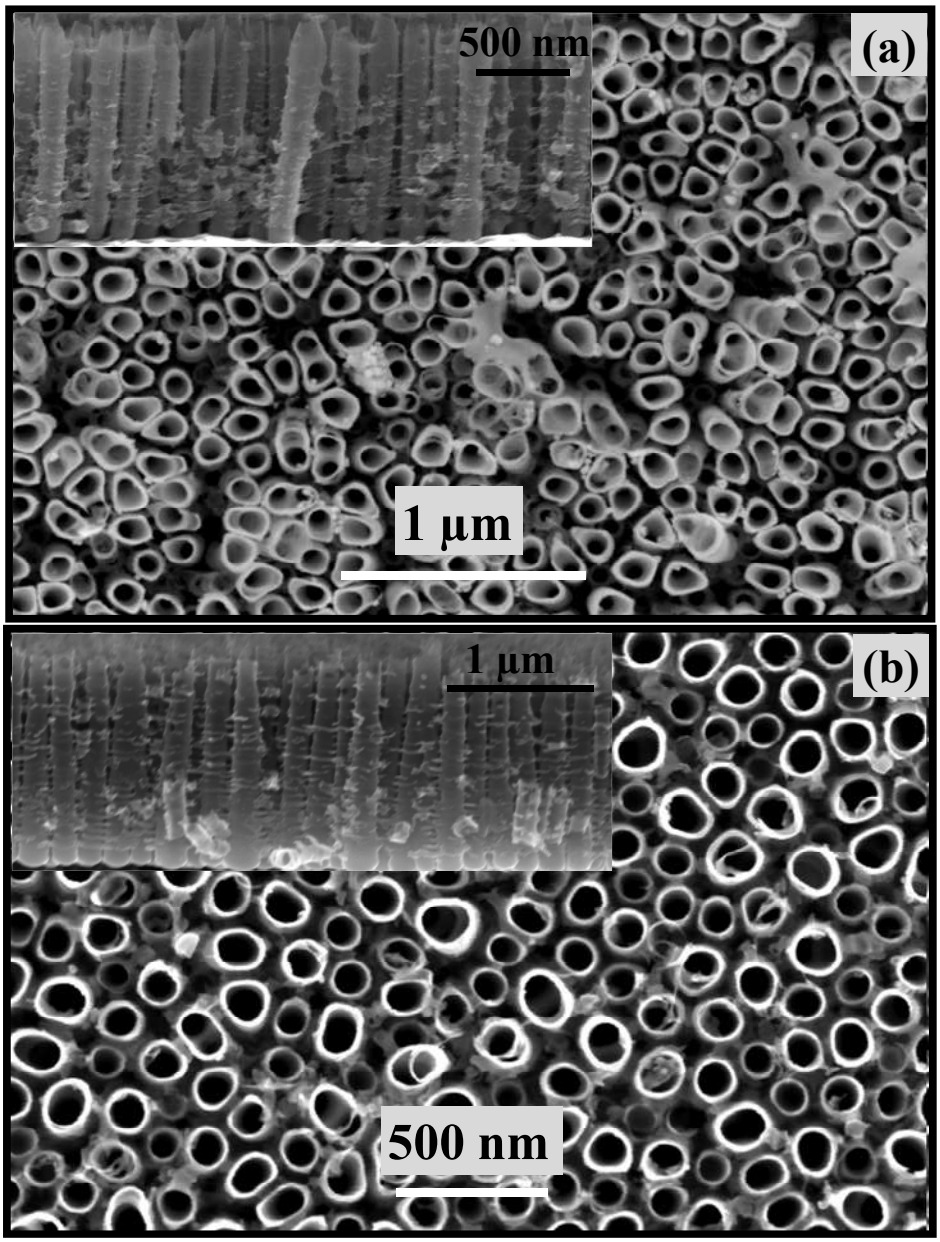

Figure 28 SEM images of (a) Sn-doped TiO_2 nanotubes (Inset: cross-section), and (b) undoped TiO_2 nanotubes (Inset: cross-section) prepared at 40 V (for 1.5 h) in the electrolyte consisting of 88.7 wt% glycerol, 1.3 wt% NH_4F and 10 wt% H_2O.

In order to confirm the oxidation state of the Sn dopants and ascertain the degree of the doping, X-ray photoelectron spectroscopy was carried out on the as-prepared TiO_2 nanotubes (analyzed for comparison) and Sn-doped TiO_2 nanotubes. The obtained high-resolution Ti2p,

O1s, C1s and Sn3d XPS core peaks spectra are presented in Figure 29 and Figure 30. The corresponding data and quantitative analysis are given in Table 4. For both samples, carbon contamination was detected (arising from traces of the solvent used for the anodization).

For the as-prepared TiO_2 nanotubes, the C1s spectrum presents one main component located at 285.0 eV associated with C-C or C-H bonds, and two other components at about 286.5 and 288.9 eV respectively attributed to C-O and O=C-O bonds. Quite similar attributions can be done for the Sn-doped TiO_2 nanotubes, except a very low intensity component located at a high binding energy (289.7 eV), which could correspond to a very low quantity of carbonate species. Due to spin-orbit coupling for both samples, each spectrum exhibits two main Ti*2p* components located at 459.0 eV (Ti$2p_{3/2}$) and 464.7 eV (Ti$2p_{1/2}$). These binding energies (B.E) are representative of Ti^{4+} in an oxygen environment, which is in agreement with previous XPS data for bulk and thin film TiO_2 [174-178].

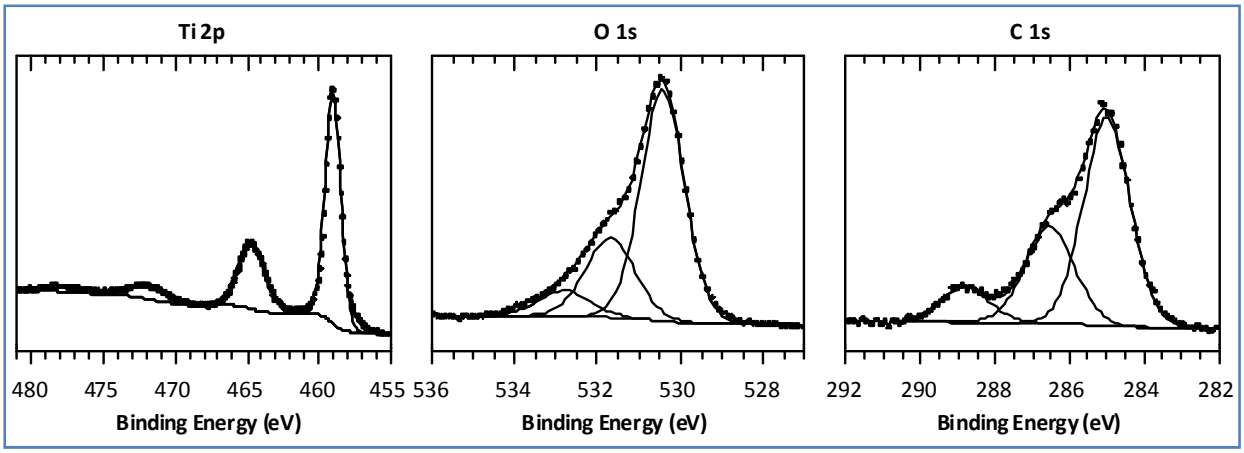

Figure 29 High-resolution Ti2p, O1s and C1s XPS spectra for the as-prepared TiO_2 nanotubes.

In addition, the spectra also contain distinct charge-transfer satellite peaks at about 13 eV above the $2p_{3/2}$ and $2p_{1/2}$ main peak positions. The origin of Ti*2p* satellite peaks is under debate[179-183]; one of the most likely explanations is the strong covalent hybridization between the metal d and the oxygen p orbitals[179]. The main peaks are essentially characterized by the

well screened final state configuration $2p^5 3d^1 L^{-1}$, where L denotes the ligand electron[180]. The satellite peaks are caused by the hole-particle pair "shake-up" excitation on the anions in the presence of the ligand-metal charge transfer screened core hole. They mostly correspond to the $2p^5 d^0$ and $2p^5 d^1 L^{-1} L'L''^{-1}$ final state configurations [181].

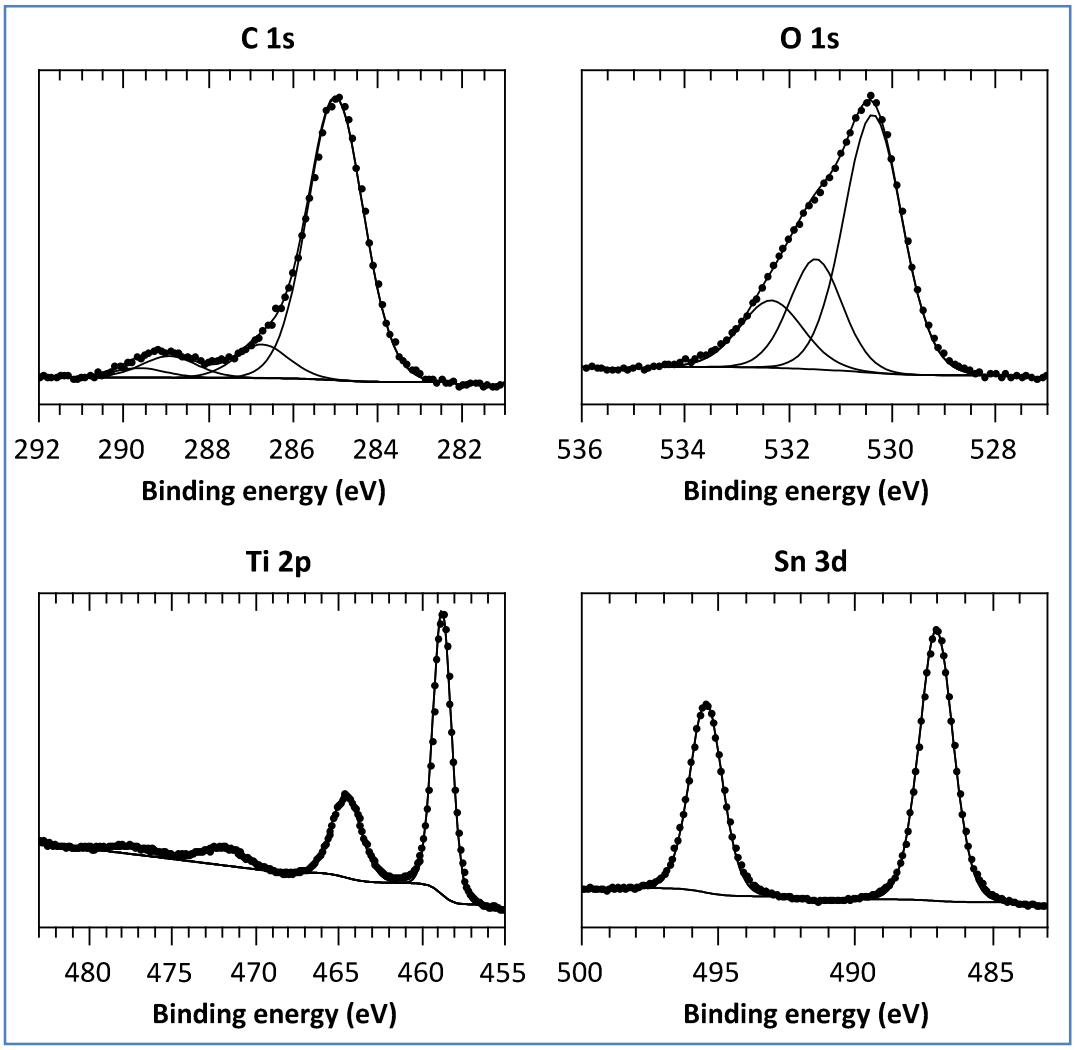

Figure 30 High-resolution Ti2p, O1s, C1s and Sn3d XPS spectra for the as-prepared Sn-doped TiO_2 nanotubes.

For both samples, the O1s core peaks also present three components. The first one located at 530.4(5) eV is assigned to oxygen atoms of the TiO_2 oxide lattice. Hence, it can be noted from Table 4 that for the as-prepared undoped TiO_2 nanotubes, the O/Ti atomic ratio is close to 2 (37.6/19.3); and for the as-prepared Sn-doped TiO_2 nanotubes, the O/(Ti+Sn) atomic ratio is also close to 2 (39.7/22.3). The two other O1s core peaks (531.7 and 532.8 eV)

are related to O=C-O and C-O bonds, in agreement with the C1s core peaks. Obviously, the Sn doping does not seem to affect the ionic network of titanium dioxide nanotubes, as no substantial modification of binding energy was observed. Owing to spin–orbit coupling effects, two peaks corresponding to $Sn3d_{5/2}$ (487.1 eV) and $Sn3d_{3/2}$ (495.5 eV) are observed, which are ascribable to the Sn^{4+} incorporated into the TiO_2 lattice[184, 185]. The quantity of the Sn dopants (x) in the $Ti_{1-x}Sn_xO_2$–type nanotubes was estimated to be ~0.5, since a Ti/Sn ratio of ~1 was obtained (Table 4).

Table 4 Binding energies, full widths at half maximum (FWHM) and atomic percentages of Ti2p, O1s, C1s and Sn3d XPS core peaks for the as-prepared TiO_2 and Sn-doped TiO_2 nanotubes.

Core Peaks	TiO_2			Sn-doped TiO_2		
	B.E. (eV)	FWHM	at%	B.E. (eV)	FWHM	at%
C 1s	285,0	1,4	18,3	285,0	1,5	21,8
	286,5	1,5	6,3	286,6	1,5	3,7
	288,8	1,5	2,8	288,9	1,5	2,8
				289,8	1,5	0,8
			27,4			***29,1***
Ti 2p	459,0	1,3	10,9	458,8	1,3	6,6
	464,7	2,2	5,8	464,5	2,1	3,1
	471,9	3,2	1,8	472,0	3,2	1,0
	477,6	3,4	0,8	477,5	3,0	0,4
			19,3			***11,1***
O 1s	530,4	1,2	37,6	530,5	1,2	39,7
	531,7	1,4	11,4	531,6	1,3	7,0
	532,8	1,4	4,5	532,7	1,4	4,4
			53,3			***49,1***
Sn3d				487,1	1,4	6,7
				495,5	1,4	4,5
						11,2

Figure 31a-c presents the ^{119}Sn Mössbauer spectra of the Ti-Sn thin film, and the Sn-doped TiO_2nts before and after annealing at 450 °C for 3 hours. All these spectra were obtained under the same conditions. A summary of the obtained hyperfine parameters is given in Table 5. The parameters (δ = 1.688(8) mm/s; Δ = 0.47(2) mm/s) obtained for the signal of

the Ti-Sn thin film (Figure 31a) can be attributed to Sn^0, emphasizing that the sputtering process led to pure metallic products. Moreover, the weak line width (2Γ) of the Sn^0 signal is consistent with the XRD results that the Ti-Sn thin film does not consist of a mixture of phases.

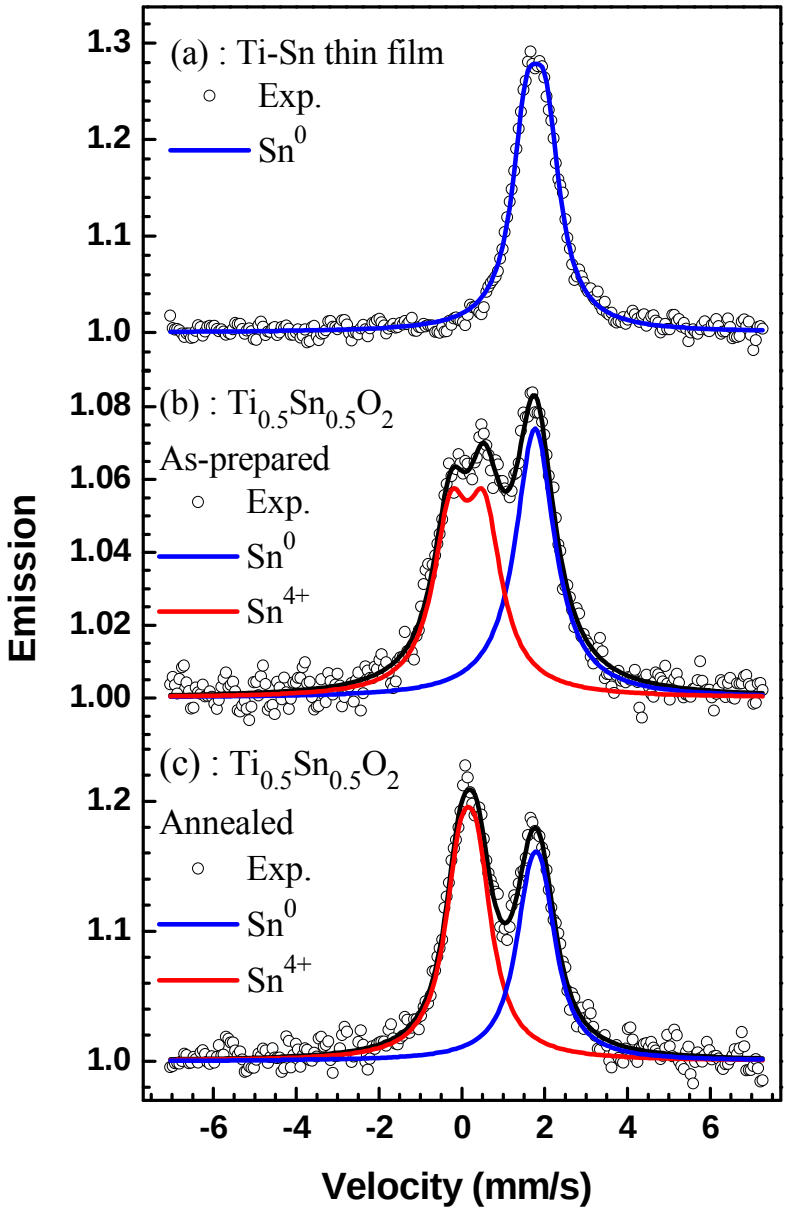

Figure 31 Room temperature ^{119}Sn Mössbauer spectra recorded for as-deposited Ti-Sn thin film (a), and Sn-doped TiO_2nts (b: amorphous, c: annealed at 450 °C).

Although the starting Ti-Sn thin film corresponds (according to X-Ray diffraction) to Sn_3Ti_5 intermetallic as mentioned earlier, the ^{119}Sn Mössbauer spectroscopy studies could not

confirm the exact nature of this thin film as the hyperfine parameters did not exactly match those of Ti-Sn intermetallics previously reported[186, 187]. However, Ti_2Sn (δ = 1.76 mm/s), Ti_3Sn (δ = 1.80 mm/s) and Ti_5Sn_3 (δ = 1.81 mm/s) have isomer shifts close to what was obtained for our Ti-Sn thin film although the quadrupole splitting of the former intermetallics were more intense[186, 187]. It is important to note that the intermetallics mentioned in literature, apart from having particulate morphologies, were produced by arc melting and annealed at very high temperatures. In addition, XRD evidenced the presence of impurity phases[186, 187]. Thus the mismatch in the hyperfine parameters in comparison to the present results can be explained by the differences in synthesis routes, thermal treatments, morphologies, and purity of the crystalline phases.

Table 5 Room temperature ^{119}Sn Mössbauer hyperfine parameters obtained from Ti-Sn thin film, as-prepared and annealed Sn-doped TiO_2nts.

Sample	Attribution	δ (mm/s)	Δ (mm/s)	2Γ (mm/s)	C (%)	χ^2
Ti-Sn thin film	Sn^0	1.688(8)	0.47(2)	0.84(2)	100	0.42
As-prepared Sn-doped TiO_2nt	Sn^0	1.66(3)	0.36(6)	0.98(7)	46(8)	0.46
	Sn^{4+}	0.05(2)	0.81(2)	1.02(5)	54(6)	
Annealed Sn-doped TiO_2nt	Sn^0	1.69(2)	0.32(8)	0.91(6)	43(1)	0.51
	Sn^{4+}	0.06(2)	0.42(5)	0.91(6)	57(1)	

δ: isomer shift; Δ: quadrupole splitting; 2Γ: full line width at half-maximum; *C*: contribution to total emission (not corrected due to unknown Lamb-Mössbauer factors); χ^2: goodness of the fitting.

The spectrum of the as-prepared Sn-doped TiO_2nts (Figure 31b) consists of two unresolved doublets. The doublet at δ = 1.66(3) mm/s is attributed to the Sn^0 from the remaining Ti-Sn layer that has not been anodized. Although the presence of this un-anodized Ti-Sn layer was not revealed by XRD, it can be due to the fact that, most probably, the amount of the remaining Ti-Sn layer is below the detection limit of XRD. This is consistent with the undoped TiO_2 nanotubes; the presence of un-anodized Ti layer was also not revealed by XRD. The other doublet at δ = 0.06(2) mm/s can be ascribed to Sn(IV). The isomer shift of δ = 0.06(2) is very close to what is typically obtained for Sn(IV) bonded to oxygen in

octahedral environnments[188-190]. These Mössbauer parameters are also in good agreement with those previously[99] obtained for Sn-doped anatase TiO_2 particles. The structural and chemical characterization performed by XRD, XPS, and Mössbauer spectroscopy clearly confirm the octahedral substitution of Sn^{4+} for Ti^{4+} in the self-organized TiO_2 nanotubes.

When the Sn-doped TiO_2nts sample is annealed (Figure 31c), two modifications are observed: (i) the intensity of the emission signal increased, indicating that annealing induced an increase in crystallite size; and (ii) the quadrupole splitting of the Sn^{4+} doublet decreased, indicating a better ordered lattice for the annealed sample. The relative amounts of Sn^0 and Sn^{4+} were not significantly affected by the heat treatment. Moreover, the Sn^0 doublet has the same parameters as those obtained for the as-prepared Sn-doped TiO_2nts sample and the as-sputtered Ti-Sn thin film, indicating that the structure of the Ti-Sn thin film is conserved for all samples.

4.1.2. Electronic Properties

From the Mott-Schottky equation given in Eq.(21), the flat band potential (E_{fb}) and the charge carrier concentration (N_D) of a specific semiconductor can be determined by plotting C^{-2} versus E (potential).

$$\frac{1}{C^2} = \left(\frac{2}{q\varepsilon\varepsilon_0 N_D} \right) \left(E - E_{fb} - \frac{kT}{q} \right) \qquad (21)$$

Where C is the capacitance of the space charge layer; q the elementary charge (1.6×10^{-19} C); ε_0 the vacuum permittivity (8.85×10^{-14} Fcm^{-1}); ε the dielectric constant of the studied semiconductor; k is Boltzmann's constant; and T is the absolute temperature. Figure 32 shows the Mott-Schottky plots obtained for the undoped and the Sn-doped TiO_2nts. The positive slope of each plot is in agreement with n-type semi-conductivity. For both undoped and Sn-doped TiO_2nts, approximately the same values of E_{fb} (-0.85 V vs Ag/AgCl) and N_D (6.5×10^{19}

cm^{-3}) were estimated, which is consistent with the theoretical consideration that Sn^{4+} (isovalent) substitution for Ti^{4+} in TiO_2 should not modify the semi-conducting behavior.

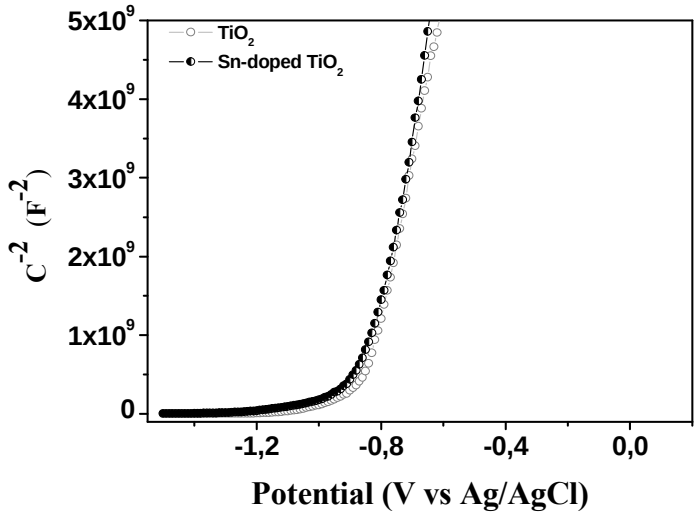

Figure 32 Mott-schottky plots obtained for the undoped and the Sn-doped TiO_2nts in a 0.1 M Na_2SO_4 solution at 30 Hz.

The conductivity (σ) of either the undoped or the Sn-doped TiO_2nts can be estimated using the charge carrier concentration (N_i), the electron mobility (μ_i) and the elementary charge (q_i) according to Eq.(22)[100, 191]; but the resulting values should be indistinguishable as the same values of charge carrier concentration (N_i) were obtained from the Mott-Schottky analysis.

$$\sigma_i = q_i \mu_i N_i \qquad (22)$$

However, it has previously[172] been demonstrated that Sn^{4+} substitution for Ti^{4+} in TiO_2 leads to increase of the bond lengths of the inner coordination shells due to the larger ionic radius of Sn^{4+} [$r(Sn^{4+})$=0.83 Å] compared to Ti^{4+} [$r(Ti^{4+})$=0.75 Å]. Fundamentally, increased bond lengths are indicative of weakened bonds and thus migration of cations (Li^+) is expected to be enhanced in the modified lattice. In view of this, we carried out potentiostatic experiments for which the current-transient profiles before the onset of a limiting current can be described by the Cottrell equation[82, 192]:

$$j = nFD_o^{1/2} C_o \pi^{-1/2} t^{-1/2} \quad (23)$$

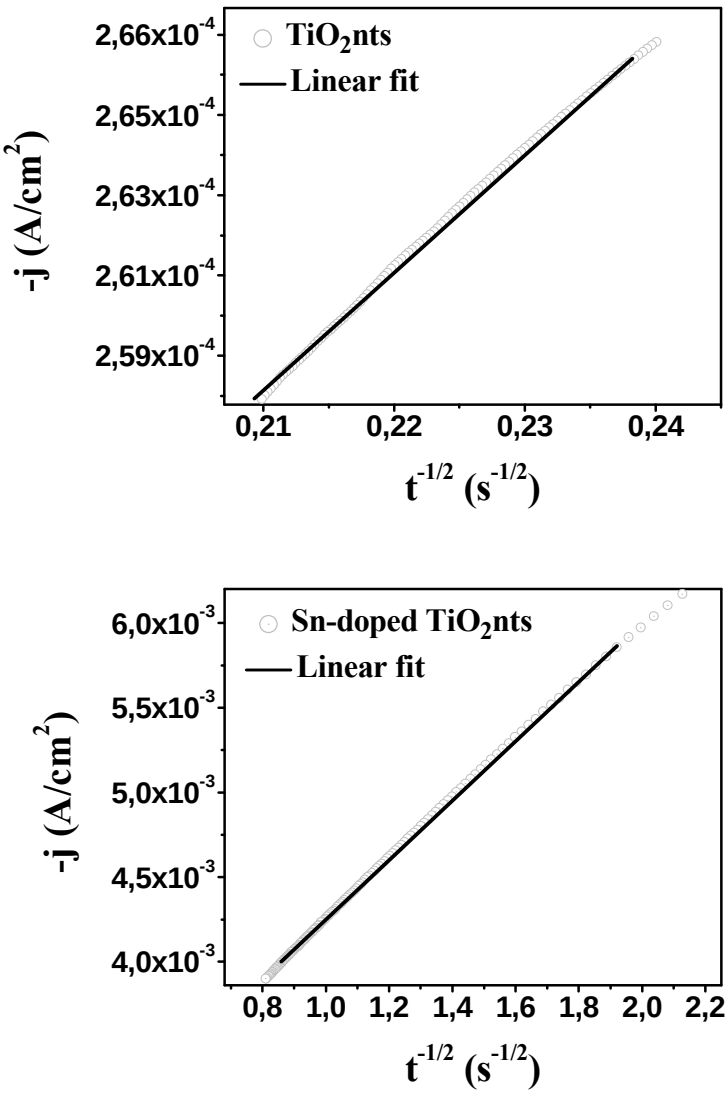

Figure 33 Cottrell plots for the determination of Li^+ diffusion coefficients in TiO_2nts and Sn-doped TiO_2nts.

The potentiostatic experiments consisted of applying a potential step (from 3.0 to 1.4 V vs Li^+/Li) to cells of $Li/LiPF_6$ (EC:DEC)/(TiO_2nts or Sn-doped TiO_2nts) during 30 s. Assuming the composition of the initial subsurface layer to be $Li_{0.5}TiO_2$ for both TiO_2nts and Sn-doped TiO_2nts, the concentration of Li^+ (C_o) was calculated to be 25×10^{-3} molcm^{-3} using 4 gcm^{-3} density of TiO_2. Hence, the diffusion coefficients (D_o) were estimated from the slopes of the fits to the Cottrell plots (Figure 33) to be 1.6×10^{-13} cm^{2}s^{-1} and 6.7×10^{-12} cm^{2}s^{-1} for

TiO_2nts and Sn-doped TiO_2nts respectively. These values of diffusion coefficients agree with previous reports[82, 192] in literature and indicate that Li^+ insertion into Sn-doped TiO_2nts is about 40 times faster than into undoped TiO_2nts. This is consistent with the assertion that increased bond lengths lead to more easy lithium ion diffusion in the structure.

4.1.3. Electrochemical Behaviour

The electrochemical behaviour versus lithium of the Sn-doped TiO_2nts was evaluated by galvanostatic cycling experiments and compared to that of undoped TiO_2nts as shown in Figure 34, with a summary also given in Table 6. In spite of the fact that both nanotubes (doped and undoped) were prepared under the same conditions (40 V in a viscous electrolyte consisting of 88.7 wt% glycerol, 1.3 wt% NH_4F and 10 wt% H_2O), the Sn-doped TiO_2nts delivered much higher capacity values.

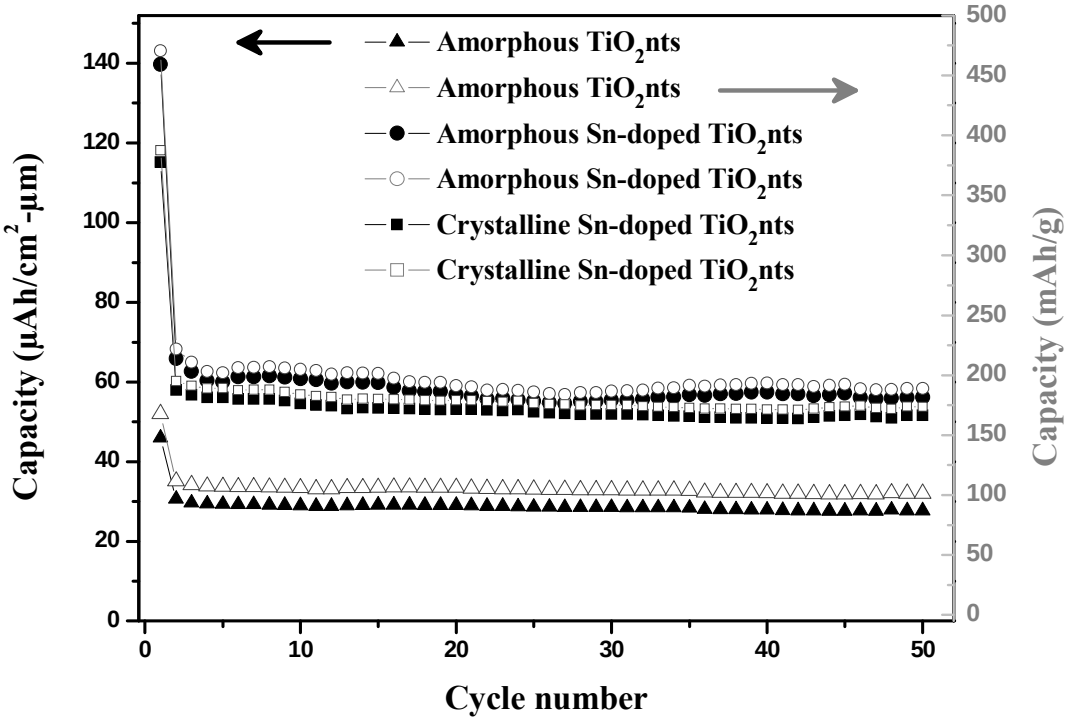

Figure 34 Galvanostatic cycle life performance at 70 µA cm^{-2} for undoped and Sn-doped TiO_2nts in the $1.0 \leq U/V \leq 2.6$ voltage range. The capacity values are given in µAh $cm^{-2}µm^{-1}$ (closed symbols) and in $mAhg^{-1}$ (open symbols) for amorphous TiO_2nts and Sn-doped TiO_2nts (amorphous and crystalline).

It has already[56, 193, 194] been established that the reactivity of rutile TiO_2 is sensitive to lithium diffusivity as a result of its peculiar crystal structure, hence the outstanding performance of the Sn-doped TiO_2nts is proposed to be related to the rutile–type structure and the enhanced lithium diffusivity imparted with the Sn doping; it was shown above with Cottrell plots (Figure 33) that Li^+ insertion into Sn-doped TiO_2nts is about 40 times faster than into undoped TiO_2nts. Also, cycling efficiencies were estimated to be 76%, 85% and 89% (Table 6) for the amorphous TiO_2nts, amorphous Sn-doped TiO_2nts and crystalline Sn-doped TiO_2nts respectively. Cycling efficiency (E) is a measure of capacity retention, and it can be expressed as the ratio of final reversible capacity (Q_f) to initial reversible capacity (Q_i)[42, 43]. Generally, amorphous TiO_2 electrodes exhibit lower cycling efficiencies than the crystalline counterparts, since the latter precludes lithium storage into defect sites and side reactions with substantial solvent traces[42]. Also, it can be asserted that so far as TiO_2 electrodes are concerned, cycling efficiencies are somewhat sensitive to current densities (C–rate values)[42].

$$TiO_2 + xLi^+ + xe^- \leftrightarrow Li_xTiO_2 \text{ for } 0 \leq x \leq 1 \qquad (24)$$

Table 6 Discharge capacities and cycling efficiencies (capacity retention) with 70 μA/cm^2 current density

Electrode	Condition	1st reversible capacity (μAh/cm^2-μm)	Irreversible capacity (μAh/cm^2-μm)	50th reversible capacity (μAh/cm^2-μm)	Cycling efficiency (%)
TiO_2nts	1–2.6V	28.6	17.0	21.9	76
Sn-doped TiO_2nts	1–2.6V	65.9	73.9	56.1	85
Sn-doped TiO_2nts[c]	1–2.6V	57.9	57.2	51.6	89

[c]Crystalline

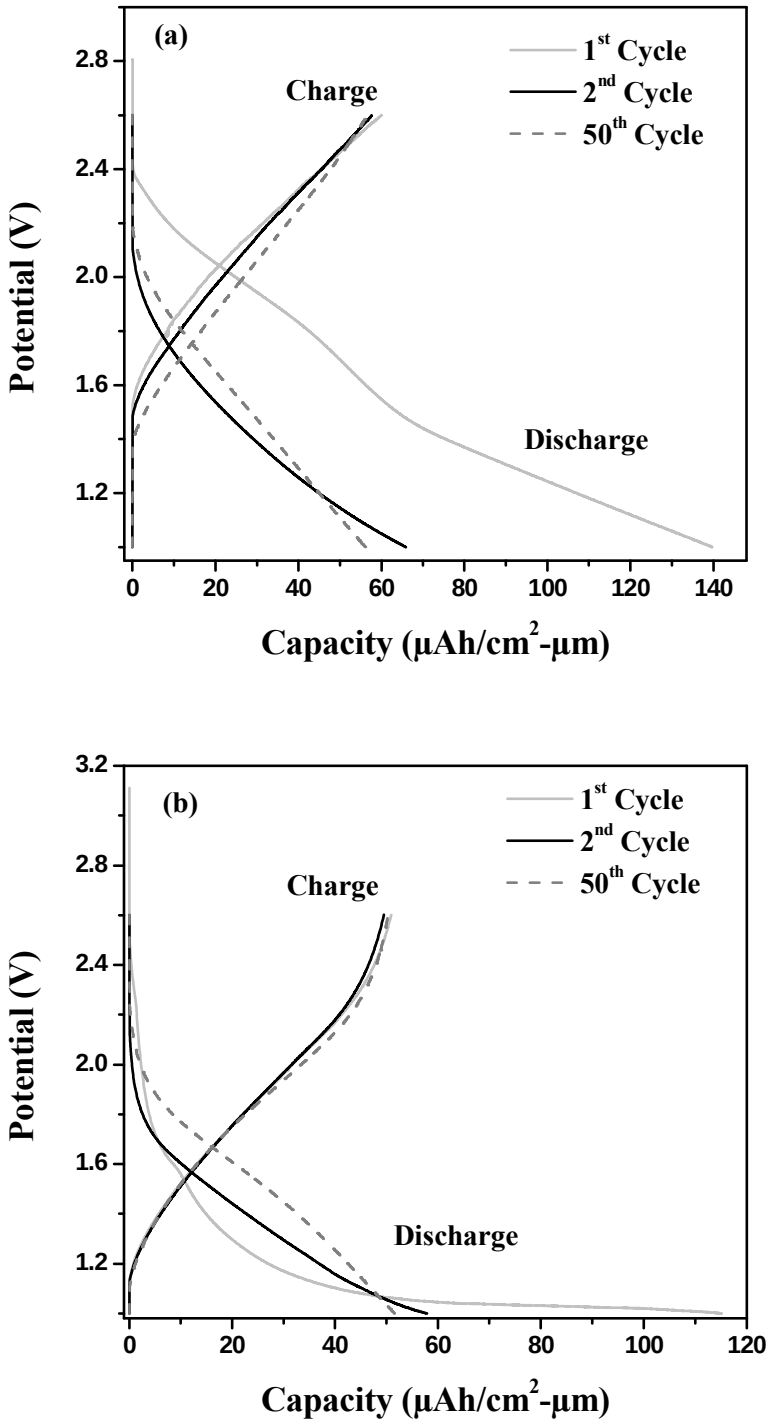

Figure 35 Galvanostatic curves obtained for the Sn-doped TiO_2nts (a: amorphous, b: crystalline) cycled in the $1.0 \leq U/V \leq 2.6$ voltage range.

The reaction for the reversible insertion of lithium into TiO_2 is as given in Eq.(24). It has been reported that ~1 Li^+ can be inserted into un-annealed (amorphous) TiO_2 due to lithium storage into defect sites[43]. For crystalline samples, although a maximum of 0.5 Li^+ can be

inserted into anatase, rutile can host up to 1 Li^+ (depending on the cut-off potential) of which almost 0.5 Li^+ are irreversibly trapped in the structure during the first discharge[43, 56]. Due to the degree of the Sn-doping, the Sn-doped TiO_2nts undergo full electrochemical reaction like a rutile-type TiO_2. That is the reason for the very high first discharge capacities (139.7 $\mu Ahcm^{-2}\mu m^{-1}$ for amorphous, and 115.1 $\mu Ahcm^{-2}\mu m^{-1}$ for crystalline) observed for the Sn-doped TiO_2nts. It has already been established that despite a very thin or inexistent solid electrolyte interphase (SEI) layer on TiO_2 electrodes, adsorbed solvents on surfaces of amorphous samples or crystallized water in the case of annealed samples contribute to the irreversibility in the first discharge[43]. The pronounced irreversible capacities observed for the Sn-doped TiO_2nts (73.9 $\mu Ahcm^{-2}\mu m^{-1}$ for amorphous, and 57.2 $\mu Ahcm^{-2}\mu m^{-1}$ for crystalline) as compared to the undoped TiO_2nts (17.0 $\mu Ahcm^{-2}\mu m^{-1}$) are a consequence of the extra lithium-ions irreversibly trapped in the rutile-type structure. The corresponding capacity values in $mAhg^{-1}$ are also presented in Figure 34. The approximate mass (m) of the TiO_2 nanotubes was estimated to be ~80 µg using: $m = V \times \rho \times P$, where ***P****(The porosity)* was estimated to be ~60% according to geometrical considerations from SEM micrographs[100, 195, 196], ***V****(Volume of nanotubes)* ≈ 3.848×10^{-5} cm^3, and $\boldsymbol{\rho}$(Density of anatase TiO_2), = 4.21 g cm^{-3}. It can be noted that for the TiO_2 nanotubes in particular, the reversible specific capacity values are less than the theoretical value of 168 mAh/g but comparable to a previous report in literature[195]. This can be due to the theoretical estimation of the mass of the TiO_2 nanotubes. Hence, it can be emphasized that the capacity values given in $mAhg^{-1}$ for the undoped and the Sn-doped TiO_2 nanotubes are slightly underestimated.

The galvanostatic discharge/charge profiles of the Sn-doped TiO_2nts (both amorphous and crystalline) are given in Figure 35; the sloping voltage profiles agree well with the cyclic voltammograms shown in Figure 36a-b, and are consistent with previous reports in literature[197-199]. For the crystalline Sn-doped TiO_2nts, the small plateau at *ca.* 1.65 V in the

first discharge (Figure 35b) can be attributed to surface storage of lithium, the corresponding small cathodic peak was also evidenced at *ca.* 1.6 V *vs* Li^+/Li in the 1st cycle CV (Figure 36b). Although the long sloping plateau (in the first discharge) starting at ca. 1.2 V ends at the cut-off potential of 1 V, the CV studies in the $0.65 \leq U/V \leq 3$ voltage range showed that the plateau is actually centered at *ca.* 0.85 V, and its irreversibility in the subsequent cycles is as a consequence of the extensive lithium storage up to that potential and the concomitant irreversible structural transformations.

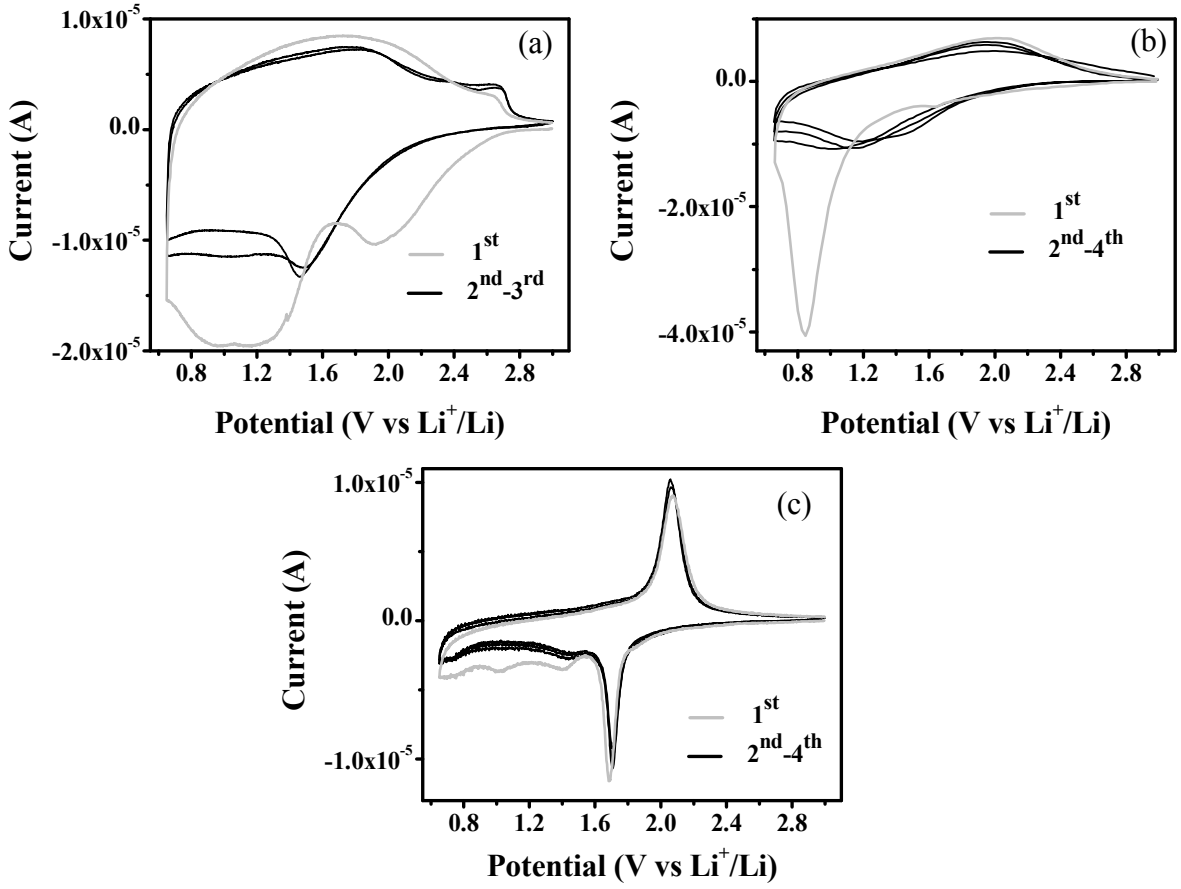

Figure 36 CV curves recorded at 0.1 mVs^{-1} in the $0.65 \leq U/V \leq 3$ voltage range for Sn-doped TiO_2nts (a: amorphous; b: crystalline), and crystalline TiO_2nts (c).

The CV curves obtained from crystalline TiO_2nts (Figure 36c) was presented to showcase the marked difference in the electrochemical characteristics brought about by the Sn-doping. It is worth noting that amorphous samples of TiO_2-based electrodes generally do not reveal

the characteristic peaks of reaction with lithium. The reduction peak at *ca.* 1.7 V *vs* Li^+/Li (Figure 36c) corresponds to lithium insertion (reversible Li^+ extraction peak at ca. 2.0 V *vs* Li^+/Li) into the anatase TiO_2 structure[43, 55] and the peaks seen at *ca.* 1.1V and 1.4 V *vs* Li^+/Li (Figure 36c) correspond to lithium insertion into the infinitesimal proportion of rutile TiO_2 as detected by XRD[56, 193].

In accounting for the improved behavior of the Sn-doped TiO_2 nanotubes, it is important to note that the response of only the Sn_3Ti_5 thin-film versus lithium is negligible and besides, the thin film is not active within the cycling voltage range of $1.0 \leq U/V \leq 2.6$ as it consists mainly of Sn as the active material[32, 45, 170]. Indeed, it is not the first time a beneficial effect of hetero-atoms is observed on the electrochemical behaviour of anode materials for Li-ion batteries[49, 200].

4.2. Fe Doping of TiO_2 Nanotubes

In this section, Fe doping of TiO_2 nanotubes is discussed. The Fe doping was achieved by the anodization of Ti-Fe thin films (obtained by co-sputtering Ti and Fe targets). The effect of Fe doping on the morphology and the electrochemical behaviour of TiO_2 nanotubes will be evaluated. To date, there are not many reports on the potentiostatic anodization of Fe in literature. Grimes and coworkers[201] first reported the formation of nanoporous iron oxide layers by potentiostatic anodization of Fe foils. They also succeeded to produce fairly-organized Ti-Fe-O nanotubes for water splitting applications[163]. Recently, anodic oxidation of Fe under optimized conditions led to well-ordered nanotubes of Fe_2O_3[162, 202].

4.2.1. Morphology, Structure and Composition

Figure 37a shows a cross-sectional SEM image of the as-deposited Ti-Fe thin film. The thin film is homogeneous and columnar along the entire cross-section. According to the XRD pattern shown in Figure 38, the as-deposited Ti-Fe thin film corresponds to a solid solution of Ti and Fe. The peak at $2\theta = \sim 39^{\circ}$ is perfectly assignable to the (1 1 0) reflection of body-centered cubic β-titanium (JCPDS: 1-089-4913). Thus the Ti–Fe thin film has a β-Ti–type structure but with preferred orientation. Usually, the sputtered titanium thin films studied in our lab[42, 120, 171] exhibit a hexagonal titanium structure (JCPDS: 44-1294) as presented in Figure 38. Hence, this transformation to β-Ti–type structure is due to the formation of a solid solution between Ti and Fe even though there was no substrate heating during the sputtering process. Moreover, it can be inferred that although the similarly co-sputtered Ti-Sn thin film discussed in section 4.1.1 corresponded to Sn_3Ti_5 intermetallic, the solid solubility observed with the as-deposited Ti-Fe thin film is not unusual with respect to the Hume-Rothery rules. SEM images of the Fe-doped TiO_2nts obtained by anodization of the Ti-Fe thin films are

presented in Figure 37(b-c). The nanotubes have lengths of ~750 nm, diameters of ~150 nm, and sidewall thickness of ~20 nm. EDS analysis (Figure 39) confirmed the pure metallic nature of the Ti-Fe thin film, and evidenced the presence of significant amount of oxygen in the as-prepared Fe-doped TiO_2nts.

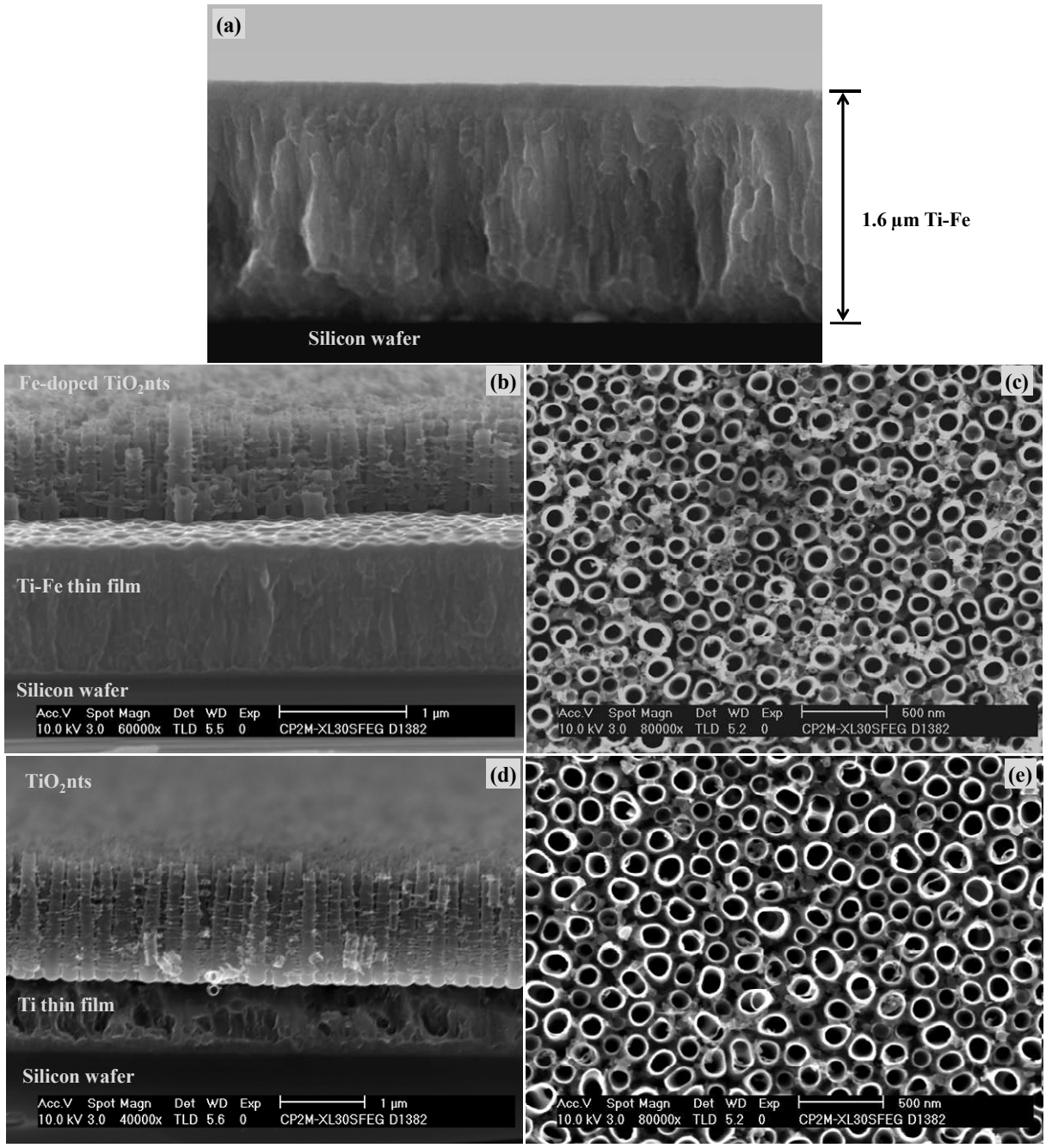

Figure 37 SEM images of (a) Ti-Fe thin film; (b-c) Fe-doped TiO_2 nanotubes, and (d-e) undoped TiO_2 nanotubes prepared in an electrolyte of 88.7 wt% glycerol, 1.3 wt% NH_4F and 10 wt% H_2O.

For comparison, undoped TiO_2nts were prepared by anodization of Ti thin films under the same conditions as used for the Fe-doped TiO_2nts. SEM images of the obtained TiO_2nts are shown in Figure 37(d-e). The TiO_2nts have lengths of ~1.4 μm, diameters of ~160 nm, and sidewall thickness of ~20 nm. By comparing the SEM images, it can be noticed that the marked difference brought about by the iron doping is in the cross-section of the nanotubes. Similar to the TiO_2nts, the as-prepared Fe-doped TiO_2nts were also amorphous and after annealing at 400 °C, anatase–type peaks could be identified (Figure 40) with a negligible proportion of rutile. Pronounced rutile–type peaks emerged in addition to the anatase after annealing at 450 ºC. The anatase to rutile transformation is expected to be promoted by the Fe dopants since TiO_2 nanotubes usually crystallize only in the anatase phase or have negligible rutile proportions at 450 °C [43, 100, 109]. The peaks marked '#' are emanating from the silicon substrate and the peaks marked '°' correspond to $FeTiO_3$ (JCPDS: 29-0733)–this phase formed due to the low solubility of iron in TiO_2 by this synthesis approach[163].

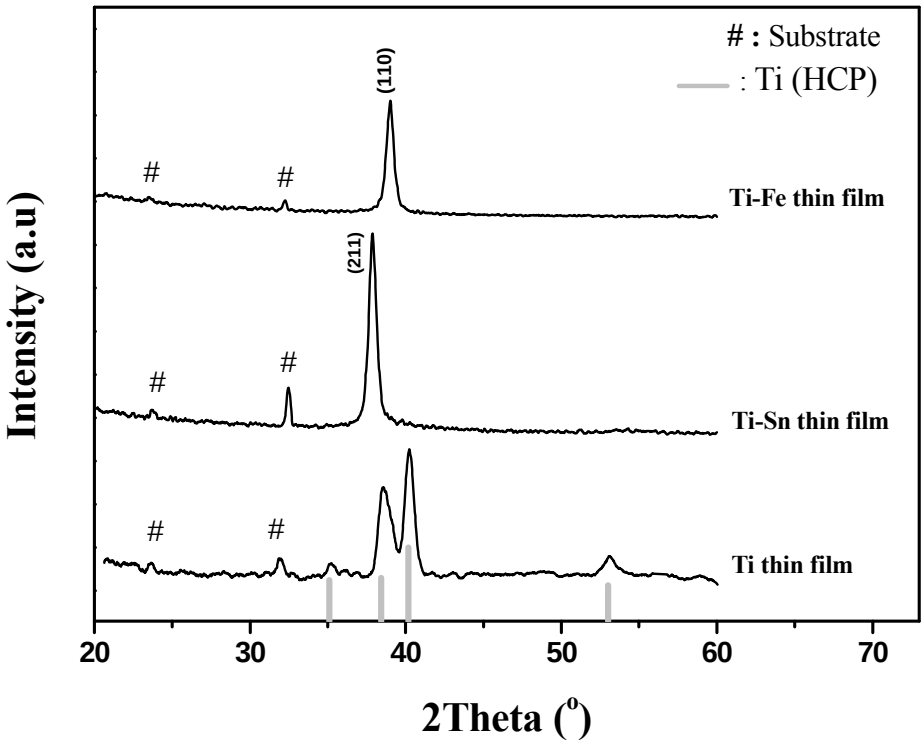

Figure 38 XRD pattern for the as-deposited Ti-Fe thin film compared with those of pure Ti and Ti-Sn thin films.

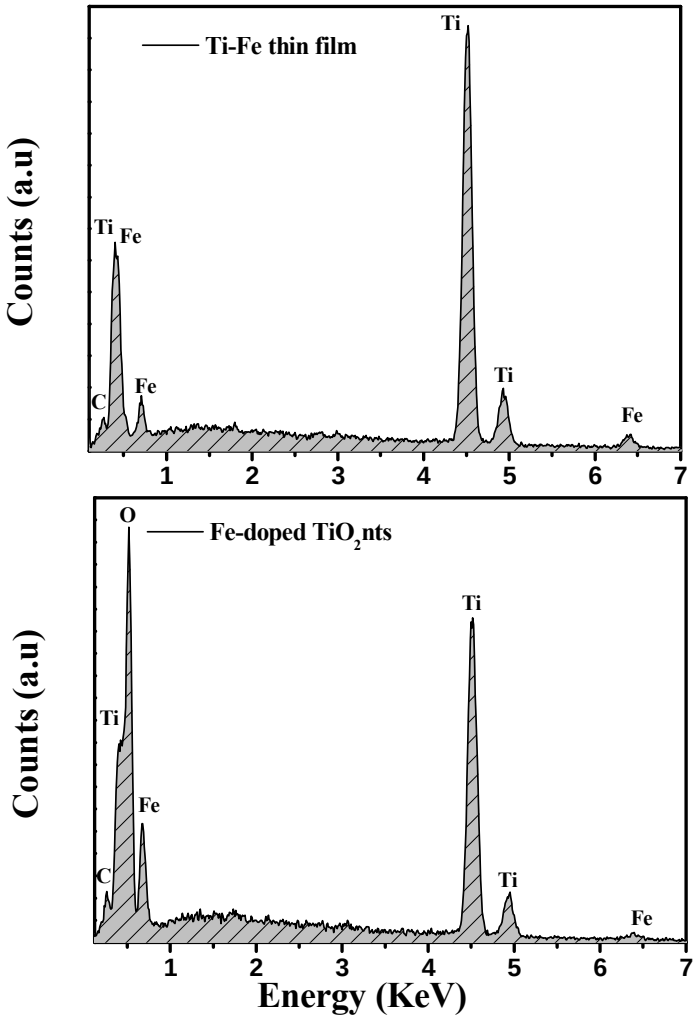

Figure 39 EDS spectra for the as-sputtered Ti-Fe thin film and the as-prepared Fe-doped TiO_2 nanotubes.

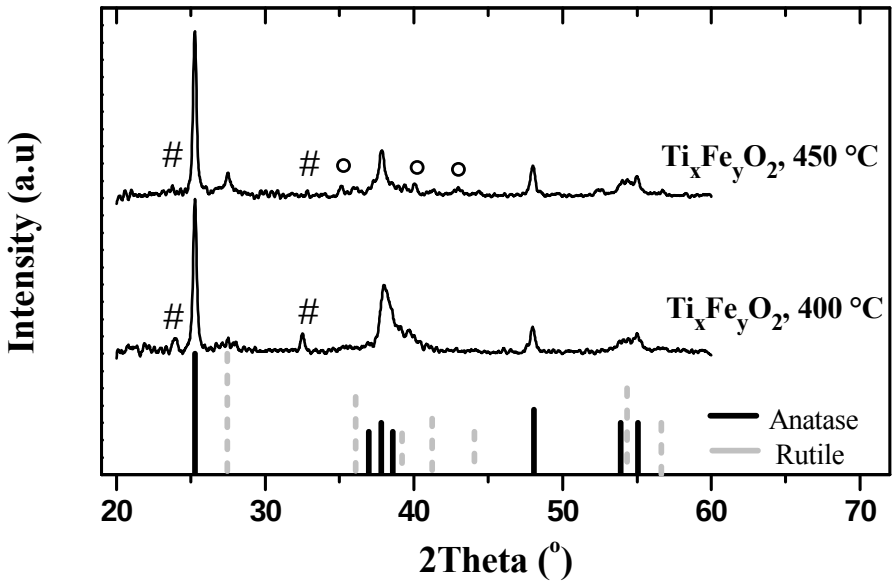

Figure 40. XRD pattern for Fe-doped TiO_2 nanotubes annealed at different temperatures.

In order to confirm the oxidation state of the iron dopants and ascertain the quality of the doping, XPS was carried out. High-resolution Ti2p, O1s, C1s and Fe2p XPS spectra of the Fe-doped TiO_2nts are given in Figure 41 and Figure 42. The Ti2p, O1s and C1s XPS core peaks of the as-prepared undoped TiO_2nts are also provided in Figure 41. The corresponding data and quantitative analysis are given in Table 7. For both samples, carbon contamination was detected (arising from traces of the solvent used for the anodization). The C1s spectra present one main component located at 285.0 eV associated with C-C or C-H bonds, and two weak components at about 286.5 and 288.9 eV respectively attributed to C-O and O=C-O bonds. Due to spin-orbit coupling for both samples, each spectrum exhibits two main Ti*2p* components located at 459.0 eV (Ti$2p_{3/2}$) and 464.7 eV (Ti$2p_{1/2}$), and the corresponding binding energies (B.E) are representative of Ti^{4+} in an oxygen environment as discussed in section 4.1.1.

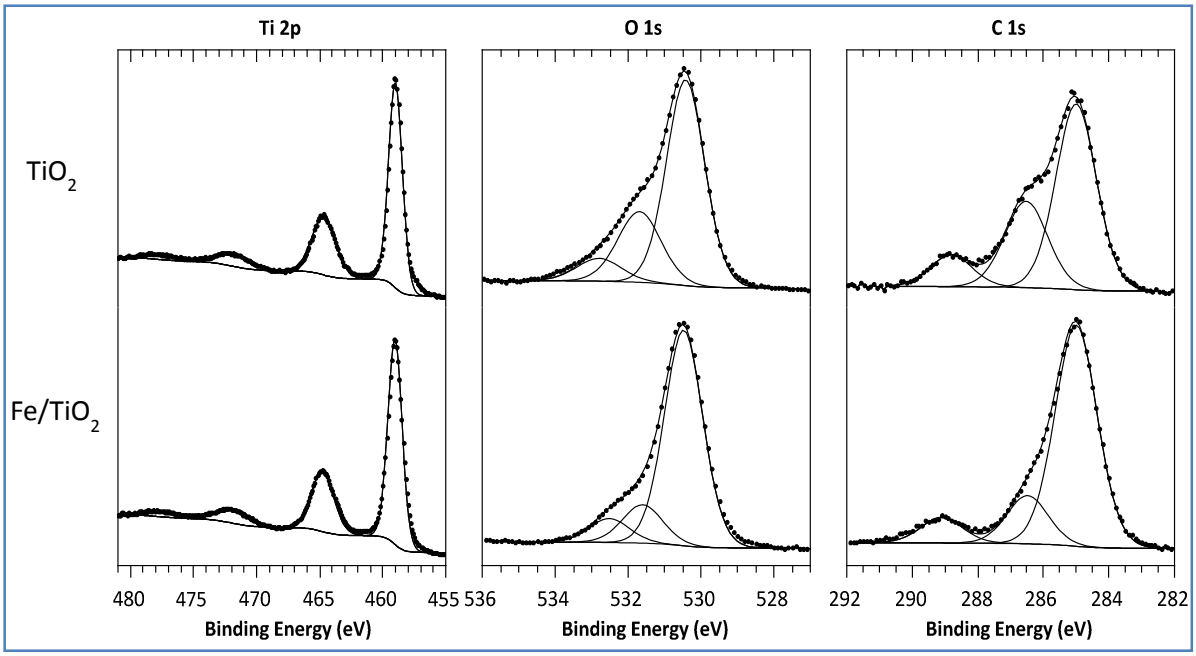

Figure 41. High-resolution Ti2p, O1s and C1s XPS spectra recorded for the as-prepared TiO_2 and Fe-doped TiO_2 nanotubes.

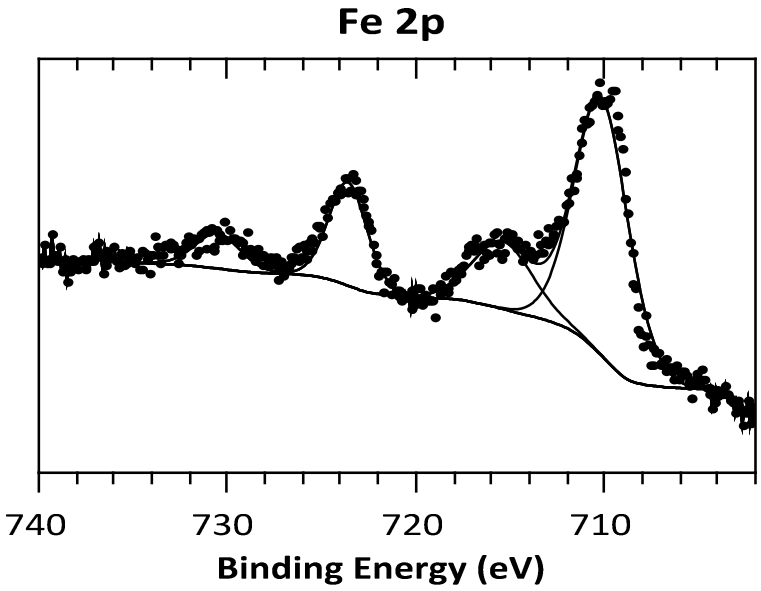

Figure 42. High-resolution Fe2p XPS spectrum recorded for the as-prepared Fe-doped TiO_2 nanotubes.

For both samples, the O1s core peaks present three components. The first (main) one, located at 530.4(5) eV, corresponds to the oxygen atoms of the TiO_2 oxide lattice. It can be noted that for the as-prepared TiO_2 and the Fe-doped TiO_2 nanotubes, the atomic ratio O/Ti is close to 2. The two other O1s core peaks (531.7 / 532.8 eV) are related to O=C-O and C-O

bonds, in agreement with C1s core peaks. The iron doping does not seem to affect the ionic network of the titanium dioxide nanotubes. No modifications of the binding energies were observed. The relative percentage of iron (Table 7) detected within the first 5 nm probed is about 1 at%. It can be noticed that the Ti/O ratio for TiO_2 nanotubes is equal to 0.51, slightly higher than for the iron doped sample (0.50). This is a direct evidence (in addition to the enhanced rutile phase at 450 °C) that a certain percentage of iron atoms have substituted for some titanium atoms leading to $Ti_xFe_yO_2$–type nanotubes[163, 203]. Besides, not all the Ti^{4+} content given in Table 7 can be attributed to the TiO_2 stoichiometry due to the presence of the $FeTiO_3$ phase.

Table 7 Binding energy (B.E), Full width at half Maximum (FWHM) and atomic percentage (at%) of Ti2p, O1s, C1s and Fe2p XPS core peaks for the as-prepared TiO_2 and Fe-doped TiO_2 nanotubes.

Core Peaks	TiO_2			Fe/TiO_2		
	B.E. (eV)	FWHM	%	B.E. (eV)	FWHM	%
C 1s	285,0	1,4	18,3	285,0	1,5	22,2
	286,5	1,5	6,3	286,5	1,5	4,7
	288,8	1,5	2,8	289,1	1,5	2,4
			27,4			***29,3***
Ti 2p	459,0	1,3	10,9	459,0	1,3	12,0
	464,7	2,2	5,8	464,8	2,1	6,0
	471,9	3,2	1,8	472,0	2,8	1,4
	477,6	3,4	0,8	477,8	2,2	0,6
			19,3			***20,0***
O 1s	530,4	1,2	37,6	530,5	1,2	39,7
	531,7	1,4	11,4	531,6	1,3	7,0
	532,8	1,4	4,5	532,6	1,4	4,4
			53,3			***49,1***
Fe 2p				710,2	3,4	0,9
				715,4	3,7	0,3
				723,6	2,4	0,3
				730,5	2,8	0,1
						1,6

The detailed analysis of the XPS Fe2p core peak was also achieved; in literature, reference compounds such as iron metal, Fe_3O_4 (1 Fe^{2+} and $2Fe^{3+}$) and Fe_2O_3 ($2Fe^{3+}$) for example were analysed [204, 205]. The main peaks of the two oxidation states, +3 and +2, are close, the differentiation being essentially made at the level of the difference of the binding energy between the main $2p_{3/2}$ component and the observed satellite peak. It is reported in literature[204, 205] that the satellite peak of Fe^{2+} is located at around 5.5 eV to the $2p_{3/2}$ component of the Fe2p core peak and around 8.5 eV for Fe^{3+}. Our results show that the difference between the binding energy of the maximum of the satellite peak with its associated $Fe2p_{3/2}$ component is equal to 5.2 eV. It thus seems that we are mainly in the presence of Fe^{2+} but a few percent of Fe^{3+} cannot be excluded due to the asymmetry of both peaks. Although there was a phase segregation of $FeTiO_3$ after annealing at 450 °C, a certain percentage of the iron atoms substituted for titanium atoms leading to $Ti_xFe_yO_2$–type nanotubes, since both Fe^{2+} and Fe^{3+} can substitute for Ti^{4+} in the TiO_2 structure[206-208].

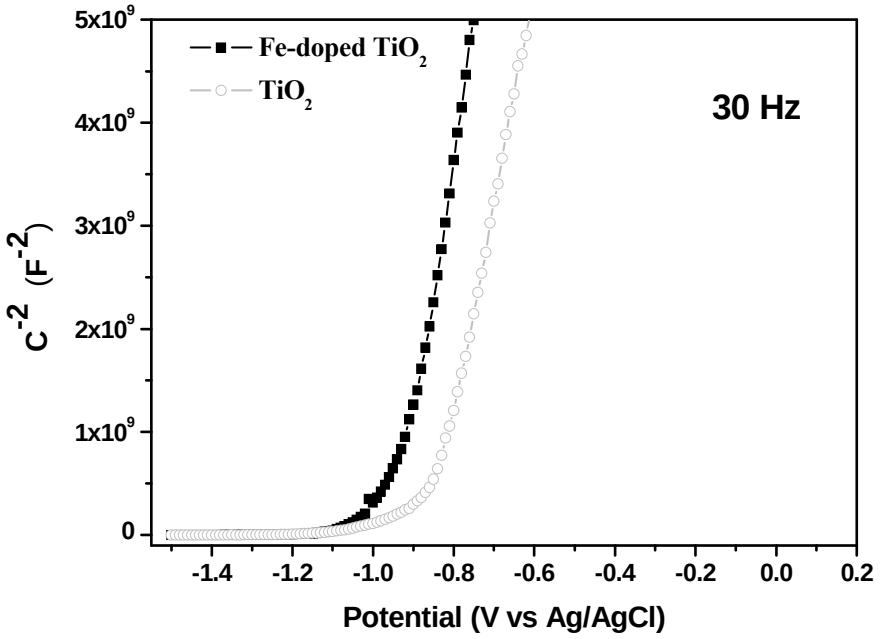

Figure 43 Mott-Schottky plots for the as-prepared TiO_2 and Fe-doped TiO_2nts.

4.2.2. Electronic Properties and Electrochemical Behaviour

Figure 43 shows the Mott-Schottky plots for the as-prepared TiO_2nts and Fe-doped TiO_2nts. The samples were prepared under the same experimental conditions since Mott-Schottky analysis is known to be sensitive to a material's synthesis conditions[209]. As expected, the capacitance increases with decreasing voltage until reaching a maximum in the accumulation region. The positive slope of each plot is in agreement with n-type semi-conductivity. Assuming a dielectric constant (ε) of 100[100, 210], the values of E_{fb} and N_D were determined to be -0.95 V vs Ag/AgCl and 5.0 $\times 10^{19}$ cm^{-3} respectively for the Fe-doped TiO_2nts, whilst for the un-doped TiO_2nts, E_{fb} of -0.85 V vs Ag/AgCl and N_D of 6.5 $\times 10^{19}$ cm^{-3} were obtained. Despite the fact that Mott-Schottky analysis is sensitive to a material's microstructure and synthesis conditions, the above values of flat-band potential (E_{fb}) and charge carrier concentration (N_D) are consistent with previous reports in literature[100, 203, 210-212]. In principle, the flat-band potential of a particular semiconductor depends on the pH of the employed electrolyte according to a Nernst-type relation (Eq.(25)):

$$E_{fb} = U_o - 0.06pH \qquad (25)$$

Where U_o (the flat-band potential at pH =0) is *ca.* -0.4 V vs Ag/AgCl for anatase TiO_2 and *ca.* -0.2 V vs Ag/AgCl for rutile TiO_2[82, 213]. From Eq.(25), the flat-band potential (with pH ≈ 6) should be *ca.* -0.76 V vs Ag/AgCl for the un-doped TiO_2nts, which is near the experimental value. However, the presence of surface states must also be considered, especially for the flat-band shift observed in Figure 43 for the Fe-doped TiO_2nts.

As the XPS studies revealed a predominance of Fe^{2+}, the substitution is reckoned to be of Fe^{2+} for Ti^{4+} in the TiO_2 lattice as described by Eq. (26) according to Kröger-Vink notation.

$$Fe_{Ti} \rightarrow Fe_{Ti}^{''} + 2h^{\circ} \qquad (26)$$

From the values of the charge carrier concentrations, the calculated amount of ionized Fe acceptors amounts to about 0.1 at%, which can be compared with the total iron content of about 1 at%. Whereas the latter contains the contribution by the presence of some $FeTiO_3$, the former corresponds to the electrically active substitutional iron on titanium sites. Some supplementary iron might also be trapped by interaction with oxide ion vacancies, giving uncharged defect complexes ($Fe_{Ti}^{''}V_o^{\circ\circ}$). Thus, the Fe^{2+} dopants are acceptors and this is confirmed by the decrease of the charge carrier concentration of the Fe-doped TiO_2nts in comparison to that of the undoped TiO_2nts. The observed shift of the flat-band potential towards a more negative value due to a transition metal (cationic) substitution is in agreement with previous reports in literature[203, 211] and it is advantageous, since large and negative flat-band potentials are required for an effective charge separation (low recombination probability) in a semiconductor[203, 211].

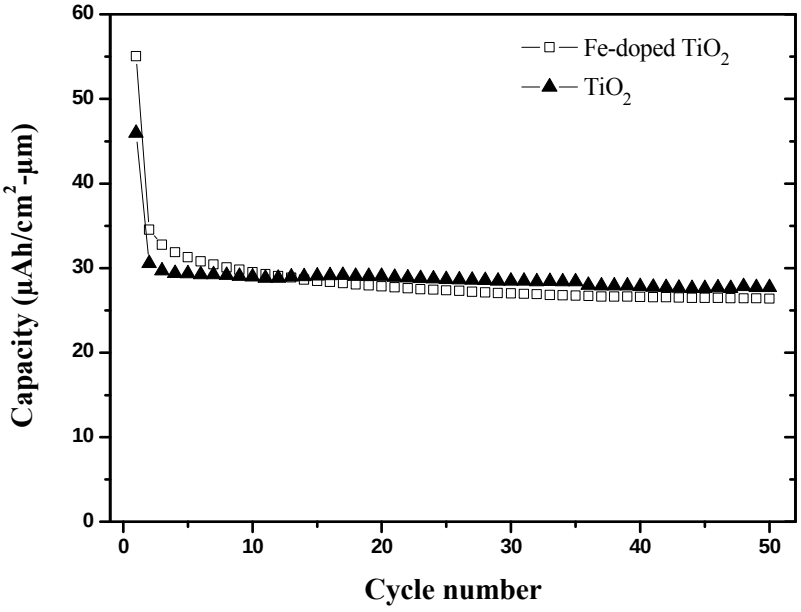

Figure 44 Galvanostatic cycle life performance at 70 µA cm^{-2} for undoped and Fe-doped TiO_2nts in the $1.0 \leq U/V \leq 2.6$ voltage range.

On the other hand, the decrease of the charge carrier concentration is indicative of reduced electronic conductivity. The conductivity (σ) of a semiconductor can be estimated using the charge carrier concentration (N_i), the electron mobility (μ_i =2×10^{-4} cm^{2}V^{-1}s^{-1} for a nanostructured TiO_2) and the elementary charge (q_i =1.6×10^{-19} C) according to Eq.(22). Hence, the conductivity values were estimated to be 2.1×10^{-3} and 1.6×10^{-3} Scm^{-1} for the undoped TiO_2nts and Fe-doped TiO_2nts respectively, agreeing with the assertion that electronic conductivity is reduced in the Fe-doped TiO_2nts. As a result of this reduced electronic conductivity, the Fe-doped TiO_2nts did not deliver higher lithium storage capacities (with cycle number) in comparison to the undoped TiO_2nts (Figure 44).

4.3. TiO_2nts with NiO or Co_3O_4 Sub-µm Particles: Composites for Li-ion Microbatteries

In this section, synthesis of composites of TiO_2 nanotubes with NiO or Co_3O_4 submicron particles and their electrochemical behaviour is discussed. So far as lithium-ion batteries are concerned, transition metal oxides are anticipated to be the best potential anode material to replace graphite since they deliver twice the capacity per unit mass and three times the energy density of graphite[47, 214]. Transition metal oxides (both monoxides and spinels) do not possess vacant sites for lithium-ion insertion but they have been predicated to react with lithium according to the conversion reaction mechanism[47, 49] given in Eq.(27):

$$M_xO_y + 2ye^- + 2yLi^+ \leftrightarrow xM + yLi_2O \quad (27)$$

Since its emergence, the conversion reaction has been extended to sulphides, nitrides, phosphides, hydrides, fluorides and oxysalts[200, 214-216]. However, conversion electrodes also present drawbacks in terms of the irreversibility in the first discharge and the marked voltage hysteresis between discharge and charge curves[49, 214]. In order to circumvent these setbacks

and achieve the commercialization of conversion electrode materials, several tracks such as exploring different synthesis routes, tailoring the chemical composition, and producing small particles with controlled shape and size have been proposed[49, 217]. Besides low-cost and simplicity, electrodeposition is a powerful technique to synthesize various nanomaterials[45, 48, 121, 218]. Compared with other chemical synthesis routes, electrodeposition is particularly efficient to avoid agglomeration of nanoparticles[49, 217, 219]. It has already been demonstrated that electrodeposition of conversion materials onto suitable substrates is a viable approach to design electrodes without the use of binders and/ or conductive agents for 3D lithium (Li-ion) microbatteries[48, 220, 221]. Moreover, TiO_2 nanotubes can indeed be functionalized by electrodepositing secondary materials[45, 55, 192, 222].

4.3.1. Morphology and Structure of Composites

Figure 45a-b show the cross-section and top-view SEM images of the TiO_2nts obtained by potentiostatic anodization in the electrolyte of 1 M H_3PO_4, 1 M NaOH and 0.4 wt% HF. The nanotubes having ~100 nm diameter and ~750 nm length were subsequently used as the substrates for the electrodeposition of Co and Ni particles by galvanostatic experiments. According to Faraday's law, the mass of the two electrodeposited metals is expected to be very close, i.e. 36.64 µg of Co and 36.49 µg of Ni; but Faradaic efficiencies were estimated to be 37% for Ni and 86% for Co according to Inductively Coupled Plasma-Mass Spectrometry (ICP-MS) experiments. The discrepancies can be explained by two side reactions: (i) hydrogen evolution particularly catalysed by the deposited metal, and (ii) reduction of Ti^{4+} (to Ti^{3+}) due to the electro-insertion of H^+ into the TiO_2 lattice[100, 109]. In addition, examination of the surfaces by SEM after electrodeposition of Co (Figure 45c) and Ni (Figure 45d) shows a relatively low density of large Co particles (~600 nm) and a high density of small Ni particles (~170 nm).

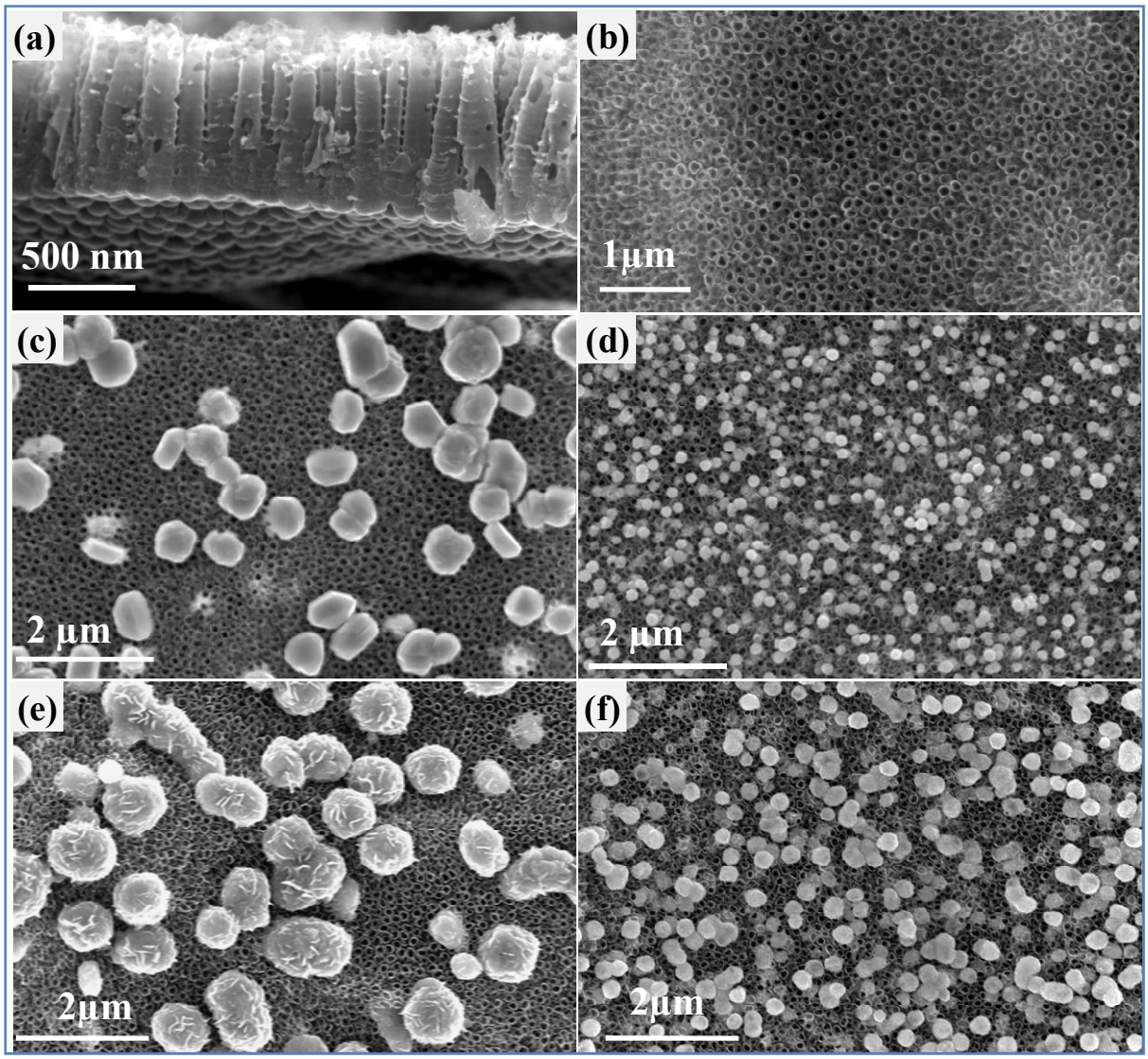

Figure 45 SEM micrographs of as-prepared TiO_2 nanotubes (a: cross-section, b: top-view), TiO_2 nanotubes with electrodeposited cobalt (c) or nickel (d) particles, and TiO_2 nanotubes with Co_3O_4 (e) or NiO (f) particles.

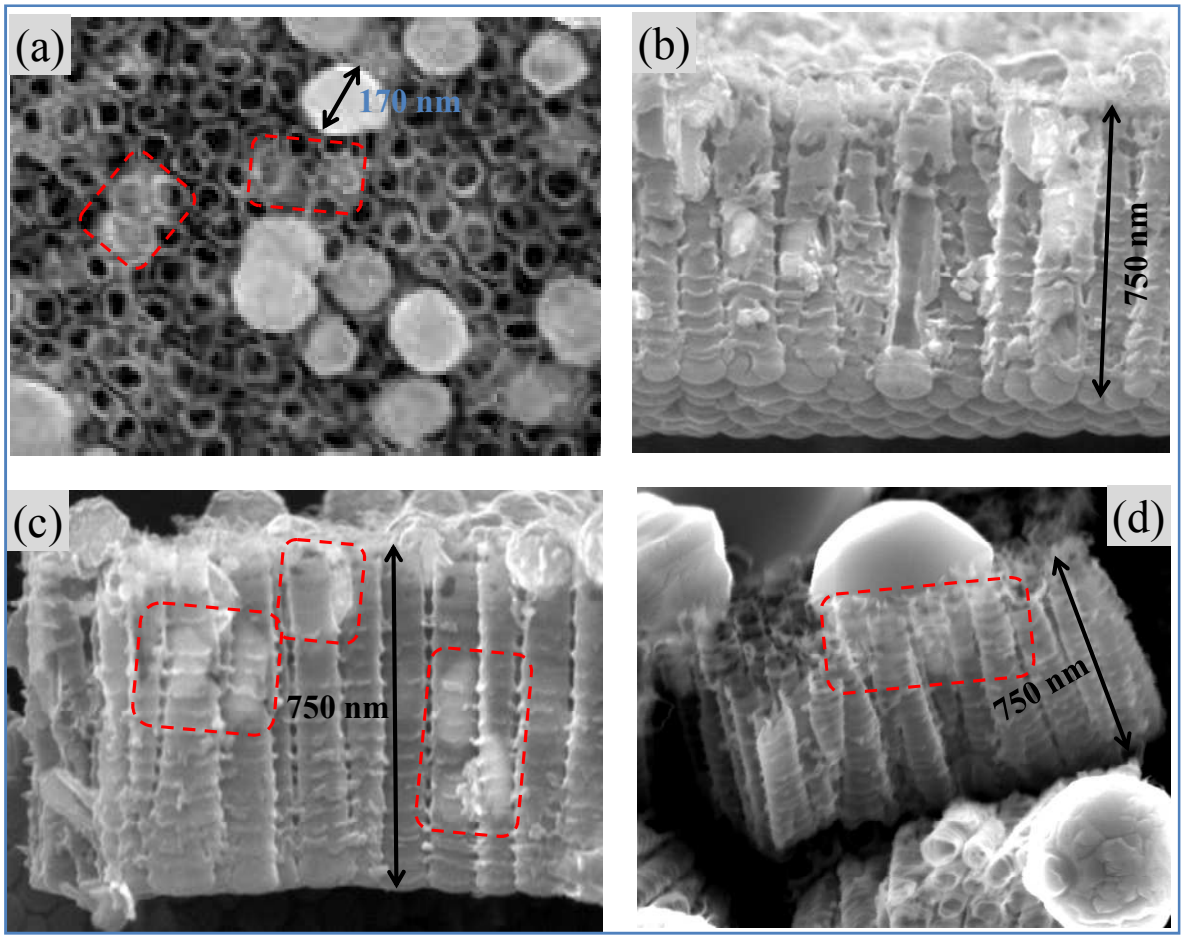

Figure 46 SEM micrographs (some zoomed) depicting that some nuclei of Ni (a-c) and Co (d) are formed on the sidewalls of TiO_2 nanotubes during electrodeposition.

Moreover, after annealing at 500 ºC for the formation of Co_3O_4 and NiO, no significant morphological modifications can be observed (Figure 45e-f) except for a slight swelling of the particles due to the gain of oxygen and some surface rugosity on the Co_3O_4 particles. It can be noticed that the Co particles tend to be coarse and agglomerated while the Ni particles are of uniform shape and size with higher coverage of the TiO_2nt surface. As the deposition conditions were the same, this discrepancy in sizes and particle densities can be explained by different nucleation and growth mechanisms for cobalt and nickel. In fact, the electrodeposition of Co and Ni from sulphate baths onto glassy carbon has been studied by Grujicic *et al*. who reported that the nucleation of Ni is faster and proceeds on a large number of active sites while further growth is inhibited by adsorbed species, such as $H_{(ads)}$ and $SO_4^{2-}{}_{(ads)}$, which is not the case for the nucleation and growth of cobalt [223, 224].

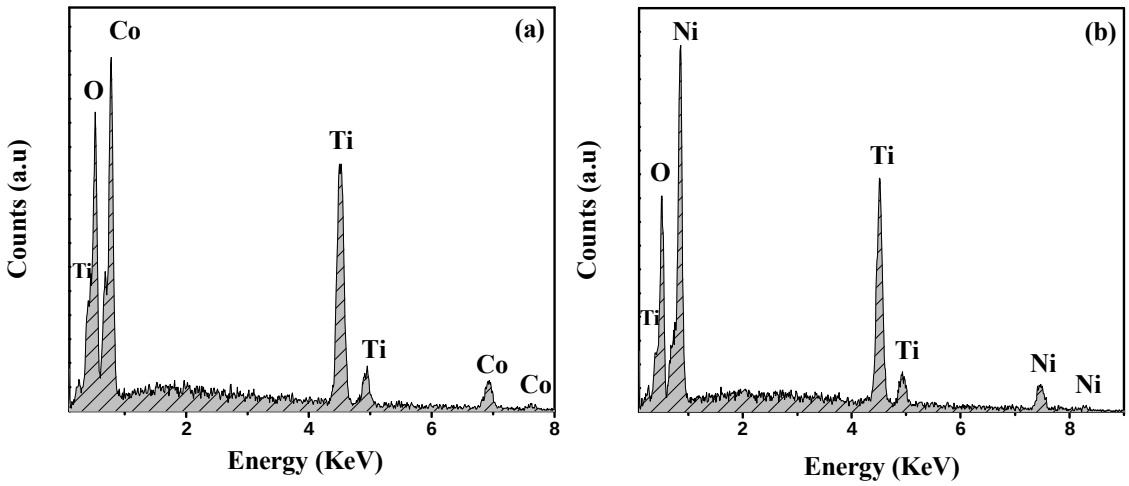

Figure 47 EDS spectra of TiO_2nt layers with (a) cobalt and (b) nickel deposits.

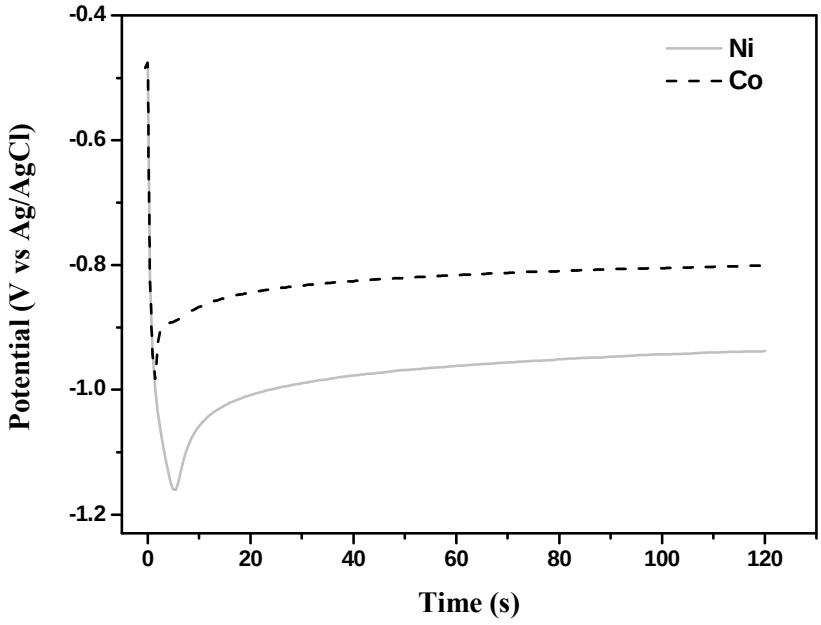

Figure 48 Galvanostatic curves obtained during the electrodeposition of cobalt and nickel particles onto TiO_2nt layers at -2.6 $mAcm^{-2}$. The electrolyte consisted of a mixture of 0.09 M $CoSO_4$ or 0.09 M $NiSO_4$ and 0.1 M $(NH_4)_2SO_4$.

Additionally, the chronopotentiometric curves given in Figure 48 clearly show that electrodeposition of Ni occurs under a higher cathodic overpotential (ΔE~140 mV under steady state), which also favours a higher nuclei density. Indeed, this higher overpotential governing the Ni deposition is coherent with the much reduced Faradaic efficiency (due to

excessive hydrogen evolution) and the observed morphology. These observations could be used to tune particle morphologies through electrochemical parameters. It is obvious from Figure 46 that for both Ni (a-c) and Co (d), some nuclei are formed on the sidewalls of the TiO_2 nanotubes. EDS analyses (Figure 47) confirmed the presence of Co and Ni metal particles in addition to the O and Ti from the underlying TiO_2nt layers. After heat-treatments at 500 ºC, X-ray diffraction (Figure 49) studies confirmed the formation of spinel Co_3O_4 (JCPDS: 42-1467) and NiO (JCPDS: 47-1049) on the crystalline TiO_2nt layers which consist mainly of anatase (JCPDS: 21-1272) and an infinitesimal proportion of rutile (JCPDS: 21-1276).

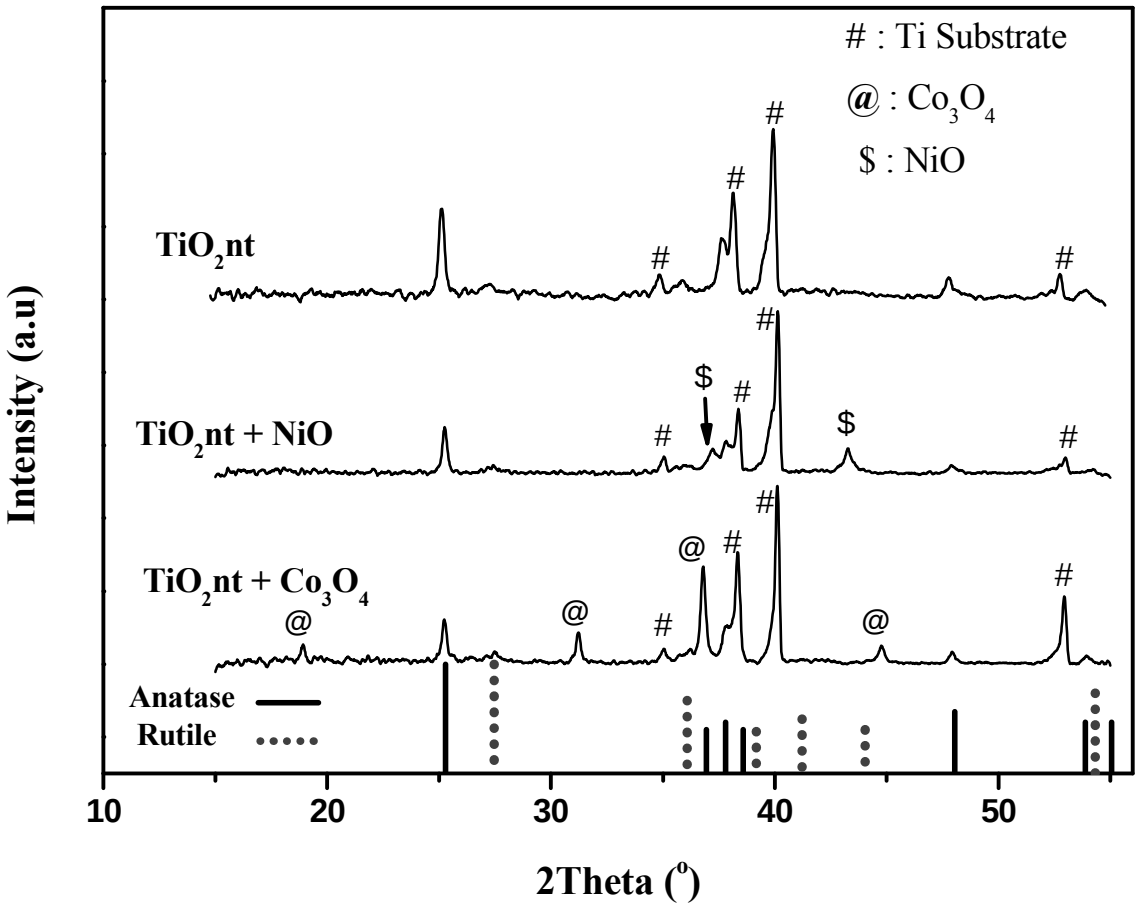

Figure 49 XRD patterns of crystalline TiO_2nts, and crystalline TiO_2nt layers with Co_3O_4 (JCPDS: 42-1467) and NiO (JCPDS: 47-1049) after annealing at 500 ºC. The peaks marked '#' are emanating from the Ti substrate.

4.3.2. Electrochemical Behaviour of Composites

To fully apprehend the electrochemical behaviour of particles-sprinkled TiO_2nts versus lithium, cyclic voltammetry experiments (Figure 50a-c) were carried out in addition to the galvanostatic discharge/charge profiles (Figure 51a-c) recorded during the cycling. Evidently, the CV curves agree well with the recorded discharge/charge profiles.

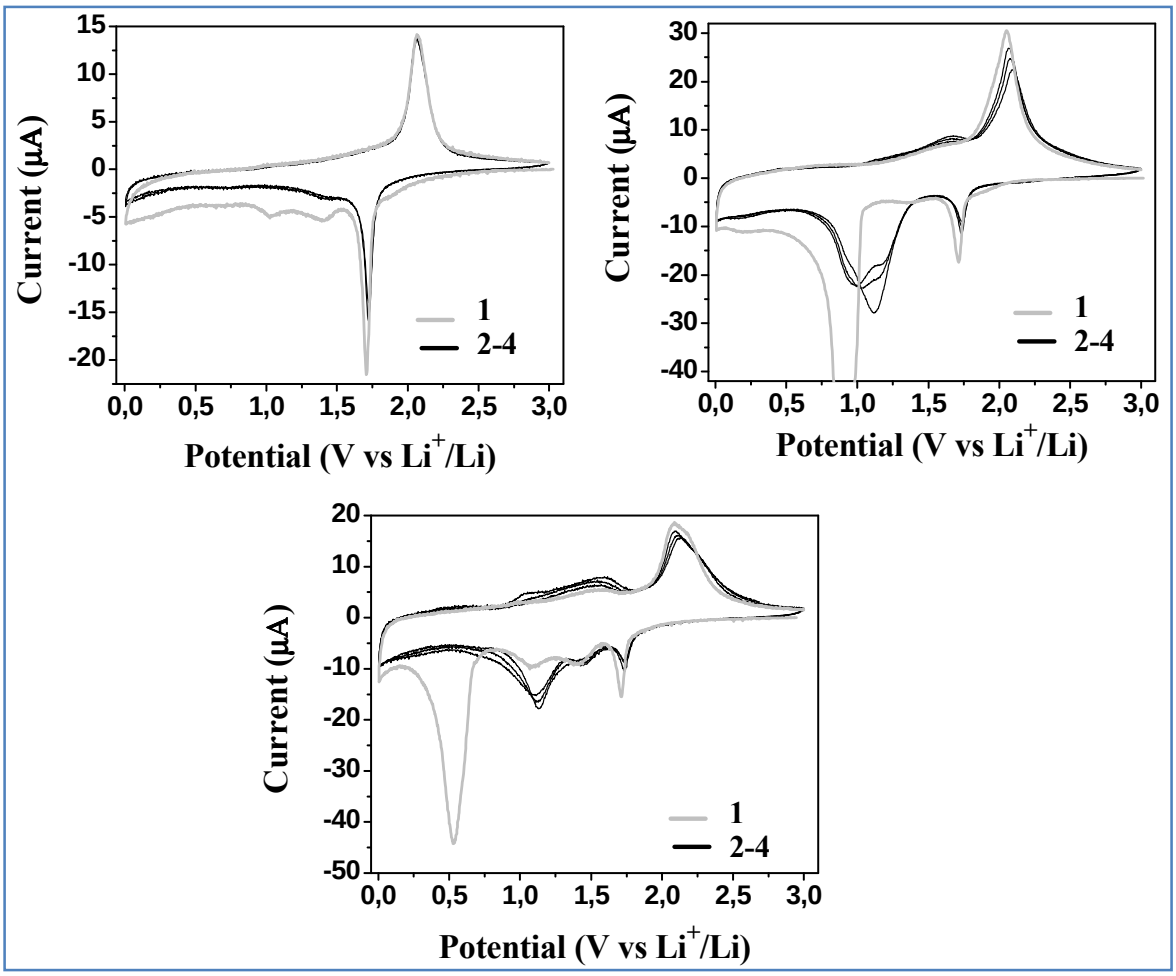

Figure 50 CV curves recorded at 0.1 mVs^{-1} for crystalline TiO_2nt layers without (a) and with particles of Co_3O_4 (b) and NiO(c).

The crystalline TiO_2nts present the characteristic peaks (Figure 50a) of lithium insertion and extraction into and from anatase TiO_2 at ca.1.7 V *vs* Li^+/Li and ca. 2.0 V *vs* Li^+/Li respectively[43, 55]. In addition, peaks of lithium insertion into the small proportion of rutile

TiO_2 detected by XRD (Figure 49) can clearly be distinguished at *ca.* 1.1 V *vs* Li^+/Li and 1.4 V *vs* Li^+/Li in the first cycle. The irreversibility of these two peaks in the subsequent cycles is as a consequence of extensive lithium storage up to the 0.05 V *vs* Li^+/Li cut-off potential, and the concomitant irreversible structural transformations. It is worth noting that rutile TiO_2 is also known to reversibly insert lithium ions [193, 225]. Although the diffusion limitation problem of lithium insertion into rutile TiO_2 at room temperature has been demonstrated to be negligible with nano-sized particles[226, 227], in several reports [56, 197], extensive lithium insertion occurs at potentials below 1.2 V and leads to irreversible structural distortions.

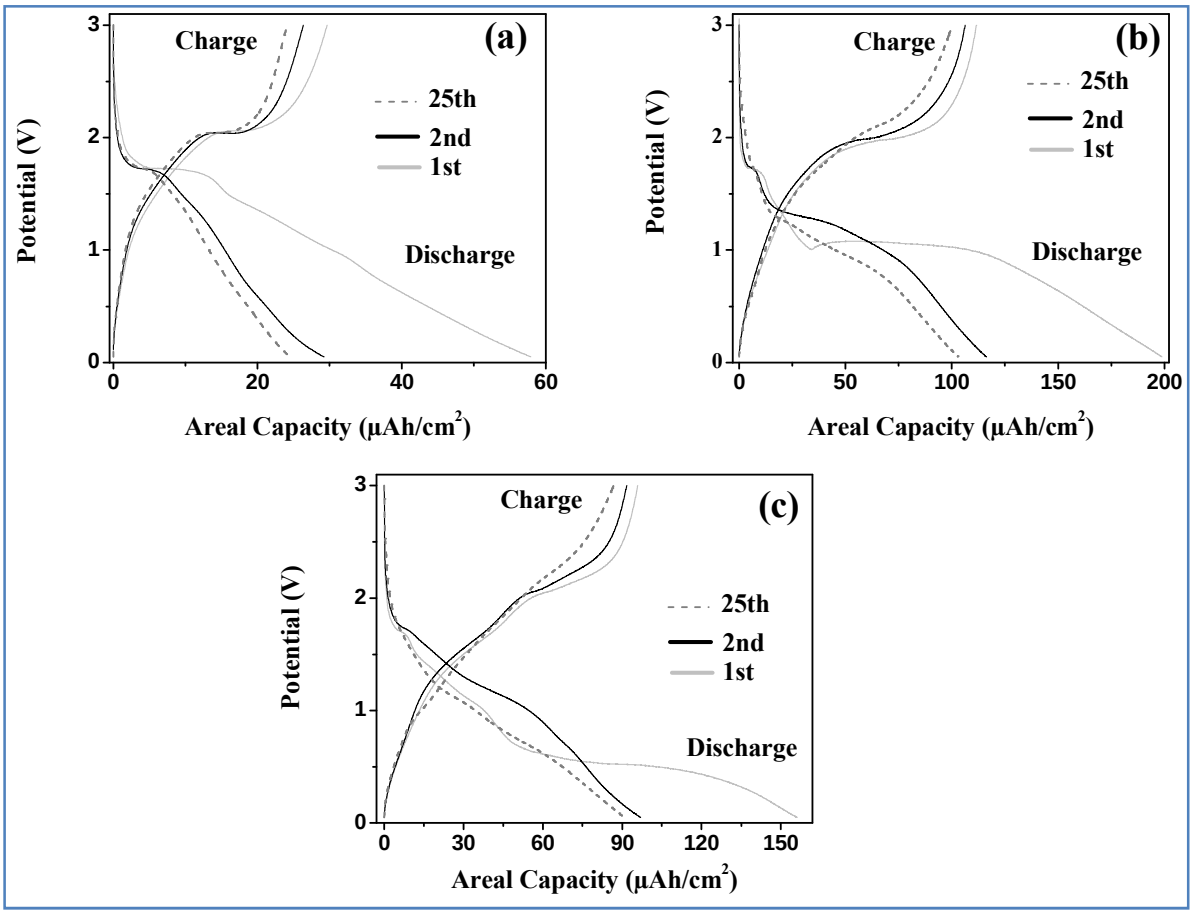

Figure 51 Galvanostatic curves recorded during cycling at 70 µA cm^{-2} for crystalline TiO_2nt layers without (a) and with particles of Co_3O_4 (b) and NiO(c).

In the CV of TiO_2nts with particles of Co_3O_4 or NiO (Figure 50b-c), lithium insertion/extraction into and from anatase TiO_2 at can be easily identified ca.1.7 V *vs* Li^+/Li and ca. 2.0 V *vs* Li^+/Li. For the Co_3O_4 sample, the peaks of lithium insertion into the small proportion of rutile TiO_2 are partly merged with the position of the cobalt reduction peaks (Figure 50b) but can be clearly seen at *ca.* 1.1 V and 1.4 V *vs* Li^+/Li for the NiO sample. Typical for most conversion electrodes, the strong peak at *ca.* 0.9 V *vs* Li^+/Li for the simultaneous reduction of the cobalt ions ($1Co^{2+}$, $2Co^{3+}$) in the first cycle was shifted to *ca.* 1.1 V *vs* Li^+/Li in the subsequent cycles [49, 221]. Similarly, the reduction of the nickel ions occurring at *ca.* 0.5 V *vs* Li^+/Li in the first cycle was shifted to *ca.* 1.1 V vs Li^+/Li in the subsequent cycles.

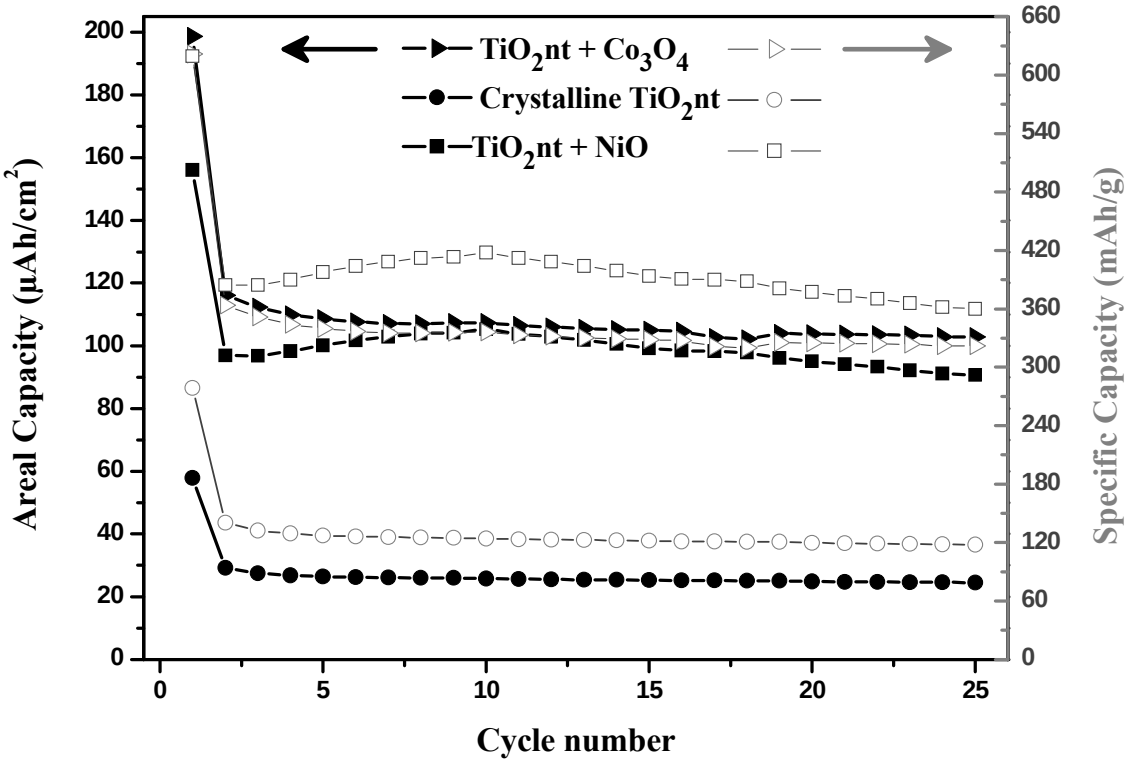

Figure 52 Galvanostatic cycle life performance at 70 µA cm^{-2} in the $0.05 \leq U/V \leq 3$ voltage range for crystalline TiO_2nt layers without and with particles of Co_3O_4 or NiO.

For conversion reactions, the voltage of the first discharge plateaus (Figure 51b-c) are closely related to the Gibbs free energy for the reduction of the transition metal oxides to the

metallic state and hence depend on the oxide composition [228]. The footprint of the first reduction process is the representative voltage plateau having extension typically equivalent to the amount of electrons required to fully reduce the oxide [214, 228]. Further discharges result in entirely different voltage profiles which imply that the first electrochemical cycles restore only partially the morphology and stoichiometry of the initial oxide particles [121, 228].

In Figure 52, the galvanostatic cycle life performance of the particles-sprinkled TiO_2nts is compared to that of crystalline TiO_2nts in the units of $\mu Ahcm^{-2}$ and mAh/g. Here also, the approximate mass (m) of the TiO_2 nanotubes was estimated to be ~80 µg using: $m = V \times \rho \times P$, where ***P****(The porosity)* was estimated to be ~50% according to geometrical considerations from SEM micrographs[100, 195, 196], ***V****(Volume of nanotubes)* ≈ 3.848 $\times 10^{-5}$ cm^3, and $\boldsymbol{\rho}$(Density of anatase TiO_2), = 4.21 g cm^{-3}. Once again, due to the theoretical estimation of the mass of the TiO_2 nanotubes, it can be emphasized that the capacity values given in $mAhg^{-1}$ for the TiO_2 nanotubes are slightly underestimated.

The amount of Co or Ni deposited on the TiO_2 nanotubes was determined by Inductively Coupled Plasma-Mass Spectrometry (ICP-MS) using an *HP 4500 ICP-MS* (*Yokogawa Analytical Systems*), and using the molar ratios from equations (28) and (29), the corresponding amount of Co_3O_4 or NiO was estimated.

$$Co + \frac{2}{3}O_2 \rightarrow \frac{1}{3}Co_3O_4 \qquad (28)$$

$$Ni + \frac{1}{2}O_2 \rightarrow NiO \qquad (29)$$

For TiO_2 electrodes, it has already been established that despite a very thin or inexistent solid electrolyte interphase (SEI) layer, irreversible side reactions with adsorbed solvents on surfaces of amorphous samples or crystallized water in the case of annealed samples contribute to the irreversible capacity between the first and the second cycles[43]. For the

composite electrodes, obviously, there is the contribution from TiO_2 in addition to that of the conversion reaction. For 'convertible' electrodes, there are three causes for the irreversible capacity between the first and the second cycles: i) irreversible electrolyte decomposition, ii) incomplete de-conversion due to the presence of inactive or electrically disconnected Li_2O/M regions, and iii) partially restored morphology and stoichiometry of the initial oxide particles [121, 214, 228].

It is apparent that the capacity values delivered during the first 25 cycles are approximately ~4 times higher in the units of $\mu Ahcm^{-2}$ (or ~3 times higher in the units of mAh/g) due to the presence of Co_3O_4 or NiO particles on the TiO_2nts. Particularly, the electrode based on TiO_2nt modified with Co_3O_4 particles has good capacity retention over the first 25 cycles (103 $\mu Ahcm^{-2}$). Nevertheless, the gain in capacity from this electrode is minimal considering that Co_3O_4 is supposed to react with $8Li^+$ [Eq. (30)] whereas NiO only reacts with $2Li^+$ according to Eq. (31).

$$Co_3O_4 + 8e^- + 8Li^+ \leftrightarrow 3Co + 4Li_2O \quad (30)$$

$$NiO + 2e^- + 2Li^+ \leftrightarrow Ni + Li_2O \quad (31)$$

The minimal gain in capacity observed for the Co_3O_4–based composite could be explained by the different morphologies of the deposits. The higher particle-density of the Ni deposit combined with no agglomeration is supposed to increase the specific surface and as a consequence, a larger electrode/electrolyte interface is formed leading to a higher number of active sites that can easily react with Li^+. The minimal gain in capacity could also be due to the recently published[229] fact that a full restoration of the Co_3O_4 stoichiometry does not occur during reaction with lithium. That is, an initiation reaction between Co_3O_4 and lithium [Eq. (30)] occurs followed by a reversible reaction employing CoO [Eq. (32)]:

$$Co + Li_2O \leftrightarrow CoO + 2Li^+ + 2e^- \quad (32)$$

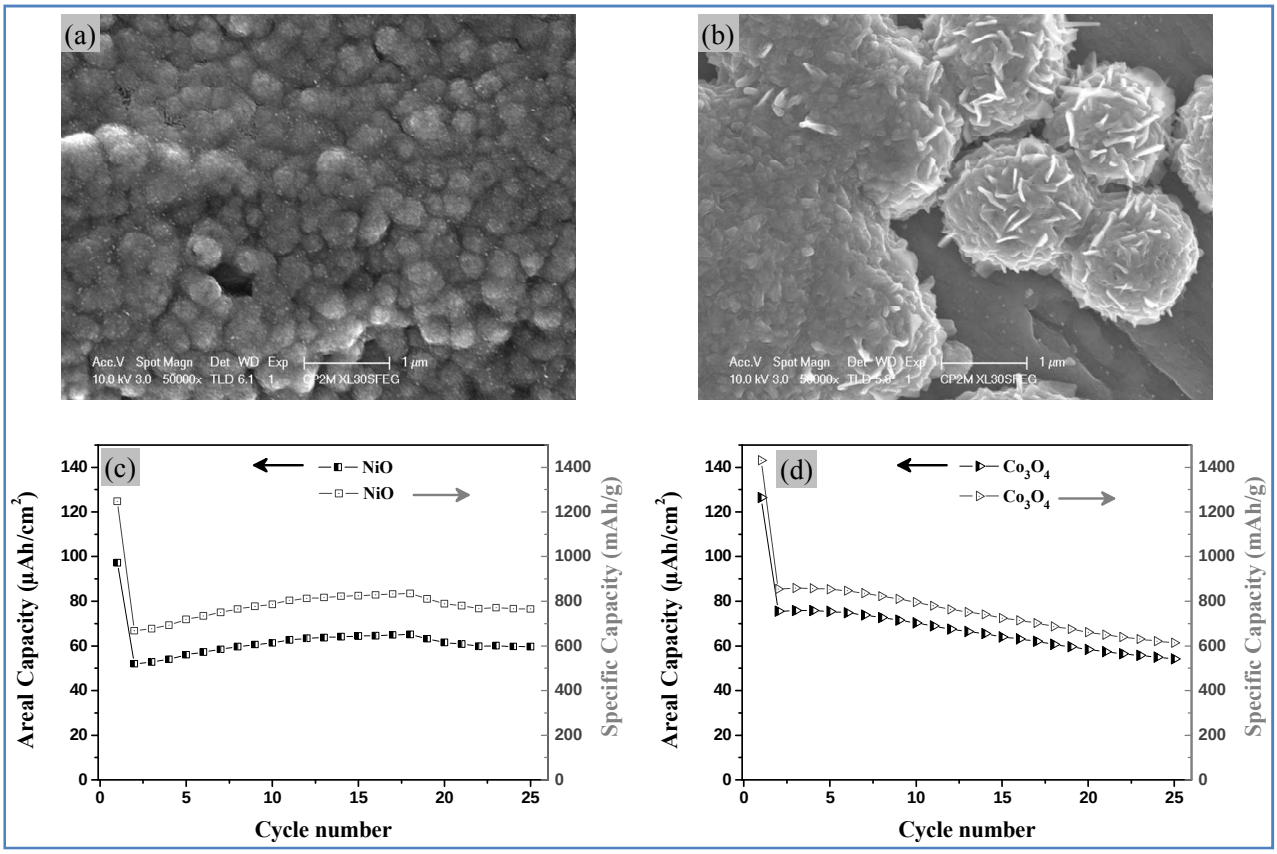

Figure 53 SEM micrographs of NiO (a) and Co_3O_4 (b) prepared by annealing Ni and Co films electrodeposited onto stainless steel substrates; and their (c: NiO and d: Co_3O_4) galvanostatic cycle life performance at 1C in the $0.05 \leq U/V \leq 3$ voltage range. The capacity values are given in $\mu Ahcm^{-2}$ (semi-closed symbols) and in $mAhg^{-1}$ (open symbols).

For comparison, electrodes of bare NiO and bare Co_3O_4 were prepared by annealing Ni and Co films electrodeposited onto inactive stainless steel substrates. It can be seen from Figure 53a that the nickel particles tend to agglomerate leading to a continuous film on the stainless steel substrate, whereas the Co deposit (Figure 53b) consists of large islands leading to a discontinuous film even though both metals were deposited at the same conditions as were previously adopted for the composites. The nucleation mechanism leading to these morphological differences on the metal substrate is consistent with what was explained above with the semiconductor TiO_2nt substrate. Figure 53 shows the specific and areal discharge

capacities of the bare NiO (c) and Co_3O_4 (d) electrodes at 1C-rate (NiO:27 $\mu A/cm^2$; Co_3O_4:10 $\mu A/cm^2$). Obviously, the specific capacities delivered by the bare NiO and Co_3O_4 electrodes are comparable to previous reports in literature [229-232]. It can be noted in Figure 52 and Figure 53 that although the areal capacities of the composite electrodes are higher than those of the bare NiO and Co_3O_4 electrodes, the contrary is observed in terms of specific capacities, and this is consistent with the much higher weights of the composite electrodes. Moreover, the bare Co_3O_4 electrode presents considerable capacity fading within the first 25 cycles (Figure 53). This capacity fading is consistent with previous reports on Co_3O_4 electrodes [229, 233], but it was circumvented with the Co_3O_4-based composite electrode (Figure 52), most probably as a result of the morphological differences. On the other hand, the bare NiO and the NiO-based composite electrodes exhibit the same superior cycle life performance within the first 25 cycles.

4.4. TiO_2nts with Gel-like PEO-PMMA Layers: Towards 3D Microbatteries

In this section, the deposition of a polymer electrolyte into TiO_2 nanotubes is discussed. Polymer electrolytes have been widely studied as solid electrolytes for lithium batteries[234-237]. These ionically conducting but electronically insulating electrolytes are made by blending polyethylene oxide (PEO)-based materials with a lithium salt (eg. LiTFSI). Although most of them operate above room temperature, a few have been demonstrated to exhibit room temperature conductivity–by modifying the physical properties of the polymer[238-240]. Basically, for room temperature conductivity, the high molecular weight polymers are plasticized by introducing ceramic fillers for a decreased crystallinity. Patel *et al*.[241] recently synthesized a soft (gel-like) polymer electrolyte for room temperature lithium-polymer batteries.

The choice of electrolyte for lithium microbatteries is indeed a problem, but it is an undisputable fact that polymer electrolytes with room-temperature conductivity are potential candidates. Of course, liquid electrolytes cannot be adopted due to problems of leakage, volatility and flammability. And for the solid (ceramic) electrolytes, substantial conductivity at room temperature is indispensable. The ceramic $Li_{0.35}La_{0.55}TiO_3$ has been reported as an all-solid-state electrolyte for 3D microbatteries. However, it is an expensive material with limited possibilities to suit all different designs and materials, and leads to considerably low discharge capacities[40, 242]. Kotobuki *et al*.[243-245] have also demonstrated that $Li_7La_3Zr_2O_{12}$ solid electrolyte is one of the promising electrolytes for all-solid-state batteries due to its high Li^+ conductivity and stability against Li metal anode.

To date, $Li_{2.9}PO_{3.3}N_{0.46}$ (LiPON) has been the best choice of solid electrolyte for lithium-based microbatteries[22, 23], although derivatives of LiPON such as LiSiPON and LiPONB have also been reported[53, 246, 247]. The glassy LiPON electrolyte exhibits good Li^+ ion conductivity (~2-5 μS/cm) at room temperature and electrochemical stability above 4.5 V, but

the top-down (thin-film) technologies employed for depositing these electrolytes are not adequate to achieve a conformal deposition onto the walls of nanostructured electrodes for the fabrication of 3D microbatteries. In view of this, electropolymerization is deemed a convenient bottom-up approach to deposit low molecular weight (gel-like) polymers (with instantaneous lithium salt incorporation) into nanostructured electrodes for the fabrication of 3D (all-solid-state) microbatteries that can operate at room temperature. It is important to mention that it was in 1989 that Ogumi *et al*.[248, 249] first demonstrated the idea of using PEO-based polymer electrolytes for all-solid-state microbatteries. In 1993, West *et al*[250] also studied thin-film electrodes with PEO-based polymer electrolytes just that their cells operated at elevated temperatures. Recently, several groups have also made substantial efforts to utilize polymer electrolytes based on phenol[251], Poly(propylene oxide)[252, 253], PMMA[254, 255], and PEO-polystyrene[256] for the design of lithium-based microbatteries.

4.4.1 Polymer Deposition and Characterization

Electrochemical polymerisation (ECP) is a powerful technique for depositing thin passive films onto materials for corrosion protection and adhesion enhancement. It is also widely adopted to produce highly pure polymer films for applications in electrocatalysis, micro-optoelectronics, and photo-electrochemistry [257-263]. Depending on the role of the working electrode (anode or cathode), the electropolymerization mechanism can be cationic, anionic, or free radical. The polymerization process can be initiated by the monomer or by added initiators when the monomer is not electrochemically active.

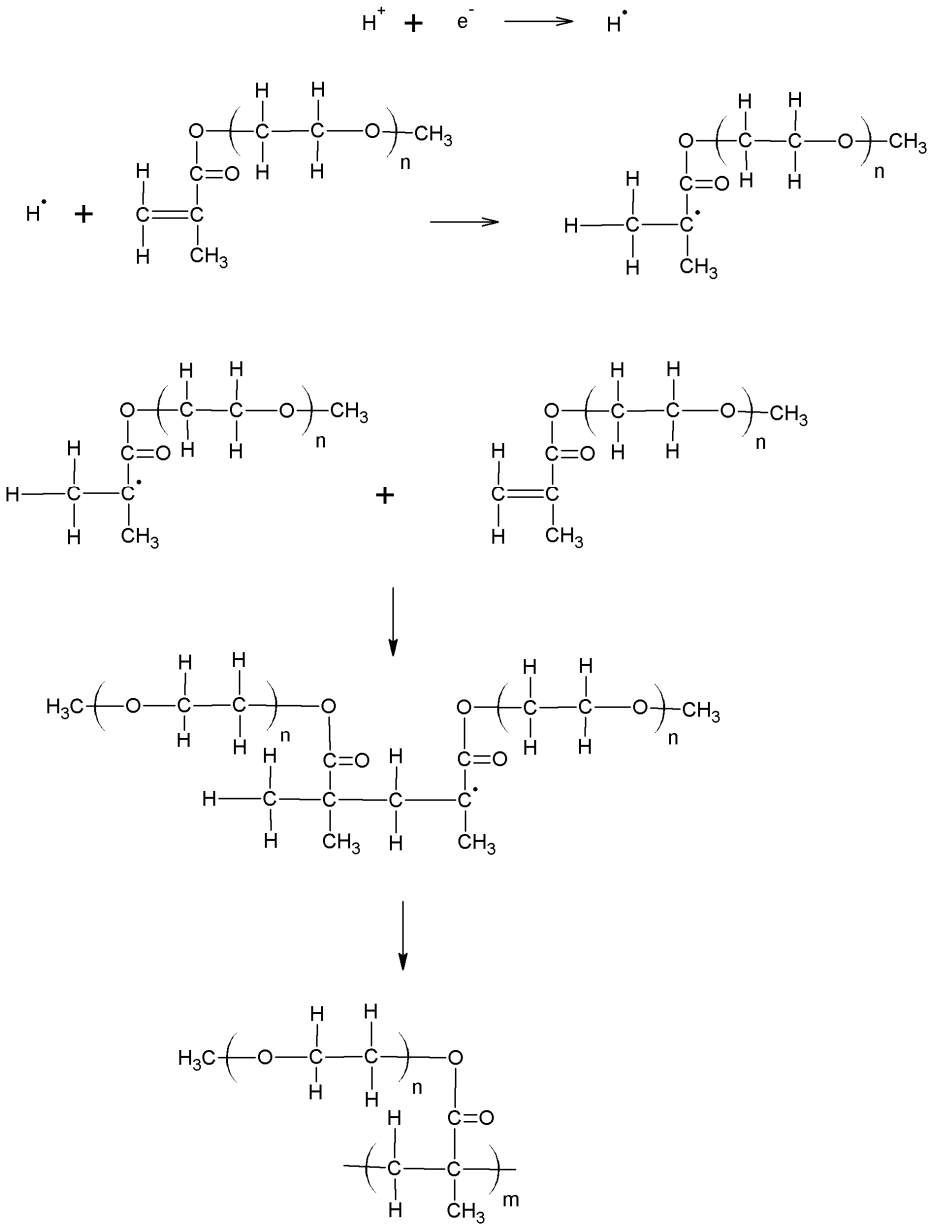

Scheme 1. Electropolymerization of PEO-functionalized methyl methacrylate based on the free radical mechanism.

Herein, the electropolymerization is expected to occur according to the free radical mechanism proposed by Cram *et al.* [262] (The mechanism is given in Scheme 1). The reduction of H^+ to produce H_2 is accompanied by the formation of $H^\bullet$ radicals that can react with the monomers leading to the polymerization of methyl methacrylate. The possible free radical-induced electropolymerization mechanism is confirmed through the examination of the cyclic voltammograms given in Figure 54. Actually, the similar general shape of both polarization

curves indicates that only the reduction reactions of H^+ and TiO_2 take place within the studied potential window. In accordance with the Nernst equation, the increasing cathodic current starting at around -0.66V/SCE is attributed to the reduction of H^+ and the production of $H^\bullet$ radicals, which are responsible for the polymerization process. At -1.22V/SCE applied potential, it can be observed the reduction of Ti^{4+} into Ti^{3+} ions with its counter reaction on the reverse scan as has been reported in literature [264]. At more cathodic potentials, H_2 evolution becomes predominant. The main difference between these two voltamogramms is the kinetics of the reactions. Indeed, when the polarization is performed in the monomer-containing electrolyte, lower current densities are recorded on both scans. This result clearly shows the formation of an insulator layer hindering the redox reactions.

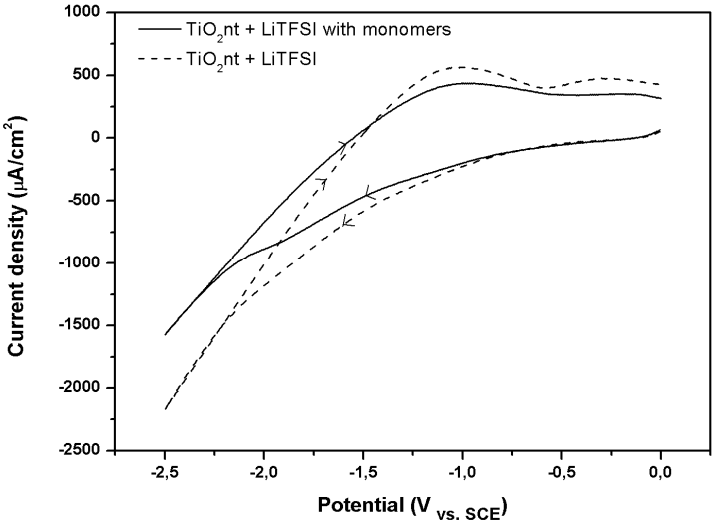

Figure 54. Cyclic voltamogramms recorded between 0V and -2.5V vs SCE for TiO_2nts layer in 0.035 M LiTFSI aqueous solution, and in 0.035 M LiTFSI aqueous solution + 2g PEO-functionalized MMA. Sweeping rate of 25mV/s.

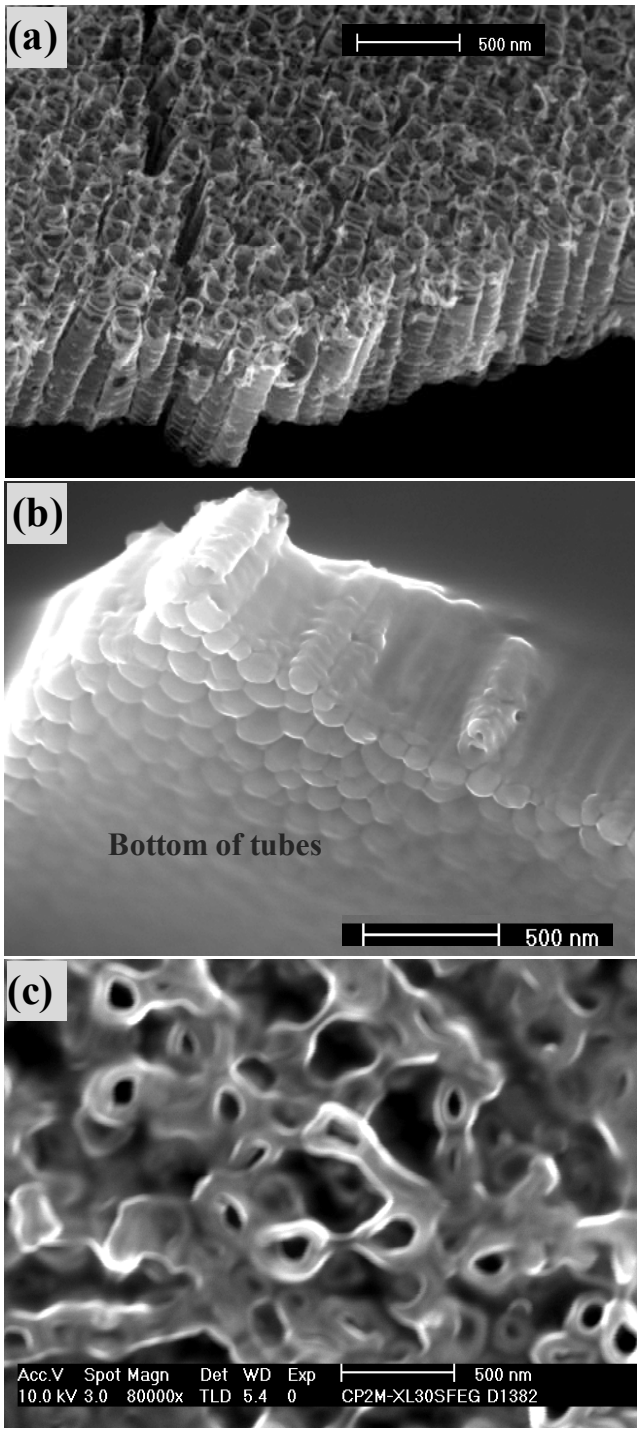

Figure 55 SEM images of as-formed TiO_2nts (a), and copolymer-embedded TiO_2nts (b: cross-section, c: top-view).

The deposition of the copolymer into the titania nanotube layer was confirmed by morphological and chemical analysis. The SEM image of as-formed titania nanotubes that are ~750 nm long with diameters of around 100 nm can be compared with the polymer-embedded titania nanotube layer (Figure 55a-b). Apparently, the nanotubes are almost

completely filled by a thin polymer film suggesting that the electrodeposition begins from the bottom of the nanotubes [171, 263]. The thickness of the polymer layer at the top of the nanotubes was estimated to be ~120 nm, but the polymer coating on the exterior walls of the nanotubes is very thin (20-30 nm), permiting to easily discern the TiO_2 nanotubes from the cross-sectional SEM image (Figure 55b) without any metallization of the polymer layer.

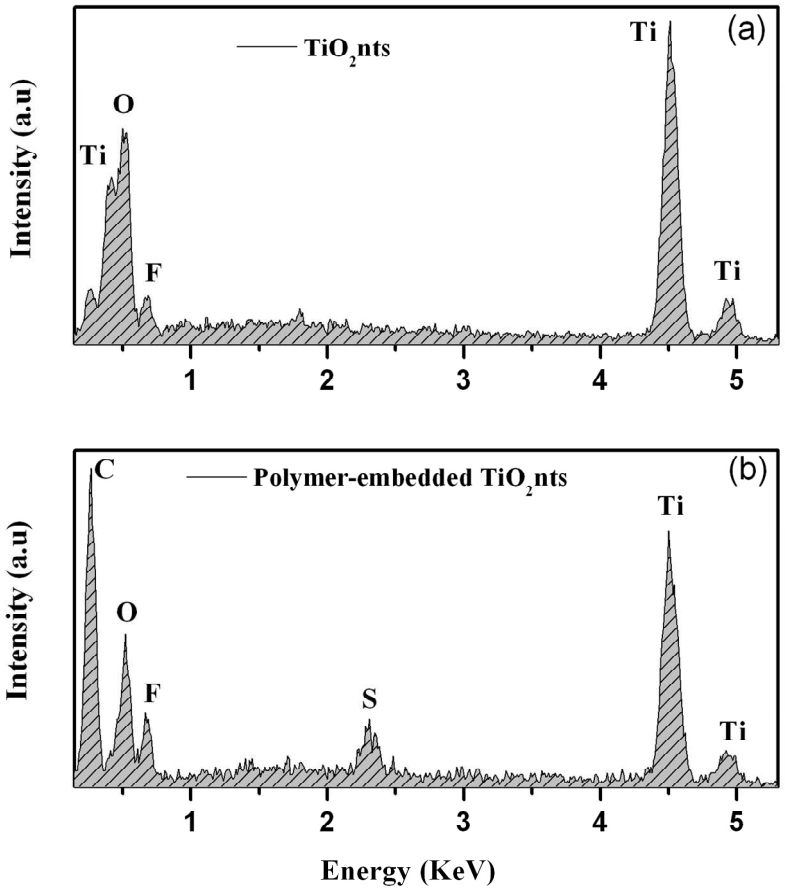

Figure 56 EDS spectra of (a) as-formed TiO_2nts, and (b) copolymer-embedded TiO_2nts.

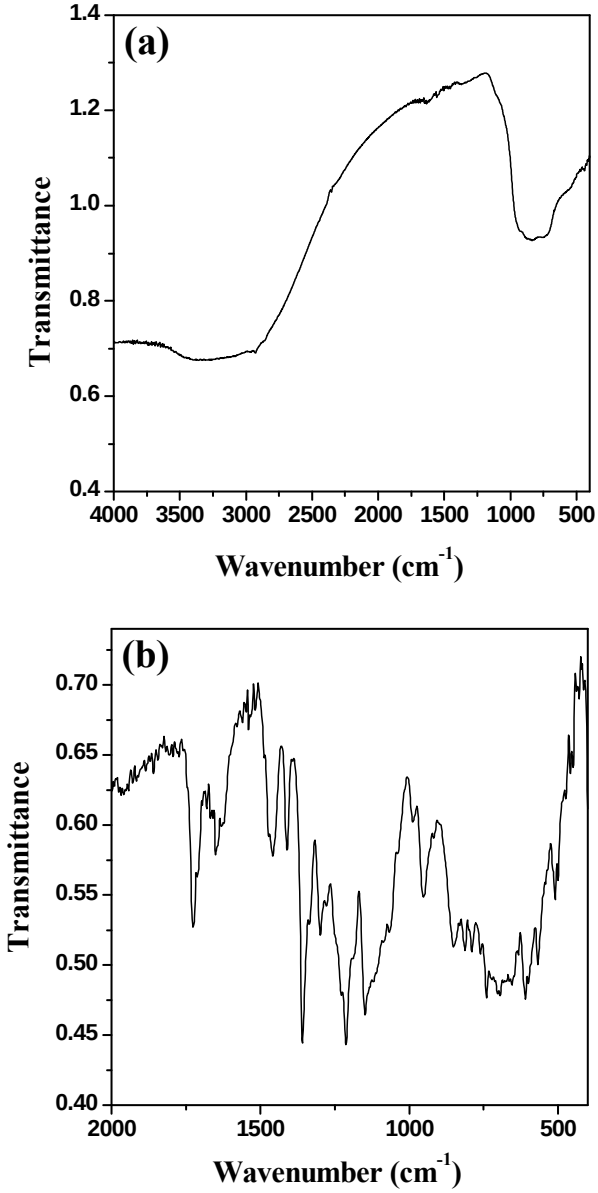

Figure 57 FTIR spectra of as-formed TiO_2nts (a) and copolymer-embedded TiO_2nts (b).

A fine control of the copolymer thickness can be achieved because the growth mechanism depends on the monomer concentration and on the bath immersion time once the free radicals are formed. The EDS spectra shown in Figure 56 depicts very high carbon content for the polymer-embedded nanotubes. The sulphur of the incorporated LiTFSI salt was also detected. The source of the carbon was clearly identified to be the copolymer by FTIR spectroscopy (Figure 57). Indeed, PEO and PMMA bands can be easily identified (see the corresponding band values obtained from literature in Table 2) [257, 258, 265, 266]. It can be noted that no such bands are present in

the FTIR spectrum obtained from the as-prepared TiO_2nt sample, which displays just the Ti-O-Ti stretching mode[267] of TiO_2 at less than 1000 cm^{-1}.

The generation of the copolymer by electropolymerization was confirmed by ^1H NMR experiments. The high solubility of the resulting PEO-PMMA in water enabled its removal from the nanotubes by dissolution and further analysis in both organic and aqueous solvents were then carried out. The ^1H NMR spectra were recorded in $CDCl_3$. Examination of the ^1H NMR spectrum of the polymer evidences the disappearance of the characteristic set of peaks of the vinylic group located at 5.57 and 6.12 ppm respectively, therefore demonstrating that a reduction of the methylmethacrylate group had occurred (Figure 58). Formation of the copolymer is also corroborated by the strong shift observed for the methyl group of the methacrylic unit which shifts from 1.95 ppm to 1.48 ppm, thus confirming the polymerization and the formation of a saturated chain. Broadening of all the signals is also in agreement with the formation of a polymer, this phenomenon being typically observed for the NMR spectra of polymers.

Table 2 Typical FTIR peak positions of PMMA-b-PEO

Peak Position (cm^{-1})	**Peak Assignment**
2880	C-H stretching vibration in PMMA
1730	C=O Carbonyl stretching group in PMMA
1640	Adsorbed water assigned to the δH-O-H bending mode
1460	CH_2 asymmetric bending in PEO
1346-1360	CH_2 wagging in PEO
1300	O-CH_3 stretching vibrations in PMMA
1250-1280	CH_2 twist
1200-1212	C-O stretching vibrations
1147-1150	C-O stretching vibrations
1104	C-O-C stretching vibrations in PEO
850	CH_2 rocking in PEO

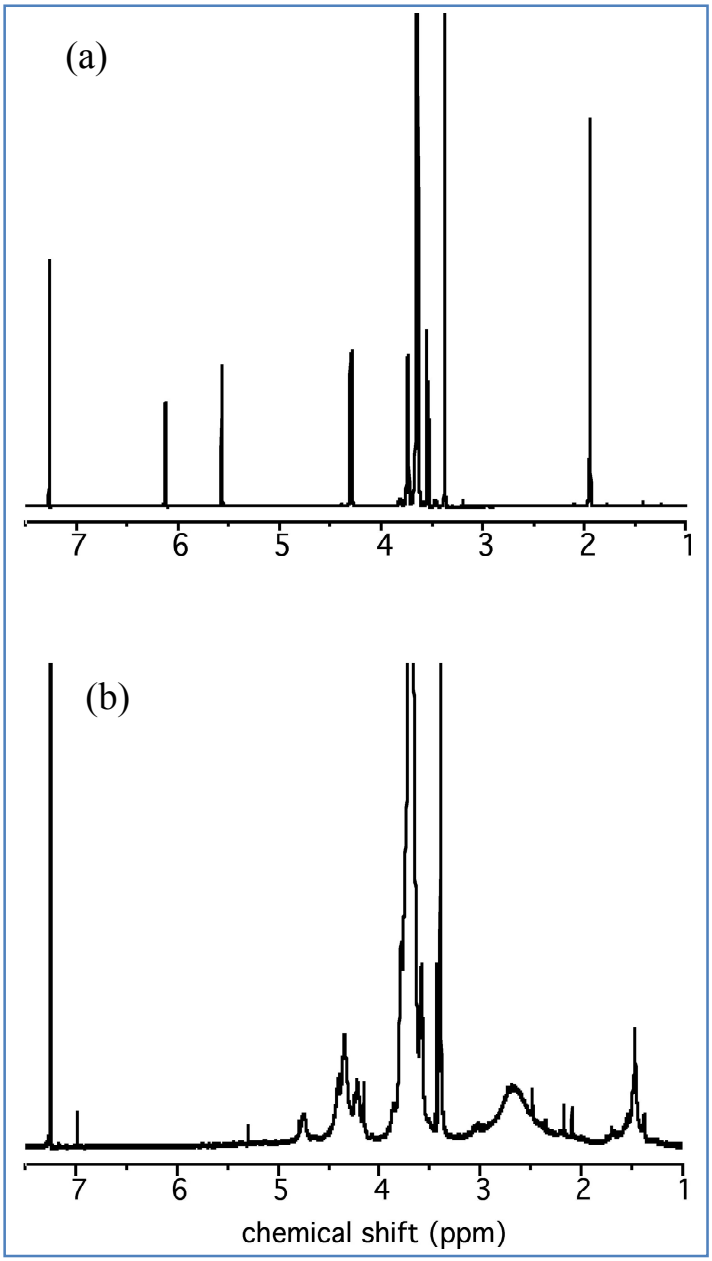

Figure 58 ^{1}H NMR spectra of the starting monomer (a) and the resulting polymer (b).

Finally, careful analysis of the ^{1}H NMR spectrum evidences the formation of copolymers of various lengths by the presence of several signals located between 4.0 and 4.6 ppm and assigned to the CH_2 group of the ester. To verify that the polymeric material was not issued from a simple electrochemical reduction of the methacrylic group, a comparison with the ^{1}H NMR spectrum of a model ester molecule (ethyl isobutyrate) that bears an isopropyl group was carried out (see Figure 59). Comparison of both NMR spectra clearly indicates that the septuplet of the CH group at 2.48

ppm and the doublet of the CH_3 groups at 1.12 ppm of ethyl isobutyrate were not observed on the NMR spectrum of the electropolymerized material, therefore providing another proof for the formation of the desired polymer. A further evidence of polymerization was provided while comparing our NMR spectrum with the ^{1}H NMR spectra of PEO-PMMA copolymers synthesized by various techniques such as ATRP (Atom Transfer Radical Polymerization), [268, 269] photopolymerization, [270] anionic polymerization [271] and free radical polymerization [272]. In each case, a good agreement was determined between the chemical shifts reported in the literature for both the CH_3 and the CH_2 groups of the PMMA chains and the chemical shift of the same groups for the electropolymerized material.

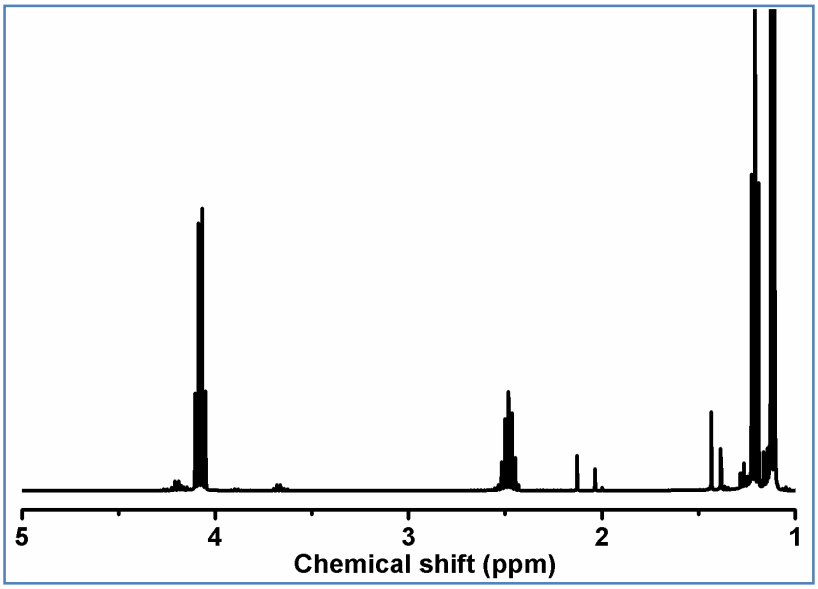

Figure 59 ^{1}H NMR spectrum of the ethyl isobutyrate recorded in $CDCl_3$.

The polymeric material was also investigated by Size Exclusion Chromatography (SEC), applying a RI detector and PS standards. Comparison of the SEC traces of both the monomer and the electropolymerized material confirmed the formation of a copolymer (see Figure 60). Although the retention time of the polymeric material is close to that of the monomer, a clear broadening of the trace with a slightly shorter retention time compared to the monomer can be

observed, indicating the formation of polymers.

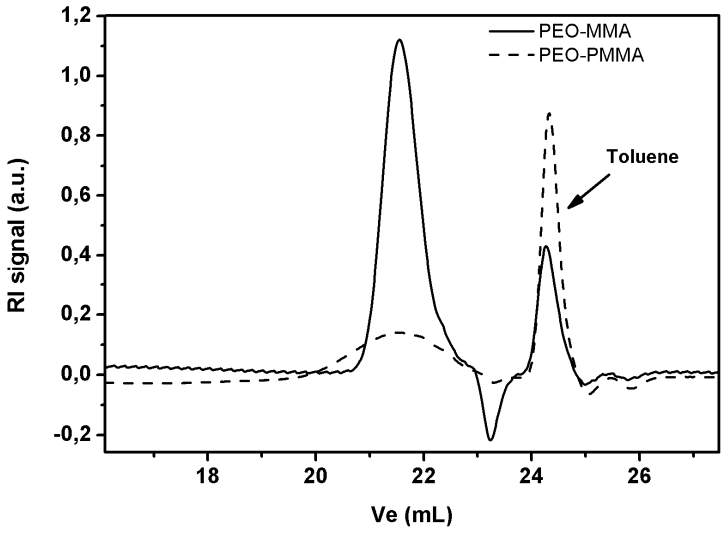

Figure 60 SEC traces of the monomer (solid line) and the polymeric material (dotted line). Eluent system: THF + 0.25%vol toluene as the internal reference.

As the electropolymerization does not induce significant changes in the retention time, formation of oligomers instead of polymers is also evidenced. No traces of high molecular weight copolymers are even detected by SEC. As other evidence for the formation of oligomers, a number average molar mass (Mn) of about 510 $g.mol^{-1}$ and a polydispersity index (PDI) of 1.846 were determined as the characteristics of the electropolymerized material using PS standards. Oligomers with chains comprising a few monomer units are thus produced by electropolymerization and the high value of the PDI is consistent with a non-controlled polymerization process.

Formation of oligomers was confirmed by Electrospray Ionization (ESI) mass spectrometry experiments. Mass spectrometry is a powerful technique for characterizing the chemical compositions and the molar mass distributions of polymers while inducing little or no fragmentation when a soft-ionization method such as ESI-MS is used [273]. Elucidation of a polymer structure, characterization of a polymer end-groups and determination of the mass of repeat units can also be achieved.

Table 8 ESI-MS peak-m/z values for the four polymer distributions.

q	1st Distribution				2nd Distribution			3rd Distribution			4th Distribution		
	p				p			p			p		
	1	2	3	4	1	2	3	1	2	3	1	2	3
1	226	370	514	658	254	398	542	268	412	556	284	428	572
2	270	414	558	702	298	442	586	312	456	600	328	472	616
3	314	458	602	746	342	486	630	356	500	644	372	516	660
4	358	502	646	790	386	530	674	400	544	688	416	560	704
5	402	546	690	834	430	574	718	444	588	732	460	604	748
6	446	590	734		474	618	762	488	632	776	504	648	792
7	490	634	778		518	662	806	532	676	820	548	692	836
8	534	678	822		562	706	850	576	720	864	592	736	
9	578	722	866		606	750		620	764		636	780	
10	622	766			650	794		664	808		680	824	
11	666	810			694	838		708			724	868	
12	710	854			738			752			768		
13	754				782			796			812		
14								840					

In the limit of the complexity of the obtained mass spectrum (Figure 61), a large number of oligomeric species led to overlapping peaks. The complexity of the ESI-MS spectrum of the electropolymerized material may also originate from the initial polydispersity of the starting monomer. In the present case, ESI-MS analysis of the commercially avalaible monomer evidenced a broad distribution of monomers comprising at least thirteen different oligomers. Contrary to SEC, ESI-MS also enables to determine the absolute molecular weight and molecular weight distribution. Four distinct ion series were identified in the ESI-MS spectrum as ammonium adducts $[M+NH_4]^+$. The ESI spectrum (Figure 61) was obtained in the positive ion mode and the peak data of the four ion series are given in Table 8. The spacing of 1 Da between ion peaks indicated the presence of only singly charged species.

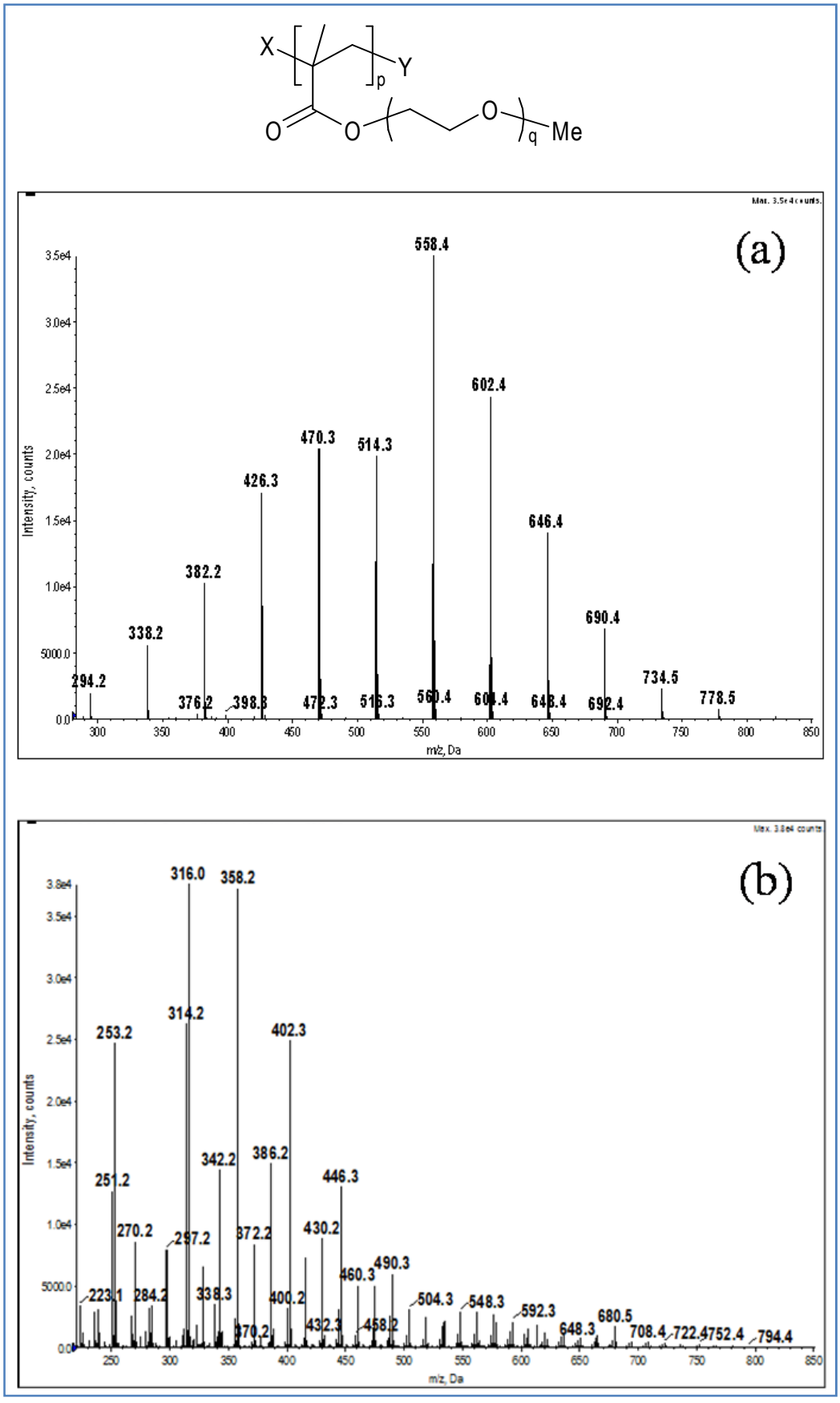

Figure 61 ESI spectrum of (a) monomers and (b) electropolymerized material obtained in the positive ion mode.

Considering the general formula of the electropolymerized material to be $C_{p(2q+5)}H_{p(4q+8)}O_{p(q+2)}XY$, with 'p' representing the number of MMA repeating units, 'q' the length of the ethyleneglycol chain, 'X' and 'Y' the two end-groups, oligomers comprising between 1 to 4 repeating MMA units were detected. However, the presence of higher molecular weight oligomers in the electropolymerized material cannot be excluded, the intensity of the "molecular ion" generally decreasing with increasing oligomer sizes[274]. Due to the dependence of the ionization efficiency on the molecular weight, biased molecular weight distribution could be deduced. Based on the abundance of the mass-to-charge ratios, number average molecular weights (Mn) of 563, 527, 549, and 537 $g.mol^{-1}$ with respective PDI of 1.04, 1.04, 1.03, 1.03 could be determined for the four distributions of oligomers.

Furthermore, X-ray photoelectron spectroscopy (XPS) was carried out to help confirm the incorporation of the lithium salt [LiTFSI: $LiN(SO_2CF_3)_2$] in the polymer deposited on the TiO_2 nanotubes. Figure 62 shows the S2p, F1s and N1s XPS core peaks arising from the $LiN(SO_2CF_3)_2$ in the deposited polymer. A detailed XPS characterization of LiTFSI was previously achieved by Leroy et al.[275]. In their work, the binding energy of N1s core peak is located at 399.6 eV (399.4 eV in this work). The F1s, Li1s and $S2p_{3/2}$ core peaks appear respectively at 688.6, 56.6 and 169.0 eV (688.7 eV, 56.7 eV, 168.8 eV in the present study).

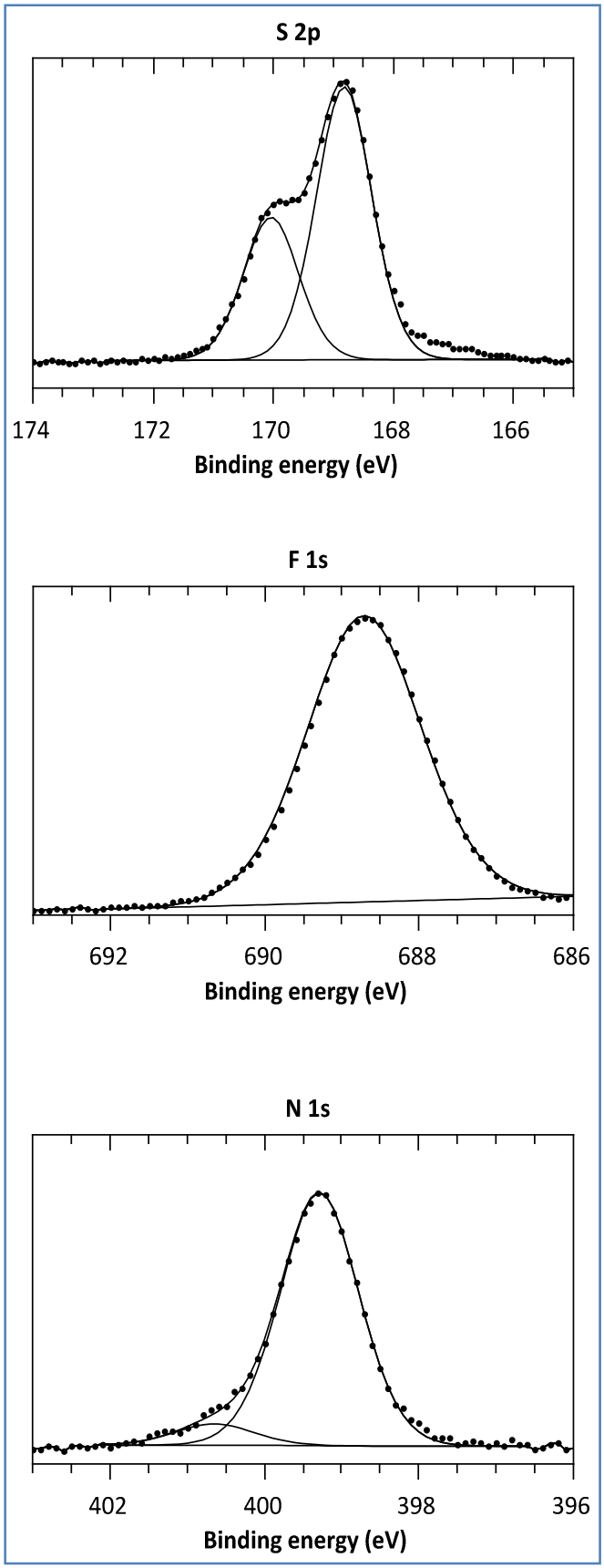

Figure 62 High-resolution S2p, F1s, and N1s XPS core peaks obtained for the copolymer-embedded TiO_2nts.

4.4.2 Electrochemical Behaviour of Polymer-Embedded TiO_2nts

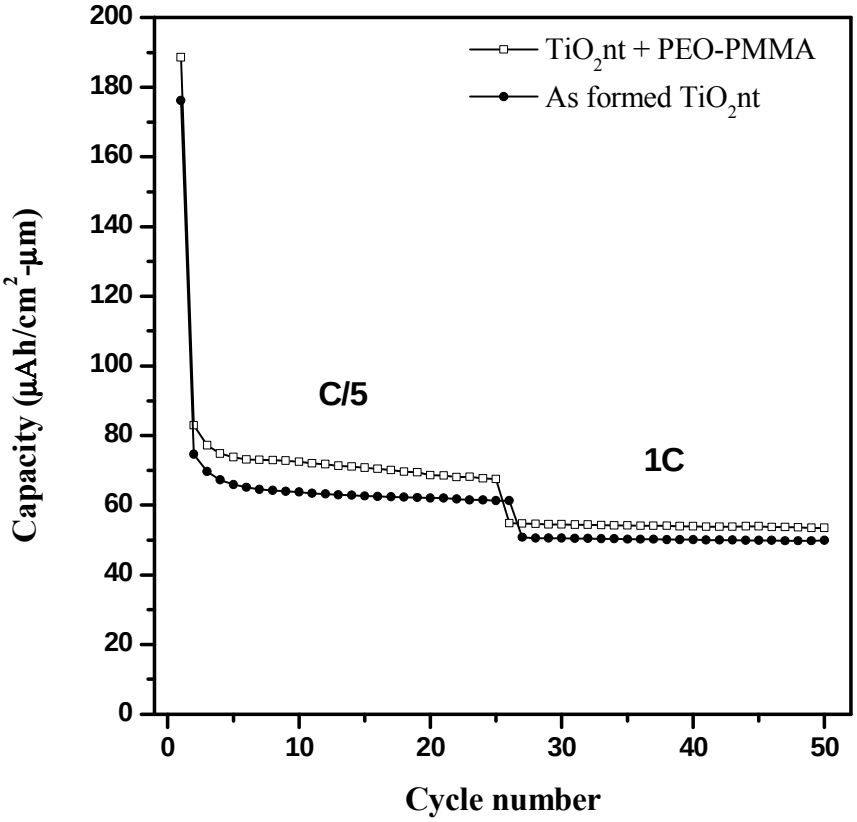

Figure 63 Capacity vs cycle number for the as-formed and copolymer-embeddded TiO_2nts cycled at 1C and C/5 within the $0.05 \leq U/V \leq 2.6$ voltage range and with an $LiPF_6$ [EC:DEC]−soaked separator).

Figure 63 shows the volumic capacity *vs* cycle number for the as-formed TiO_2nts and copolymer-embedded TiO_2nts at two kinetic rates. Due to the gel-like nature of the polymer, no heating was required for the electrochemical studies. The electrochemical performances of the two materials are also summarized in Table 9. In each case, the capacity fading is minimal even with 50 cycles, indicating that the presence of the thin copolymer electrolyte does not have any adverse impact on the lithium storage properties of the TiO_2 nanotubes. Compared to the as-formed TiO_2nts, at current densities of 14 $\mu A/cm^2$ (C/5) and 70 $\mu A/cm^2$ (1C), the copolymer-embedded TiO_2 nanotubes delivered slightly higher (~8%) capacity values.

Table 9 Discharge capacities and efficiencies for as-prepared TiO_2nts and copolymer-embedded TiO_2nts cycled at different rates.

Electrode	Kinetic rate	1st DC[a]	1st RC[b]	IC[c]	50th C[d]	E[e] (%)
TiO_2nt	C/5	176	75	101	60	80
	1C	136	66	70	50	76
TiO_2nt + Copolymer	C/5	189	83	106	65	78
	1C	155	70	85	54	77

[a] Discharge Capacity, [b] Reversible Capacity, [c] Irreversible Capacity, [d] Capacity, [e] Efficiency. All capacities are given in µAh/cm^2-µm.

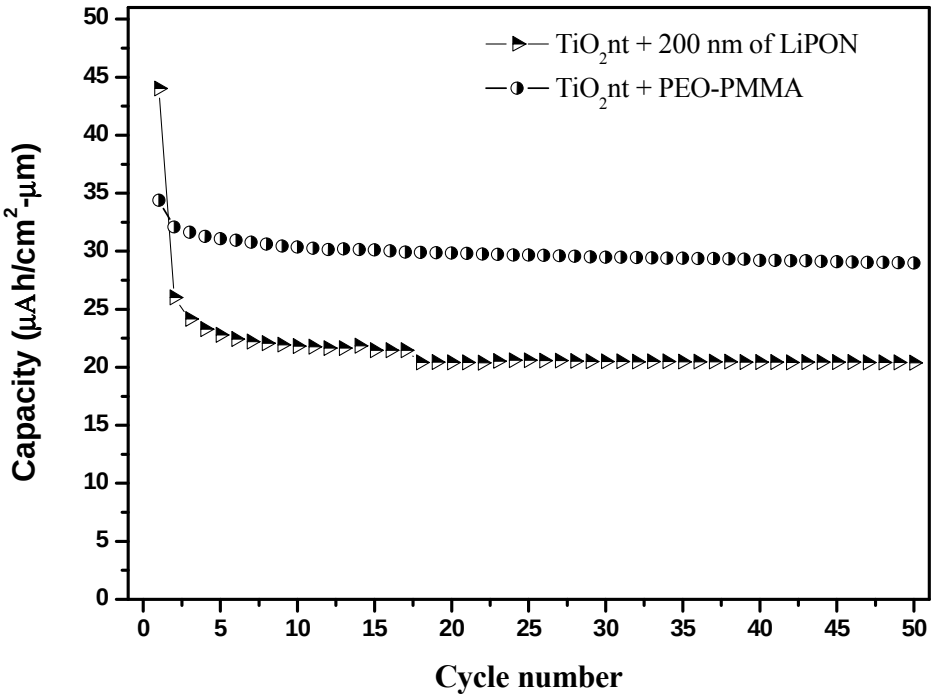

Figure 64 Capacity vs cycle number for copolymer-embedded TiO_2nts and TiO_2nts with 200 nm of LiPON deposit (The cycling was done at j = 350 µA/cm^2 (5C) within the $0.05 \leq U/V \leq 2.6$ voltage range and with an $LiPF_6$ [EC:DEC]−soaked separator).

Moreover, at a current density of 350 µA/cm^2 (5C), the system based on the gel-like copolymer electrolyte delivered much higher capacity values (as shown in Figure 64) in comparison to the system of TiO_2 nanotubes with a layer of LiPON electrolyte (Figure 65). This can be explained by the examination of the as-prepared electrode/solid-electrolyte interfaces. It can be seen from the SEM image shown in Figure 65 that the LiPON deposit covers completely the top of the

nanotubes and does not seem to enter the voids within or between the nanotubes, which otherwise is achievable with the copolymer electrolyte (Figure 55b). It can be asserted that the good performance of the copolymer-embedded TiO_2 nanotubes is not only as a result of the good conductivity of the polymer but also due to an improved electrode/solid-electrolyte interface brought about by the proper filling of the nanotubes.

A highly conformal deposition of the polymer electrolyte onto the as-prepared TiO_2nts has finally been shown to be possible (Figure 66), and the successive deposition of a cathode material is presently being studied for a full 3D design in the near future.

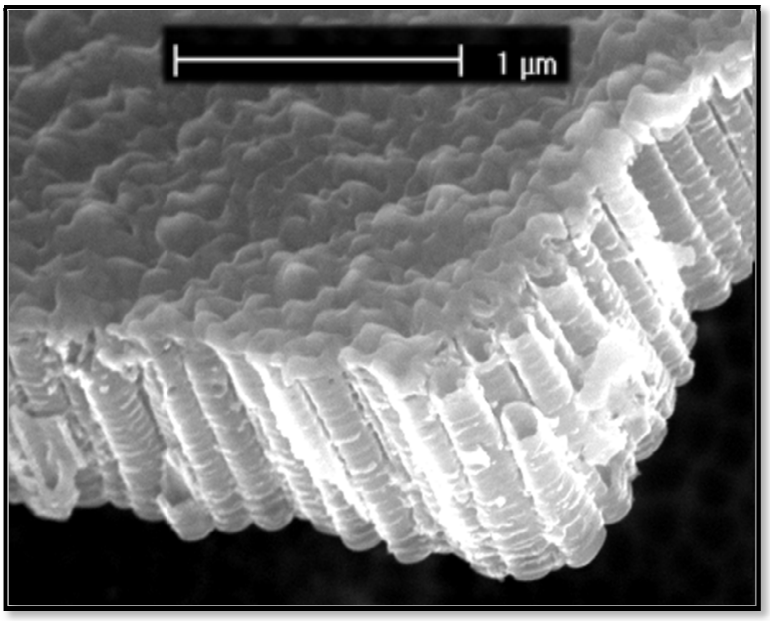

Figure 65 TiO_2nts with a 200 nm LiPON layer deposited by RF−magnetron sputtering.

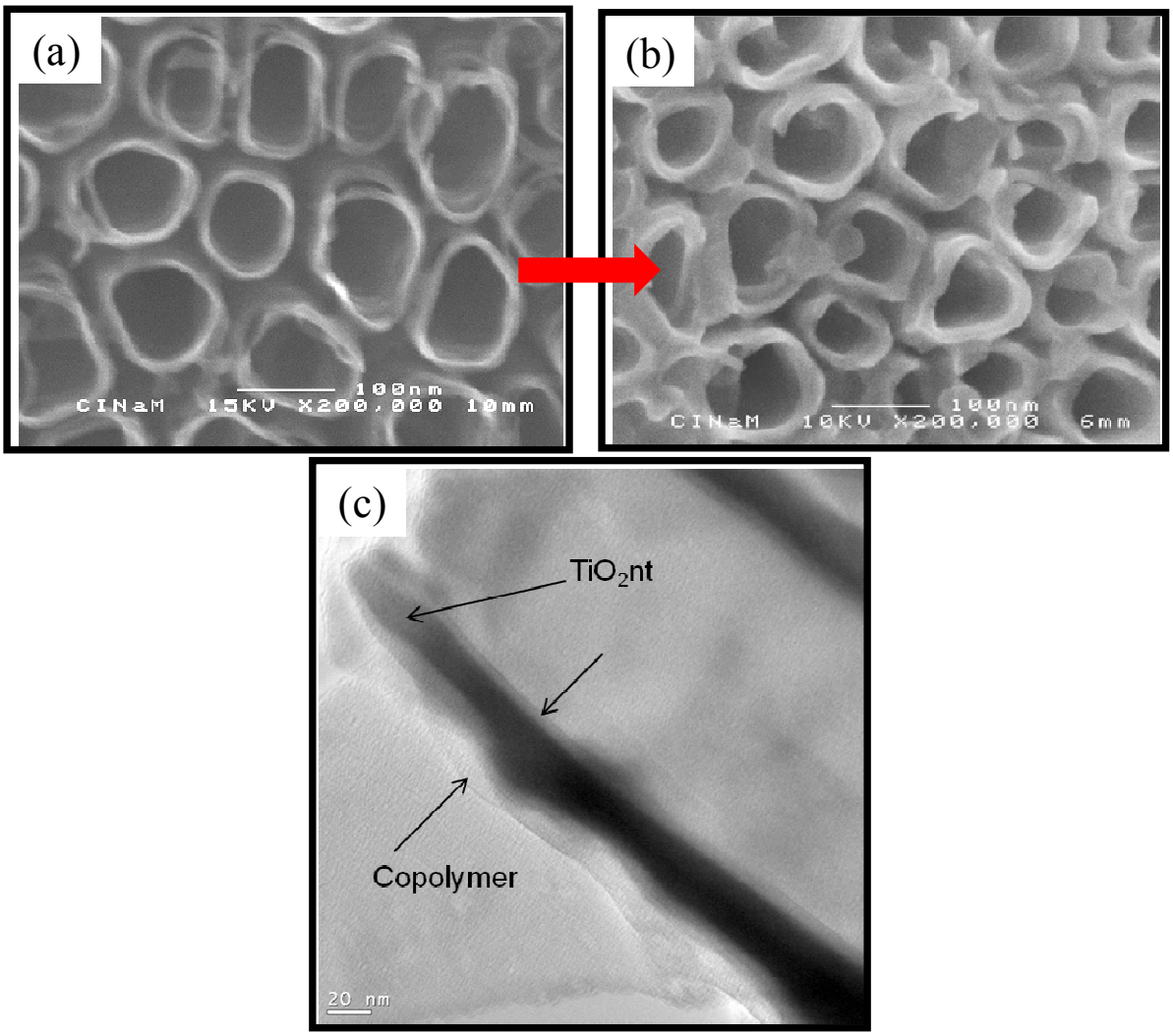

Figure 66 SEM micrographs of as-prepared TiO_2nts (a) and TiO_2nts with a conformally deposited polymer layer (b); and (c) TEM micrograph evidencing the conformally deposited polymer layer.

4.5. Conclusion and Perspectives

The advent of modern microelectronic devices has necessitated the search for high-performance all-solid-state (rechargeable) microbatteries. So far, only lithium-based systems fulfill the voltage and energy density requirements of microbatteries. Presently, there is a need to move from 2D to 3D configurations, and also a necessity to adopt the "Li-ion" or the "rocking-chair" concept in designing these lithium-based (thin-film) microbatteries. This implies the combination of cathode materials such as $LiCoO_2$, $LiMn_2O_4$ or $LiFePO_4$ with the wide range of possible anode materials that can react reversibly with lithium.

Among all the potential anode materials, TiO_2 nanotubes possess a spectacular characteristic for designing 3D Li-ion microbatteries. Besides the self-organized nano-architecture, the use of TiO_2 is ecologically and economically competitive, and the nanotubes have been demonstrated to exhibit very good capacity retention particularly at moderate kinetic rates. The use of TiO_2 as anode also provides cells with low self-discharge and eliminates the risk of overcharging due to its higher operating voltage (ca. 1.72 V vs. Li^+/Li). As TiO_2 (anatase or rutile) effectively inserts only 0.5 Li^+ per formula unit, corresponding to a theoretical capacity of 168 mAh/g, the first part of this study was focussed on improving the overall performance of TiO_2 nanotubes by synthesizing TiO_2 nanotubes and their derivatives, and comparing their electrochemical behaviour in lithium test cells. For derivatives via doping, Fe^{2+} and Sn^{4+} substitution of Ti^{4+} was successfully achieved by anodization of co-sputtered Ti-Fe and Ti-Sn thin films. The Sn-doped TiO_2 nanotubes delivered much higher capacity values in comparison to undoped TiO_2 nanotubes even though Sn was not active within the studied potential window. On the other hand, Fe doping did not improve the electrochemical behaviour of TiO_2 nanotubes, but it is an indication that the doping process can be successfully extended to Sb/Nb-doping of self-supported TiO_2 nanotubes in the search for improved performance. Apart from cationic substitution, anionic substitution of oxygen,

for example carbon doping, is anticipated to also help improve the electrochemical behavior of TiO_2 nanotubes.

For derivatives by designing composites, although the performance was improved with the sub-micron NiO or Co_3O_4 particles, combined current-pulse deposition of nano-sized (10-20 nm) 3d metals and annealing will be a better alternative to decorate the TiO_2nts with conversion materials for an effective 3D design in the near future. Lastly, emphasis was placed on the possibility to employ polymeric films as solid-state Li-ion conductors for the fabrication of 3D Li-ion microbatteries. Gel-like PEO-PMMA copolymer electrolyte was successfully deposited onto the walls of TiO_2 nanotubes by electrodeposition. X-ray photoelectron spectroscopy (XPS) confirmed the incorporation of lithium salt (LiTFSI: $LiN(SO_2CF_3)_2$) into the polymer deposited on the TiO_2 nanotubes, making it a Li-ion conductor. A highly conformal deposition of the polymer electrolyte has indeed been achieved, and the deposition of cathode materials ($LiCoO_2$ or $LiFePO_4$) onto the polymeric layer is anticipated to be achievable with atomic layer deposition for a complete 3D Li-ion microbattery in the near future.

List of Publications

(1) Kyerematenga, N. A.; Vacandio, F.; Sougrati, M. T.; Martinez, H.; Jumas, J. C.; Knauth, P.; Djenizian, T. J. Power Sources 2013, **224**, 269–277.
(2) Kyerematenga, N. A.; Lebouin, C.; Knauth, P.; Djenizian, T. Electrochim. Acta 2013, **88**, 814–820.
(3) Kyerematenga, N. A.; Hornebecq, V.; Martinez, H.; Knauth, P.; Djenizian, T. ChemPhysChem 2012, **13**, 3707–3713.
(4) Kyerematenga, N. A.; Dumur, F.; Knauth, P.; Pecquenard, B.; Djenizian, T. Comptes Rendus Chimie 2012, **In press**.
(5) Plylahan, N.; Kyerematenga, N. A.; Eyraud, M.; Dumur, F.; Martinez, H.; Santinacci, L.; Knauth, P.; Djenizian, T. Nanoscale Research Letters 2012, **7**, 349.
(6) Kyerematenga, N. A.; Hornebecq, V.; Knauth, P.; Djenizian, T. Electrochim. Acta 2012, **62**, 192–198.
(7) Kyerematenga, N. A.; Dumur, F.; Knauth, P.; Pecquenard, B.; Djenizian, T. Electrochem.Commun. 2011, **13**, 894–897.

REFERENCES

1. D. Golodnitsky, V. Yufit, M. Nathan, I. Shechtman, T. Ripenbein, E. Strauss, S. Menkina and E. Peled, *J. Power Sources*, 2006, **153**, 281–287.
2. J. B. Bates, N. J. Dudney, B. J. Neudecker, F. X. Hart, H. P. Jun and S. A. Hackney, *Journal of Electrochemical Society*, 2000, **147**, 59.
3. K. Kanehori, K. Matsumoto, K. Miyauchi and T. Kudo, *Solid State Ionics*, 1983, **1445**, 9/10.
4. M. Balkanski, *Sol. Energy Mater. Sol. Cells*, 2000, **62**, 21-35.
5. P. J. Gellings and H. J. M. Bouwmeester, eds., *The CRC Handbook of Solidstate Electrochemistry*, CRC press, Inc., Florida, USA, 1997.
6. L. Jourdaine, J. L. Souquet, V. Delord and M. Ribes, *Solid State Ionics*, 1988, **28**, 1490-1494.
7. K. John H, *Thin Solid Films*, 1977, **43**, 41-92.
8. P. Vouros and J. I. Masters, *J. Electrochem. Soc.*, 1969, **116**, 880-884.
9. S. Chandra, R. C. Agrawal and R. K. Pandey, *National Academy Science Letters-India*, 1978, **1**, 112-114.
10. S. Sekido and Y. Ninomiya, *Solid State Ionics*, 1981, **3-4**, 153-156.
11. C. C. Liang, J. Epstein and G. H. Boyle, *J. Electrochem. Soc.*, 1969, **116**, 1452-1454.
12. C. C. Liang and P. Bro, *J. Electrochem. Soc.*, 1969, **116**, 1322-1323.
13. M. S. Whittingham and F. R. Gamble, *Mater. Res. Bull.*, 1975, **10**, 363-371.
14. K. Kanehori, K. Matsumoto, K. Miyauchi and T. Kudo, *Solid State Ionics*, 1983, **9-10, Part 2**, 1445-1448.
15. G. Meunier, R. Dormoy and A. Levasseur, *Materials Science and Engineering B-Solid State Materials for Advanced Technology*, 1989, **3**, 19-23.
16. S. D. Jones and J. R. Akridge, *Solid State Ionics*, 1992, **53-56, Part 1**, 628-634.

17. M. Balkanski, C. Julien and J. Y. Emery, *J. Power Sources*, 1989, **26**, 615-622.
18. C. Julien, A. Khelfa, N. Benramdane, J. P. Guesdon, P. Dzwonkowski, I. Samaras and M. Balkanski, *Mater. Sci. Eng., B*, 1994, **23**, 105-115.
19. C. Julien, L. El-Farh, M. Balkanski, O. M. Hussain and G. A. Nazri, *Appl. Surf. Sci.*, 1993, **65-66**, 325-330.
20. H. Ohtsuka, S. Okada and J. Yamaki, *Solid State Ionics*, 1990, **40-1**, 964-966.
21. E. J. Plichta, W. K. Behl, D. Vujic, W. H. S. Chang and D. M. Schleich, *J. Electrochem. Soc.*, 1992, **139**, 1509-1513.
22. J. B. Bates, N. J. Dudney, G. R. Gruzalski, R. A. Zuhr, A. Choudhury, C. F. Luck and J. D. Robertson, *J. Power Sources*, 1993, **43**, 103-110.
23. J. B. Bates, G. R. Gruzalski, N. J. Dudney, C. F. Luck, X. H. Yu and S. D. Jones, *Solid State Technology*, 1993, **36**, 59-&.
24. W. Lai, C. K. Erdonmez, T. F. Marinis, C. K. Bjune, N. J. Dudney, F. Xu, R. Wartena and Y. M. Chiang, *Adv. Mater.*, 2010, **22**, E139.
25. J. B. Bates, N. J. Dudney, B. Neudecker, A. Ueda and C. D. Evans, *Solid State Ionics*, 2000, **135**, 33-45.
26. B. Warneke, M. Last, B. Liebowitz and K. S. J. Pister, *Computer*, 2001, **34**, 44-+.
27. L. Baggetto, R. A. H. Niessen, F. Roozeboom and P. H. L. Notten, *Adv. Funct. Mater.*, 2008, **18**, 1057-1066.
28. P. H. L. Notten, F. Roozeboom, R. A. H. Niessen and L. Baggetto, *Adv. Mater.*, 2007, **19**, 4564-4567.
29. R. W. Hart, H. S. White, B. Dunn and D. R. Rolison, *Electrochem. Commun.*, 2003, **5**, 120-123.
30. J. F. M. Oudenhoven, L. Baggetto and P. H. L. Notten, *Advanced Energy Materials*, **1**, 10-33.
31. J. W. Long, B. Dunn, D. R. Rolison and H. S. White, *Chem. Rev.*, 2004, **104**, 4463-4492.
32. L. Bazin, S. Mitra, P. L. Taberna, P. Poizot, M. Gressier, M. J. Menu, A. Barnabé, P. Simon and J. M. Tarascon, *J. Power Sources*, 2009, **188**, 578-582.
33. M. Nathan, D. Golodnitsky, V. Yufit, E. Strauss, T. Ripenbein, I. Shechtman, S. Menkin and E. Peled, *Journal of Microelectromechanical Systems*, 2005, **14**, 879-885.
34. D. Golodnitsky, M. Nathan, V. Yufit, E. Strauss, K. Freedman, L. Burstein, A. Gladkich and E. Peled, *Solid State Ionics*, 2006, **177**, 2811-2819.
35. A. V. Jeyaseelan and J. F. Rohan, *Appl. Surf. Sci.*, 2009, **256**, S61-S64.
36. H.-S. Min, B. Y. Park, L. Taherabadi, C. Wang, Y. Yeh, R. Zaouk, M. J. Madou and B. Dunn, *J. Power Sources*, 2008, **178**, 795-800.
37. C. Lethien, M. Zegaoui, P. Roussel, P. Tilmant, N. Rolland and P. A. Rolland, *Microelectronic Engineering*, **88**, 3172-3177.
38. K. Yoshima, H. Munakata and K. Kanamura, *J. Power Sources*, **208**, 404-408.
39. Y. J. Park, K. S. Park, J. G. Kim, M. K. Kim, H. G. Kim and H. T. Chung, *J. Power Sources*, 2000, **88**, 250-254.
40. M. Kotobuki, Y. Suzuki, H. Munakata, K. Kanamura, Y. Sato, K. Yamamotob and T. Yoshida, *J. Power Sources*, 2010, **195**, 5784-5788.
41. Z. G. Lu, H. Cheng, M. F. Lo and C. Y. Chung, *Adv. Funct. Mater.*, 2007, **17**, 3885-3896.
42. G. F. Ortiz, I. Hanzu, P. Knauth, P. Lavela, J. L. Tirado and T. Djenizian, *Electrochim. Acta*, 2009, **54** 4262-4268.
43. G. F. Ortiz, I. Hanzu, T. Djenizian, P. Lavela, J. L. Tirado and P. Knauth, *Chem. Mater.*, 2009, **21**, 63-67.

44. N. A. Kyerematen, F. Dumur, P. Knauth, B. Pecquenard and T. Djenizian, *Electrochem. Commun.*, 2011, **13**, 894-897.
45. G. F. Ortiz, I. Hanzu, P. Lavela, P. Knauth, J. L. Tirado and T. Djenizian, *Chem. Mater.*, 2010, **22**, 1926-1932.
46. G. F. Ortiz, I. Hanzu, P. Knauth, P. Lavela, J. L. Tirado and T. Djenizian, *Electrochemical and Solid State Letters*, 2009, **12**, A186-A189.
47. P. Poizot, S. Laruelle, S. Grugeon, L. Dupont and J. M. Tarascon, *Nature*, 2000, **407**, 496-499.
48. L. Taberna, S. Mitra, P. Poizot, P. Simon and J. M. Tarascon, *Nat. Mater.*, 2006, **5**, 567-573.
49. P. Lavela, N. A. Kyerematen and J. L. Tirado, *Mater. Chem. Phys.*, 2010 **124**, 102-108.
50. C. Vidal-Abarca, P. Lavela and J. L. Tirado, *Electrochemical and Solid State Letters*, 2008, **11**, A198-A201.
51. C. Navone, J. P. Pereira-Ramos, R. Baddour-Hadjean and R. Salot, *J. Electrochem. Soc.*, 2006, **153**, A2287-A2293.
52. A. Gies, B. Pecquenard, A. Benayad, H. Martinez, D. Gonbeau, H. Fuess and A. Levasseur, *Thin Solid Films*, 2008, **516**, 7271-7281.
53. B. Fleutot, B. Pecquenard, F. Le Cras, B. Delis, H. Martinez, L. Dupont and D. Guy-Bouyssou, *J. Power Sources*, 2011, **196**, 10289-10296.
54. M. Roberts, P. Johns, J. Owen, D. Brandell, K. Edstrom, G. El Enany, C. Guery, D. Golodnitsky, M. Lacey, C. Lecoeur, H. Mazor, E. Peled, E. Perre, M. M. Shaijumon, P. Simon and P. L. Taberna, *J. Mater. Chem.*, 2011, **21**, 9876-9890.
55. T. Djenizian, I. Hanzu and P. Knauth, *J. Mater. Chem.*, 2011, **21**, 9925-9937.
56. P. Kubiak, M. Pfanzelt, J. Geserick, U. Hörmann, N. Hüsing, U. Kaiser and M. Wohlfahrt-Mehrens, *J. Power Sources*, 2009, **194**, 1099-1104.
57. T. Brousse, P.-L. Taberna, O. Crosnier, R. Dugas, P. Guillemet, Y. Scudeller, Y. Zhou, F. Favier, D. Belanger and P. Simon, *J. Power Sources*, 2007, **173**, 633-641.
58. E. Machefaux, T. Brousse, D. Belanger and D. Guyomard, *J. Power Sources*, 2007, **165**, 651-655.
59. D. Linden and T. B. Reddy, McGraw-Hill Companies, New York, US., 2001.
60. H. A. Kiehne, (2003) *Battery Technology Handbook*, 2ed illustrated, CRC Press, available from: Google books online http://books.google.com> [Accessed 22nd March 2009].
61. M. S. Whittingham, *Progress in Solid State Chemistry*, 1978, **12**, 41-99.
62. M. S. Whittingham, *J. Solid State Chem.*, 1979, **29**, 303-310.
63. M. S. Whittingham, *Science*, 1976, **192**, 1126-1127.
64. J. Broadhead, F. J. DiSalvo and F. A. Trumbore, 1975, **Pat. US3864167**.
65. J. Broadhead and A. D. Butherus, 1974, **Pat. US3791867**.
66. M. Zanini, S. Basu and J. E. Fischer, *Carbon*, 1978, **16**, 211-212.
67. S. Basu, C. Zeller, P. J. Flanders, C. D. Fuerst, W. D. Johnson and J. E. Fischer, *Materials Science and Engineering*, 1979, **38**, 275-283.
68. R. Yazami and P. Touzain, *J. Power Sources*, 1983, **9**, 365-371.
69. J. O. Besenhard and R. Schollhorn, *J. Electrochem. Soc.*, 1977, **124**, 968-971.
70. J. O. Besenhard and R. Schollhorn, *J. Power Sources*, 1977, **1**, 267-276.
71. J. O. Besenhard, *Carbon*, 1976, **14**, 111-115.
72. J. O. Besenhard and G. Eichinger, *J. Electroanal. Chem.*, 1976, **68**, 1-18.
73. G. Eichinger and J. O. Besenhard, *J. Electroanal. Chem.*, 1976, **72**, 1-31.
74. D. W. Murphy, F. J. Di Salvo, J. N. Carides and J. V. Waszczak, *Mater. Res. Bull.*, 1978, **13**, 1395-1402.

75. M. Lazzari and B. Scrosati, *J. Electrochem. Soc.*, 1980, **127**, 773-774.
76. S. Basu, 1981, **Pat. US4304825**.
77. K. Mizushima, P. C. Jones, P. J. Wiseman and J. B. Goodenough, *Mater. Res. Bull.*, 1980, **15**, 783-789.
78. M. M. Thackeray, W. I. F. David, P. G. Bruce and J. B. Goodenough, *Mater. Res. Bull.*, 1983, **18**, 461-472.
79. A. Yoshino, K. Sanechika and T. Nakajima, 1987, **Pat. US4668595**.
80. T. Nagaura and K. Tozawa, *Prog. Batteries Solar Cells*, 1990, **9**, 209.
81. W. V. Schalkwijk and B. Scrosati, eds., *Advances in Lithium-Ion Batteries*, Kluwer Academic/Plenum Publishers, New York., 2002.
82. L. Kavan, M. GrÃ¤tzel, S. E. Gilbert, C. Klemenz and H. J. Scheel, *Journal of the American Chemical Society*, 1996, **118**, 6716-6723.
83. J. Tang and S. Endo, *J. Am. Ceram. Soc.*, 1993, **76**, 796-798.
84. M. Latroche, L. Brohan, R. Marchand and M. Tournoux, *J. Solid State Chem.*, 1989, **81**, 78-82.
85. J. Akimoto, Y. Gotoh, Y. Oosawa, N. Nonose, T. Kumagai, K. Aoki and H. Takei, *J. Solid State Chem.*, 1994, **113**, 27-36.
86. R. Marchand, L. Brohan and M. Tournoux, *Mater. Res. Bull.*, 1980, **15**, 1129-1133.
87. J. F. Banfield, D. R. Veblen and D. J. Smith, *American Mineralogist*, 1991, **76**, 343-353.
88. M. Dondi, G. Cruciani, G. Guarini, F. Matteucci and M. Raimondo, *Ceramics International*, 2006, **32**, 393-405.
89. N. Serpone, D. Dondi and A. Albini, *Inorg. Chim. Acta*, 2007, **360**, 794-802.
90. A. Fujishima and K. Honda, *Nature*, 1972, **238**, 37-38.
91. A. Fujishima, T. N. Rao and D. A. Tryk, *Journal of Photochemistry and Photobiology C: Photochemistry Reviews*, 2000, **1**, 1-21.
92. T. Inoue, A. Fujishima, S. Konishi and K. Honda, *Nature*, 1979, **277**, 637-638.
93. S. J. Bao, C. M. Li, J. F. Zang, X. Q. Cui, Y. Qiao and J. Guo, *Adv. Funct. Mater.*, 2008, **18**, 591-599.
94. A. Ghicov, M. Yamamoto and P. Schmuki, *Angew. Chem. Int. Ed.*, 2008, **47**, 7934-7937.
95. D. Cummins, G. Boschloo, M. Ryan, D. Corr, S. N. Rao and D. Fitzmaurice, *The Journal of Physical Chemistry B*, 2000, **104**, 11449-11459.
96. B. Oregan and M. Gratzel, *Nature*, 1991, **353**, 737-740.
97. A. K. Chandiran, F. Sauvage, M. Casas-Cabanas, P. Comte, S. M. Zakeeruddin and M. Graetzel, *J. Phys. Chem. C*, 2010, **114**, 15849-15856.
98. S. Y. Huang, L. Kavan, I. Exnar and M. Gratzel, *J. Electrochem. Soc.*, 1995, **142**, L142-L144.
99. L. Aldon, P. Kubiak, A. Picard, J. C. Jumas and J. Olivier-Fourcade, *Chem. Mater.*, 2006, **18**, 1401-1406.
100. I. Hanzu, T. Djenizian and P. Knauth, *J. Phys. Chem. C*, 2011, **115**, 5989-5996.
101. P. Roy, S. Berger and P. Schmuki, *Angew. Chem. Int. Ed.*, 2011, **50**, 2904-2939.
102. F. R. Cummings, L. J. Le Roux, M. K. Mathe and D. Knoesen, *Mater. Chem. Phys.*, 2010, **124**, 234-242.
103. K. Madhusudan Reddy, S. V. Manorama and A. Ramachandra Reddy, *Mater. Chem. Phys.*, 2002, **78**, 239-245.
104. R. Zallen and M. P. Moret, *Solid State Commun.*, 2006, **137**, 154-157.
105. M. V. Thournout, Université Montpellier II, **Montpellier**, **FRANCE**, **2006**, p. 192.
106. U. Müller, *Inorganic structural chemistry*, Wiley, 2006.
107. S. Iijima, *Nature*, 1991, **354**, 56-58.

108. G. K. Mor, O. K. Varghese, M. Paulose, K. Shankar and C. A. Grimes, *Sol. Energy Mater. Sol. Cells*, 2006, **90**, 2011-2075.
109. J. M. Macak, H. Tsuchiya, A. Ghicov, K. Yasuda, R. Hahn, S. Bauer and P. Schmuki, *Curr. Opin. Solid State Mater. Sci.*, 2007, **11** 3-18.
110. P. Hoyer, *Langmuir*, 1996, **12**, 1411-1413.
111. H. J. Shin, D. K. Jeong, J. G. Lee, M. M. Sung and J. Y. Kim, *Adv. Mater.*, 2004, **16**, 1197-+.
112. T. Kasuga, M. Hiramatsu, A. Hoson, T. Sekino and K. Niihara, *Langmuir*, 1998, **14**, 3160-3163.
113. T. Kasuga, M. Hiramatsu, A. Hoson, T. Sekino and K. Niihara, *Adv. Mater.*, 1999, **11**, 1307-+.
114. J. J. Kelly, *Electrochim. Acta*, 1979, **24**, 1273-1282.
115. V. Zwilling, E. Darque-Ceretti, A. Boutry-Forveille, D. David, M. Y. Perrin and M. Aucouturier, *Surf. Interface anal.*, 1999, **27**, 629-637.
116. V. Zwilling, M. Aucouturier and E. Darque-Ceretti, *Electrochim. Acta*, 1999, **45**, 921-929.
117. D. Gong, C. A. Grimes, O. K. Varghese, W. C. Hu, R. S. Singh, Z. Chen and E. C. Dickey, *J. Mater. Res.*, 2001, **16**, 3331-3334.
118. R. Beranek, H. Hildebrand and P. Schmuki, *Electrochem. Solid St.*, 2003, **6**, B12-B14.
119. A. Ghicov, H. Tsuchiya, J. M. Macak and P. Schmuki, *Electrochem. Commun.*, 2005, **7**, 505-509.
120. Y. D. Premchand, T. Djenizian, F. Vacandio and P. Knauth, *Electrochem. Commun.*, 2006, **8**, 1840-1844.
121. G. F. Ortiz, I. Hanzu, P. Lavela, J. L. Tirado, P. Knauth and T. Djenizian, *J. Mater. Chem.*, 2010, **20**, 4041-4046.
122. M. Paulose, K. Shankar, O. K. Varghese, G. K. Mor and C. A. Grimes, *Journal of Physics D: Applied Physics*, 2006, **39**, 2498.
123. M. Paulose, K. Shankar, O. K. Varghese, G. K. Mor, B. Hardin and C. A. Grimes, *Nanotechnology*, 2006, **17**, 1446.
124. M. Paulose, O. K. Varghese, G. K. Mor, C. A. Grimes and K. G. Ong, *Nanotechnology*, 2006, **17**, 398.
125. J. M. Macak, P. J. Barczuk, H. Tsuchiya, M. Z. Nowakowska, A. Ghicov, M. Chojak, S. Bauer, S. Virtanen, P. J. Kulesza and P. Schmuki, *Electrochem. Commun.*, 2005, **7**, 1417-1422.
126. G. C. Wood and J. P. O'Sullivan, *Electrochim. Acta*, 1970, **15**, 1865-1876.
127. G. Patermarakis and H. S. Karayannis, *Electrochim. Acta*, 1995, **40**, 2647-2656.
128. A. P. Li, F. Muller, A. Birner, K. Nielsch and U. Gosele, *J. Appl. Phys.*, 1998, **84**, 6023-6026.
129. V. P. Parkhutik and V. I. Shershulsky, *Journal of Physics D-Applied Physics*, 1992, **25**, 1258-1263.
130. J. L. Delplancke and R. Winand, *Electrochim. Acta*, 1988, **33**, 1551-1559.
131. D. D. Macdonald, *J. Electrochem. Soc.*, 1993, **140**, L27-L30.
132. J. Siejka and C. Ortega, *J. Electrochem. Soc.*, 1977, **124**, 883-891.
133. G. E. Thompson, *Thin Solid Films*, 1997, **297**, 192-201.
134. S. Berger, S. P. Albu, F. Schmidt-Stein, H. Hildebrand, P. Schmuki, J. S. Hammond, D. F. Paul and S. Reichlmaier, *Surf. Sci.*, 2011, **605**, L57-L60.
135. S. Hrapovic, B. L. Luan, M. D'Amours, G. Vatankhah and G. Jerkiewicz, *Langmuir*, 2001, **17**, 3051-3060.
136. H. Habazaki, K. Fushimi, K. Shimizu, P. Skeldon and G. E. Thompson, *Electrochem. Commun.*, 2007, **9**, 1222-1227.

137. S. P. Albu, A. Ghicov, S. Aldabergenova, P. Drechsel, D. LeClere, G. E. Thompson, J. M. Macak and P. Schmuki, *Adv. Mater.*, 2008, **20**, 4135-4139.
138. S. J. Garcia-Vergara, P. Skeldon, G. E. Thompson and H. Habazaki, *Electrochim. Acta*, 2006, **52**, 681-687.
139. P. Skeldon, G. E. Thompson, S. J. Garcia-Vergara, L. Iglesias-Rubianes and C. E. Blanco-Pinzon, *Electrochemical and Solid State Letters*, 2006, **9**, B47-B51.
140. K. R. Hebert and J. E. Houser, *J. Electrochem. Soc.*, 2009, **156**, C275-C281.
141. J. E. Houser and K. R. Hebert, *Nat. Mater.*, 2009, **8**, 415-420.
142. J. M. Macak, H. Tsuchiya, L. Taveira, S. Aldabergerova and P. Schmuki, *Angew. Chem. Int. Ed.*, 2005, **44**, 7463-7465.
143. Y.-Y. Song and P. Schmuki, *Electrochem. Commun.*, 2010, **12**, 579-582.
144. A. Valota, D. J. LeClere, P. Skeldon, M. Curioni, T. Hashimoto, S. Berger, J. Kunze, P. Schmuki and G. E. Thompson, *Electrochim. Acta*, 2009, **54**, 4321-4327.
145. J. M. Macak, H. Tsuchiya and P. Schmuki, *Angew. Chem. Int. Ed.*, 2005, **44**, 2100-2102.
146. J. M. Macak and P. Schmuki, *Electrochim. Acta*, 2006, **52**, 1258-1264.
147. L. V. Taveira, J. M. Macak, K. Sirotna, L. F. P. Dick and P. Schmuki, *J. Electrochem. Soc.*, 2006, **153**, B137-B143.
148. W. Chanmanee, A. Watcharenwong, C. R. Chenthamarakshan, P. Kajitvichyanukul, N. R. de Tacconi and K. Rajeshwar, *Journal of the American Chemical Society*, 2007, **130**, 965-974.
149. S. Banerjee, S. K. Mohapatra, M. Misra and I. B. Mishra, *Nanotechnology*, 2009, **20**.
150. S. Berger, F. Jakubka and P. Schmuki, *Electrochem. Commun.*, 2008, **10**, 1916-1919.
151. F. Vacandio, M. Eyraud, C. Chassigneux, P. Knauth and T. Djenizian, *J. Electrochem. Soc.*, 2010, **157**, K279-K283.
152. S. Berger, F. Jakubka and P. Schmuki, *Electrochem. Solid St.*, 2009, **12**, K45-K48.
153. H. Tsuchiya and P. Schmuki, *Electrochem. Commun.*, 2005, **7**, 49-52.
154. R. Hahn, J. M. Macak and P. Schmuki, *Electrochem. Commun.*, 2007, **9**, 947-952.
155. A. Ghicov, S. Aldabergenova, H. Tsuchyia and P. Schmuki, *Angew. Chem. Int. Ed.*, 2006, **45**, 6993-6996.
156. W. Wei, K. Lee, S. Shaw and P. Schmuki, *Chem. Commun.*, **48**, 4244-4246.
157. W. Wei, J. M. Macak and P. Schmuki, *Electrochem. Commun.*, 2008, **10**, 428-432.
158. Wei, J. M. Macak, N. K. Shrestha and P. Schmuki, *J. Electrochem. Soc.*, 2009, **156**, K104-K109.
159. K. Lee and P. Schmuki, *Electrochem. Commun.*, **13**, 542-545.
160. Y. Yang, S. P. Albu, D. Kim and P. Schmuki, *Angew. Chem. Int. Ed.*, **50**, 9071-9075.
161. Y. Yang, D. Kim, M. Yang and P. Schmuki, *Chem. Commun.*, **47**, 7746-7748.
162. T. J. LaTempa, X. Feng, M. Paulose and C. A. Grimes, *J. Phys. Chem. C*, 2009, **113**, 16293-16298.
163. G. K. Mor, H. E. Prakasam, O. K. Varghese, K. Shankar and C. A. Grimes, *Nano Lett.*, 2007, **7**, 2356-2364.
164. R. Qin, D. Y. Ding, C. Q. Ning, H. G. Liu, B. S. Zhu, M. Li and D. L. Mao, *Appl. Surf. Sci.*, **257**, 6308-6313.
165. M. C. Turhan, R. P. Lynch, H. Jha, P. Schmuki and S. Virtanen, *Electrochem. Commun.*, 2010, **12**, 796-799.
166. J. H. Jeun and S. H. Hong, *Sensors and Actuators B-Chemical*, 2010, **151**, 1-7.
167. C.-Y. Kuo, K.-H. Huang and S.-Y. Lu, *Electrochem. Commun.*, 2007, **9**, 2867-2870.
168. A. Hossain, G. W. Yang, M. Parameswaran, J. R. Jennings and Q. Wang, *Journal of Physical Chemistry C*, 2010, **114**, 21878-21884.
169. H. C. Shin, J. Dong and M. Liu, *Adv. Mater.*, 2004, **16**, 237-240.

170. G. F. Ortiz, P. Lavela, P. Knauth, T. Djenizian, R. Alcantara and J. L. Tirado, *J. Electrochem. Soc.*, 2011, **158**, A1094-A1099.
171. T. Djenizian, I. Hanzu, Y. D. Premchand, F. Vacandio and P. Knauth, *Nanotechnology*, 2008, **19**, 205601.
172. A. Weibel, R. Bouchet, S. L. P. Savin, A. V. Chadwick, P. E. Lippens, M. Womes and P. Knauth, *ChemPhysChem*, 2006, **7**, 2377-2383.
173. F. Fresno, D. Tudela, J. M. Coronado and J. Soria, *Catal. Today*, 2009, **143**, 230-236.
174. M. G. Faba, D. Gonbeau and G. Pfisterguillouzo, *J. Electron. Spectrosc.*, 1995, **73**, 65-80.
175. J.-C. Dupin, D. Gonbeau, P. Vinatier and A. Levasseur, *Phys. Chem. Chem. Phys.*, 2000, **2**, 1319-1324.
176. C. Guimon, A. Gervasini and A. Auroux, *J. Phys. Chem. B*, 2001, **105**, 10316-10325.
177. A. R. Gonzalezelipe, G. Munuera, J. P. Espinos and J. M. Sanz, *Surf. Sci.*, 1989, **220**, 368-380.
178. M. C. Biesinger, L. W. M. Lau, A. R. Gerson and R. S. C. Smart, *Appl. Surf. Sci.*, 2010, **257**, 887-898.
179. J. C. Parlebas, M. A. Khan, T. Uozumi, K. Okada and A. Kotani, *J. Electron. Spectrosc.*, 1995, **71**, 117-139.
180. J. L. Guimaraes, M. Abbate, S. B. Betim and M. C. M. Alves, *J. Alloys Compd.*, 2003, **352**, 16-20.
181. D. K. G. Deboer, C. Haas and G. A. Sawatzky, *Phys. Rev. B*, 1984, **29**, 4401-4419.
182. I. Pollini, A. Mosser and J. C. Parlebas, *Phys. Rep.*, 2001, **355**, 1-72.
183. A. E. Bocquet, T. Mizokawa, K. Morikawa, A. Fujimori, S. R. Barman, K. Maiti, D. D. Sarma, Y. Tokura and M. Onoda, *Phys. Rev. B*, 1996, **53**, 1161-1170.
184. X. J. Zhu, Z. P. Guo, P. Zhang, G. D. Du, C. K. Poh, Z. X. Chen, S. Li and H. K. Liu, *Electrochim. Acta*, 2010, **55**, 4982-4986.
185. X. Zhou, W. Fu, H. Yang, D. Ma, J. Cao, Y. Leng, J. Guo, Y. Zhang, Y. Sui, W. Zhao and M. Li, *Mater. Chem. Phys.*, 2010, **124**, 614-618.
186. J. W. O'Brien, R. A. Dunlap and J. R. Dahn, *J. Alloys Compd.*, 2003, **353**, 60-64.
187. J. W. O'Brien, R. A. Dunlap and J. R. Dahn, *J. Alloys Compd.*, 2003, **353**, 65-73.
188. B. Grzeta, E. Tkalcec, C. Goebbert, M. Takeda, M. Takahashi, K. Nomura and M. Jaksic, *J. Phys. Chem. Solids*, 2002, **63**, 765-772.
189. V. S. Urusov, D. A. Khramov and K. Langer, *European Journal of Mineralogy*, 1999, **11**, 295-298.
190. I. Issac, M. Scheuermann, S. M. Becker, E. G. Bardaji, C. Adelhelm, D. Wang, C. Kuebel and S. Indris, *J. Power Sources*, 2011, **196**, 9689-9695.
191. L. V. Taveira, A. A. Saguees, J. M. Macak and P. Schmuki, *J. Electrochem. Soc.*, 2008, **155**, C293-C302.
192. I. Hanzu, T. Djenizian, G. F. Ortiz and P. Knauth, *J. Phys. Chem. C*, 2009, **113**, 20568-20575.
193. M. Pfanzelt, P. Kubiak, M. Fleischhammer and M. Wohlfahrt-Mehrens, *J. Power Sources*, 2011, **196**, 6815-6821.
194. W. J. Macklin and R. J. Neat, *Solid State Ionics*, 1992, **53-56**, 694-700.
195. K. Zhu, Q. Wang, J.-H. Kim, A. A. Pesaran and A. J. Frank, *J. Phys. Chem. C*, 2012, **116**, 11895-11899.
196. N. A. Kyerematen, V. Hornebecq, P. Knauth and T. Djenizian, *Electrochim. Acta*, 2012, **62**, 192-198.
197. H. Uchiyama, E. Hosono, H. Zhou and H. Imai, *Solid State Ionics*, 2009, **180**, 956-960.

198. S. Dong, H. Wang, L. Gu, X. Zhou, Z. Liu, P. Han, Y. Wang, X. Chen, G. Cui and L. Chen, *Thin Solid Films*, 2011, **519**, 5978-5982.
199. J. S. Chen and X. W. Lou, *J. Power Sources*, 2010, **195**, 2905-2908.
200. M. J. Aragon, B. Leon, T. Serrano, C. P. Vicente and J. L. Tirado, *J. Mater. Chem.*, 2011, **21**, 10102-10107.
201. H. E. Prakasam, O. K. Varghese, M. Paulose, G. K. Mor and C. A. Grimes, *Nanotechnology*, 2006, **17**, 4285-4291.
202. R. R. Rangaraju, K. S. Raja, A. Panday and M. Misra, *Electrochim. Acta*, **55**, 785-793.
203. A. P. Singh, S. Kumari, R. Shrivastav, S. Dass and V. R. Satsangi, *Int. J. Hydrogen. Energ.*, 2008, **33**, 5363-5368.
204. G. Bhargava, I. Gouzman, C. M. Chun, T. A. Ramanarayanan and S. L. Bernasek, *Appl. Surf. Sci.*, 2007, **253**, 4322-4329.
205. P. Graat and M. A. J. Somers, *Surf. Interface anal.*, 1998, **26**, 773-782.
206. F. Lin, D. M. Jiang, Y. Lin and X. M. Ma, *Physica B-Condensed Matter*, 2008, **403**, 2193-2196.
207. P. Xiaoyan, J. Dongmei, L. Yan and M. Xueming, *J. Magn. Magn. Mater.*, 2006, **305**, 388-391.
208. M. Zhou, J. Yu and B. Cheng, *J. Hazard. Mater.*, 2006, **137**, 1838-1847.
209. M. A.G, *Electrochim. Acta*, 2007, **52**, 4167-4176.
210. P. Pu, H. Cachet and E. M. M. Sutter, *Electrochim. Acta*, 2010, **55**, 5938-5946.
211. M. Radecka, M. Rekas, A. Trenczek-Zajac and K. Zakrzewska, *J. Power Sources*, 2008, **181**, 46-55.
212. F. Spadavecchia, G. Cappelletti, S. Ardizzone, M. Ceotto and L. Falciola, *The Journal of Physical Chemistry C*, 2011, **115**, 6381-6391.
213. G. Rothenberger, D. Fitzmaurice and M. Gratzel, *Journal of Physical Chemistry*, 1992, **96**, 5983-5986.
214. J. Cabana, L. Monconduit, D. Larcher and M. R. Palacin, *Adv. Mater.*, 2010, **22**, E170-E192.
215. A. S. Arico, P. Bruce, B. Scrosati, J. M. Tarascon and W. Van Schalkwijk, *Nat. Mater.*, 2005, **4**, 366-377.
216. Y. Oumellal, A. Rougier, G. A. Nazri, J. M. Tarascon and L. Aymard, *Nat. Mater.*, 2008, **7**, 916-921.
217. C. Vidal-Abarca, P. Lavela and J. L. Tirado, *J. Power Sources*, 2011, **196**, 6978-6981.
218. E. Perre, P. L. Taberna, D. Mazouzi, P. Poizot, T. Gustafsson, K. Edstrom and P. Simon, *J. Mater. Res.*, 2010, **25**, 1485-1491.
219. P. Lavela, J. L. Tirado and C. Vidal-Abarca, *Electrochim. Acta*, 2007, **52**, 7986-7995.
220. C. Wang, D. L. Wang, Q. M. Wang and H. J. Chen, *J. Power Sources*, 2010, **195**, 7432-7437.
221. C. Wang, D. Wang, Q. Wang and L. Wang, *Electrochim. Acta*, 2010, **55**, 6420-6425.
222. J. M. Macak, B. G. Gong, M. Hueppe and P. Schmuki, *Adv. Mater.*, 2007, **19**, 3027-3031.
223. D. Grujicic and B. Pesic, *Electrochim. Acta*, 2004, **49**, 4719-4732.
224. D. Grujicic and B. Pesic, *Electrochim. Acta*, 2006, **51**, 2678-2690.
225. S. Bach, J. P. Pereira-Ramos and P. Willman, *Electrochim. Acta*, 2010, **55**, 4952-4959.
226. Y. S. Hu, L. Kienle, Y. G. Guo and J. Maier, *Adv. Mater.*, 2006, **18**, 1421-1426.
227. M. A. Reddy, M. S. Kishore, V. Pralong, V. Caignaert, U. V. Varadaraju and B. Raveau, *Electrochem. Commun.*, 2006, **8**, 1299-1303.
228. P. Poizot, S. Laruelle, S. Grugeon and J. M. Tarascon, *J. Electrochem. Soc.*, 2002, **149**, A1212-A1217.

229. H. C. Liu and S. K. Yen, *J. Power Sources*, 2007, **166**, 478-484.
230. Y. Wang and Q. Z. Qin, *J. Electrochem. Soc.*, 2002, **149**, A873-A878.
231. X. H. Huang, J. P. Tu, X. H. Xia, X. L. Wang, J. Y. Xiang, L. Zhang and Y. Zhou, *J. Power Sources*, 2009, **188**, 588-591.
232. Z. W. Fu, Y. Wang, Y. Zhang and Q. Z. Qin, *Solid State Ionics*, 2004, **170**, 105-109.
233. C. L. Liao, Y. H. Lee, S. T. Chang and K. Z. Fung, *J. Power Sources*, 2006, **158**, 1379-1385.
234. D. E. Fenton, J. M. Parker and P. V. Wright, *Polymer*, 1973, **14**, 589
235. M. Armand, *Adv. Mater.*, 1990, **2**, 278-286.
236. B. Scrosati, *Mater. Sci. Eng., B*, 1992, **12**, 369-373.
237. M. Armand, *Solid State Ionics*, 1994, **69**, 309-319.
238. K. M. Abraham and M. Alamgir, *J. Power Sources*, 1993, **43**, 195-208.
239. M. Alamgir and K. M. Abraham, *J. Power Sources*, 1995, **54**, 40-45.
240. F. B. Dias, L. Plomp and J. B. J. Veldhuis, *J. Power Sources*, 2000, **88**, 169-191.
241. M. Patel, M. Gnanavel and A. J. Bhattacharyya, *J. Mater. Chem.*, 2011, **21**, 17419-17424.
242. M. Kotobuki, Y. Suzuki, K. Kanamura, Y. Sato, K. Yamamoto and T. Yoshida, *J. Power Sources*, 2011, **196**, 9815-9819.
243. M. Kotobuki, H. Munakata, K. Kanamura, Y. Sato and T. Yoshida, *J. Electrochem. Soc.*, 2010, **157**, A1076-A1079.
244. M. Kotobuki, K. Kanamura, Y. Sato, K. Yamamoto and T. Yoshida, *J. Power Sources*, 2012, **199**, 346-349.
245. M. Kotobuki, K. Kanamura, Y. Sato and T. Yoshida, *J. Power Sources*, 2011, **196**, 7750-7754.
246. S.-J. Lee, H.-K. Baik and S.-M. Lee, *Electrochem. Commun.*, 2003, **5**, 32-35.
247. S.-J. Lee, J.-H. Bae, H.-W. Lee, H.-K. Baik and S.-M. Lee, *J. Power Sources*, 2003, **123**, 61-64.
248. Z. Ogumi, Y. Uchimoto and Z. Takehara, *J. Power Sources*, 1989, **26**, 457-460.
249. Z. Ogumi, Y. Uchimoto, Z. Takehara and Y. Kanamori, *Journal of the Chemical Society-Chemical Communications*, 1989, 1673-1674.
250. K. West, B. Zachau-Christiansen, T. Jacobsen and S. Skaarup, *J. Power Sources*, 1993, **43**, 127-134.
251. C. P. Rhodes, J. W. Long and D. R. Rolison, *Electrochemical and Solid State Letters*, 2005, **8**, A579-A584.
252. S. Tan, S. Walus, J. Hilborn, T. Gustafsson and D. Brandell, *Electrochem. Commun.*, 2010, **12**, 1498-1500.
253. S. Tan, S. Walus, T. Gustafsson and D. Brandell, *Solid State Ionics*, 2011, **198**, 26-31.
254. S. R. Gowda, A. L. M. Reddy, M. M. Shaijumon, X. B. Zhan, L. J. Ci and P. M. Ajayan, *Nano Lett.*, 2011, **11**, 101-106.
255. K. Dokko, J.-i. Sugaya, H. Nakano, T. Yasukawa, T. Matsue and K. Kanamura, *Electrochem. Commun.*, 2007, **9**, 857-862.
256. H. Nakano, K. Dokko, J. I. Sugaya, T. Yasukawa, T. Matsue and K. Kanamura, *Electrochem. Commun.*, 2007, **9**, 2013–2017.
257. M. Karakisla, M. Sacak and U. Akbulut, *J. Appl. Polym. Sci.*, 1996, **59**, 1347-1354.
258. S. L. Cram, G. M. Spinks, G. G. Wallace and H. R. Brown, *J. Adhesion Sci. Technol.*, 2003, **17**, 1403-1423.
259. X. Zhang, J. P. Bell and M. Narkis, *Journal of Applied Polymer Science*, 1996, **62**, 1303-1312.
260. Z. Adamcova and L. Dempirova, *Prog. Org. Coat.*, 1989, **16**, 295-320.
261. J. R. Maccallum and D. H. Mackerron, *Eur. Polym. J.*, 1982, **18**, 717-724.

262. S. L. Cram, G. M. Spinks, G. G. Wallace and H. R. Brown, *Electrochim. Acta*, 2002, **47**, 1935-1948.
263. T. Djenizian, B. Gelloz, F. Dumur, C. Chassigneux, L. Jin and N. Koshida, *J. Electrochem. Soc.*, 2010, **157**, H534-H539.
264. J. M. Macak, H. Tsuchiya, A. Ghicov, K. Yasuda, R. Hahn, S. Bauer and P. Schmuki, *Curr. Opin. Solid St. M.*, 2007, **11**, 3-18.
265. S. S. Sekhon, G. Singh, S. A. Agnihotry and S. Chandra, *Solid State Ionics*, 1995, **80** 37-44.
266. S. J. Wen, T. J. Richardson, D. I. Ghantous, K. A. Striebel, P. N. Ross and E. J. Cairns, *J. Electroanal. Chem.*, 1996, **408** 113-118.
267. X. Han, Y. Zhu, X. Yang and C. Li, *J. Alloys Compd.*, 2010, **500** 247-251.
268. M. Ye, D. Zhang, L. Han, J. Tejada and C. Ortiz, *Soft Matter*, 2006, **2**, 243-256.
269. L. Wang, L. Q. Xu, K. G. Neoh and E. T. Kang, *J. Mat. Chem.*, 2011, **21**, 6502-6505.
270. N. Luo, J. B. Hutchison, K. S. Anseth and C. N. Bowman, *Macromolecules*, 2002, **35**, 2487-2493.
271. B. C. Anderson and S. K. Mallapragada, *Biomaterials*, 2002, **23**, 4345-4352.
272. S. A. Pooley, B. L. Rivas and A. E. Maureira, *J. Appl. Polym. Sci.*, 2002, **85**, 2929-2934.
273. R. Murgasova and D. M. Hercules, *Anal. Chem.*, 2003, **75**, 3744-3750.
274. T. Gruendling, S. Weidner, J. Falkenhagen and C. Barner-Kowollik, *Polym. Chem-UK*, 2010, **1**, 599-617.
275. S. Leroy, H. Martinez, R. Dedryvere, D. Lemordant and D. Gonbeau, *Appl. Surf. Sci.*, 2007, **253**, 4895-4905.